Image-Based Quantification Workflow for Coronary Morphology: A Tool for Use in Next-Generation Bifurcation Stent Design

Sara Marie Nomeland
Marquette University

Recommended Citation
Nomeland, Sara Marie, "Image-Based Quantification Workflow for Coronary Morphology: A Tool for Use in Next-Generation Bifurcation Stent Design" (2010). *Master's Theses (2009 -)*. Paper 62.
http://epublications.marquette.edu/theses_open/62

IMAGE-BASED QUANTIFICATION WORKFLOW FOR CORONARY MORPHOLOGY: A TOOL FOR USE IN NEXT-GENERATION BIFURCATION STENT DESIGN

by

Sara M. Nomeland, B.S.

A Thesis Submitted to the Faculty of the Graduate School,
Marquette University,
in Partial Fulfillment of the
Requirements for the Degree of Master of Science in Biomedical Engineering

Marquette University

August 2010

ABSTRACT

IMAGE-BASED QUANTIFICATION WORKFLOW FOR CORONARY MORPHOLOGY: A TOOL FOR USE IN NEXT-GENERATION BIFURCATION STENT DESIGN

Sara M. Nomeland, B.S.

Marquette University, 2010

Coronary artery disease (CAD) occurs in ~200,000 bifurcation lesions annually. Treatment of CAD near bends and bifurcations is challenging and a preferred strategy for bifurcation lesions has yet to be established. However, a favorable treatment option may be elucidated by a more thorough understanding of vessel morphology as well as local hemodynamic alterations caused by current stenting approaches. Computational modeling of human arteries offers an attractive way to investigate the relationships between geometry, hemodynamics and vascular disease. Recent developments also make it possible to perform analysis on realistic geometries acquired noninvasively.

The objective of this work was twofold. The first aim was to build on previous work in this area by quantifying hemodynamic alterations introduced by treatment of an idealized coronary bifurcation using several approaches that involve multiple stents. Each model was created using combined computer aided design techniques and computational fluid dynamics (CFD) analysis tools. Resting and hyperemic blood flow conditions were also studied to determine the severity of local hemodynamic alterations and for comparison to previous results. Indices of time-averaged wall shear stress (TAWSS) and oscillatory shear index (OSI) were quantified for four idealized computational models. The luminal surface exposed to low TAWSS was similar in the main vessel (MV) for all models. Greatest differences were noted between un-stented versus stented side branch vessels (ex. rest: 1% vs. 35%). Sites of elevated OSI (>0.1) were minimal, except under hyperemia conditions in the MV (10% surface area). Flow disturbances were quantified for each provisional technique used, illustrating how stents protruding in main vessels impact flow profiles. Stents without kissing balloon dilation had abnormal flow disturbances, but showed decreased percentage of area exposed to areas of low WSS.

A second aim of this work was to design a robust and unbiased method to quantify vessel morphology and representative trends for three bifurcation sites prone to CAD. Computational models of these sites were generated using computed topography images from 22 patients. Models were used to query geometric characteristics from each bifurcation site including area, length, eccentricity, taper, curvature and bifurcation angles. Post-processing was accomplished by a combination of statistical methods and clustering analysis. Vessel length and area were significantly different within and between bifurcation sites. The left main coronary artery (LCA) bifurcation was significantly different from its two daughter bifurcations (left anterior descending and left circumflex arteries). Specifically vessel area and length were significantly different both between and within bifurcation sites. The daughter bifurcation sites were similar for all characteristics. Vessel area and length proved to be the most useful properties for identifying trends within a particular bifurcation site. The outcome of this work provides a workflow for characterizing coronary bifurcations and a strong foundation for elucidating common parameters from normal, healthy coronary arteries.

Collectively these results from idealized and patient-specific coronary bifurcations offer additional insight into the impact of current treatment approaches and characteristics associated with current stenting techniques. Flow disturbances and local hemodynamic changes have been quantified for provisional techniques currently used. These methods and results may ultimately be useful in the design of next-generation bifurcation stents.

ACKNOWLEDGMENTS

Sara M. Nomeland, B.S.

"There is nothing more difficult to take in hand, more perilous to conduct or more uncertain in its success than to take the lead in the introduction of a new order of things."
–Niccolo Machiavelli

This work would not have been accomplished without the expertise of those around me most notably my principal advisor John F. LaDisa Jr. PhD from Marquette University. Dr. LaDisa introduced me into the world of computational fluid dynamics and piqued my engineering interests by incorporating cardiovascular bio-fluids research with biomechanical engineering. I am forever indebted to him for taking a chance with me, by providing me an amazing research opportunity to work with him and his lab. This educational journey would not have been completed without the guidance of my Marquette University committee members; Dr. Kristina Ropella, PhD, Dr. Lars Olson, PhD, and Dr. Laura Ellwein, PhD. Their knowledge and assistance were vital to the final outcome of this work. I am forever grateful for their expertise and support.

A special thanks to the medical doctors who supported this research. In particular, Raymond Migrino, MD from the Medical College of Wisconsin/Veterans Affairs Health Care System, Phoenix, Arizona and Bon-Kwon Koo, MD, PhD from Seoul National University, in Seoul, Korea. As well as David S. Marks, MD MBA, Director, Cardiac Catheterization Laboratory & Clinical Trials and Associate Professor of Medicine, and Susan Mauermann, RN, CCRC, Manager Clinical Research in Cardiovascular Medicine at the Froedert & Medical College Cardiovascular Center for their support and collaboration in the bifurcation morphology portion of the investigation. Their medical expertise and guidance were instrumental in the fruition of this thesis.

I want to thank the members of the CV T.E.C. research group, in addition to engaging in discussions relevant to our work; many of them have been my friends as well as colleagues. In particular, I want to thank my lab mates; Dave Wendell, Arjun Menon, Hongfeng (Nick) Wang, Ronak Dholakia, Timothy Gundert and Sung Kwon. Most notably I need to acknowledge that my work conducted on coronary vessel quantification would have been impossible without assistance from Tim and the achievements he made in his own research. Also, Dave's assistance with image processing and interpretation techniques was critical in my learning of the cardiovascular system.

This work would not have been possible without financial support. I need to thank my funding source: Translational Opportunity Grant of the Pilot and Collaborative Clinical and Translational Research Grants program from the Clinical and Translational Science Institute of Southeastern Wisconsin.

I would like to thank my parents and sister, Beth whose support has been essential to my success, especially with regards to their financial and emotional assistance over the years. They have provided me with the freedom to pursue what I want and for that I am truly grateful. Finally, I would like to thank Ryan Sherman, for his constant support, for his understanding and for just being there. Thank you for being my best friend and believing in me even when I doubted myself.

TABLE OF CONTENTS

LIST OF TABLES

LIST OF FIGURES

ABBREVIATIONS AND ACRONYMS

3D = three dimensional
CAD = coronary artery disease
CFD = computational fluid dynamics
CVD = cardiovascular disease
D1 = first diagonal coronary artery
DES = drug-eluding stent
DIA = distal intersection angle
EI = eccentricity index
FFR = fractional flow reserve
JPDF = joint probability density function
IVUS = intravascular ultrasound
KB = kissing balloon
LAD = left anterior descending coronary artery
LCX = left circumflex artery
LMCA = left main coronary artery
MACE = major adverse cardiac event
MDCT = multidetector computed topography
MV = main vessel
NH = neointimal hyperplasia
OSI = oscillatory shear index
PCI = percutaneous coronary intervention
PIA = proximal intersection angle
PSB = provisional side branch stenting technique
PV = parent vessel
ROI = region of interest
SB = side branch vessel
TAWSS = time average wall shear stress
VMTK = vascular modeling toolkit
WSS (τ) = wall shear stress

CHAPTER 1 : INTRODUCTION

1.1 Cardiovascular Disease

According to the American Heart Association (AHA 2007) more than 80 million people in the United States are living with some form of cardiovascular disease (CVD). CVD is classified into a group of diseases which involve the heart and blood vessels of the human body. The heart functions as a pump to provide oxygen rich blood to meet the metabolic demands of the tissues perfused by the vasculature. Often CVD is manifested by a narrowing of blood vessels due to the excessive production of atherosclerotic plaque (Guyton and Hall 2006).

Atherosclerosis, the primary manifestation of CVD, is a disease of the arteries in which fatty lesions or plaques develop on the inside surfaces of the arterial walls and is associated with damage of vessel endothelium (Guyton and Hall 2006). Plaque formation can cause partial, or in extreme cases, total occlusion of a blood vessel which can lead to myocardial ischemia or infarction. Risk factors for atherosclerosis such as physical inactivity, elevated cholesterol levels, high blood pressure, diabetes mellitus, and smoking are typically manifested globally thereby having the potential to impact the entire vasculature. Approximately 50% of patients with CVD experience localized plaque in the arteries that perfuse that heart thereby leading to coronary artery disease (CAD)(AHA 2007). According the National Institute of Health (NIH), CAD is the leading cause of death in the United States for both men and women (NIH 2009).

1.2 Coronary Anatomy and Physiology

The coronary arteries are the primary source of myocardial perfusion and arise from the ascending aorta just above the semilunar valves. They consist of two separate branching networks; the right coronary artery which arises from the anterior sinus of valsalva and passes between the pulmonary artery and right auricular appendix, and the left coronary artery which arises from the left posterior sinus of valsalva and passes between the pulmonary artery and left auricular appendix before bifurcating further (Gray 2003). The main coronary arteries lie on the surface of the heart (epicardia) whereas the smaller arteries (endocardial) penetrate into the cardiac muscle (myocardium) (Figure 1.1). The resting coronary blood flow in humans is approximately 225 ml/min (about 4-5 % of total cardiac output).

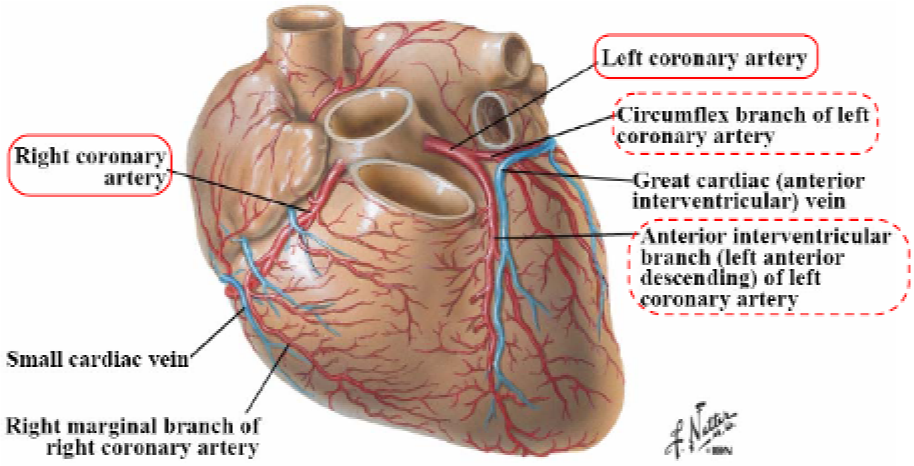

Figure 1.1: Anterior view of the heart and its major vessels. The solid lines indicate the primary coronary arteries from the aortic sinuses; the dashed lines indicate the bifurcating daughter vessels from the primary arteries. From the Atlas of Human Anatomy by Frank Netter.

The events of the cardiac cycle produce consistent, reproducible changes in blood pressure, velocity, flow, vessel caliber and curvature which correspond to specific valvular events. High tissue pressure in the myocardium during contraction restricts left ventricular perfusion during systole. Therefore, blood flow in the coronary arteries is maximized during diastole while myocardial pressure is at its lowest. This pressure-flow relationship is unique to the coronary arteries and has a direct impact on arterial blood flow waveform contours and vascular input impedance, important parameters used with computational fluid dynamics modeling. Recall that the coronary arteries provide the heart with its blood supply and Figure 1.2 illustrates which specific arteries perfuse different areas of the heart. A clear understanding of the perfusion territories of the heart helps to appreciate how an occlusion or narrowing can affect the heart. For instance, the left anterior descending artery provides blood supply to most of left ventricle which may be impacted if perfusion to this region is inadequate and its metabolic demands are not met.

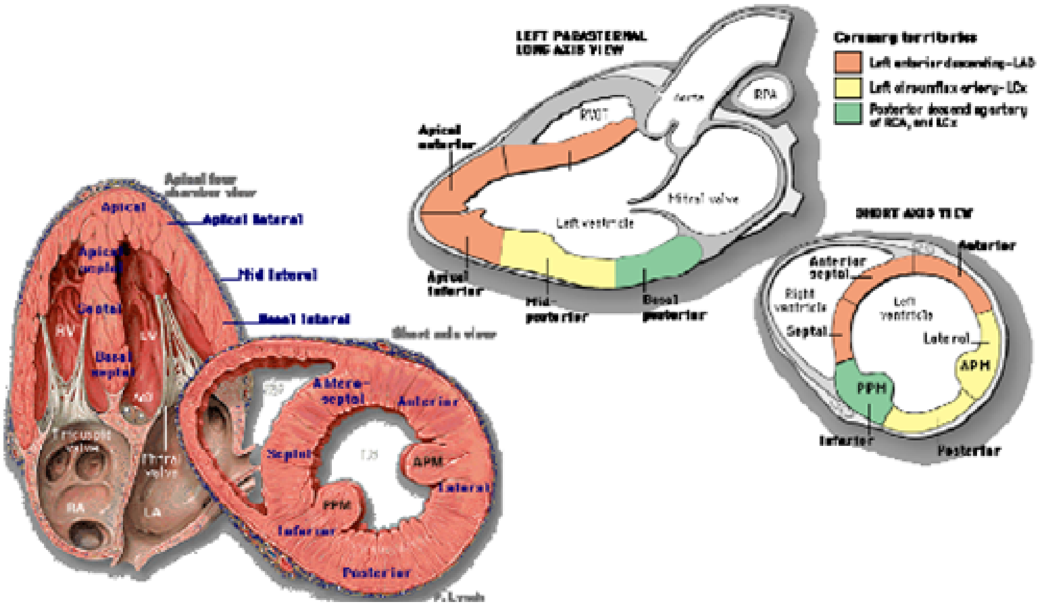

Figure 1.2: Coronary perfusion territories in different portions of the heart. Adapted from yale.med.edu.

The current investigation focused on the left coronary artery, also known as the left main coronary artery (LMCA), which arises from the aorta above the left cusp of the aortic valve. The LMCA primarily supplies the anterior and left lateral portions of the left ventricle, the essential pump of the heart. Coronary bifurcations are vessels which separate into two branches. The anatomy of the bifurcation is generally described by a parent vessel (PV) which then splits into two daughter vessels; usually referred to as main vessel (MV) and side branch (SB). The transition zone between the PV and the daughter vessels is called the ostium and the most distal portion of the ostium where the flow divider is located is known as the carina. Coronary bifurcations are prone to developing atherosclerotic plaque due, at least in part, by adverse local hemodynamic indices discussed in more detail below. These lesions amount to 15-20% of the total number of treated CAD patients (Sharma, Mareş, and Kini 2009).

1.3 Vascular Bifurcations: an area of altered fluid flow

Atherosclerotic plaque tends to localize in bends throughout the vasculature where blood flow is disturbed and particularly at bifurcations (Fung and Liu 1993). A high incidence of plaque accumulation occurs in the left coronary arterial system, specifically, the left anterior descending coronary artery (LAD) and first diagonal branch (D1) coronary bifurcation (Lefèvre et al. 2000; Wang et al. 2006). Healthy un-stented patients have blood flow velocity profiles which become skewed toward the flow divider, away from the lumen walls opposite the bifurcation (Figure 1.3). Curvature of the LAD does not allow for parallel fluid motion at all points within the artery. In this particular coronary bifurcation the axial velocity component of a fully developed parabolic flow is subjected to centrifugal forces and inertial effects causing the velocity profile to be skewed toward the outer epicardial wall. The location and geometry of the flow divider in addition to the downstream vascular resistance dictates how much fluid is directed into each branch and whether there is a potential for fluid recirculation to develop.

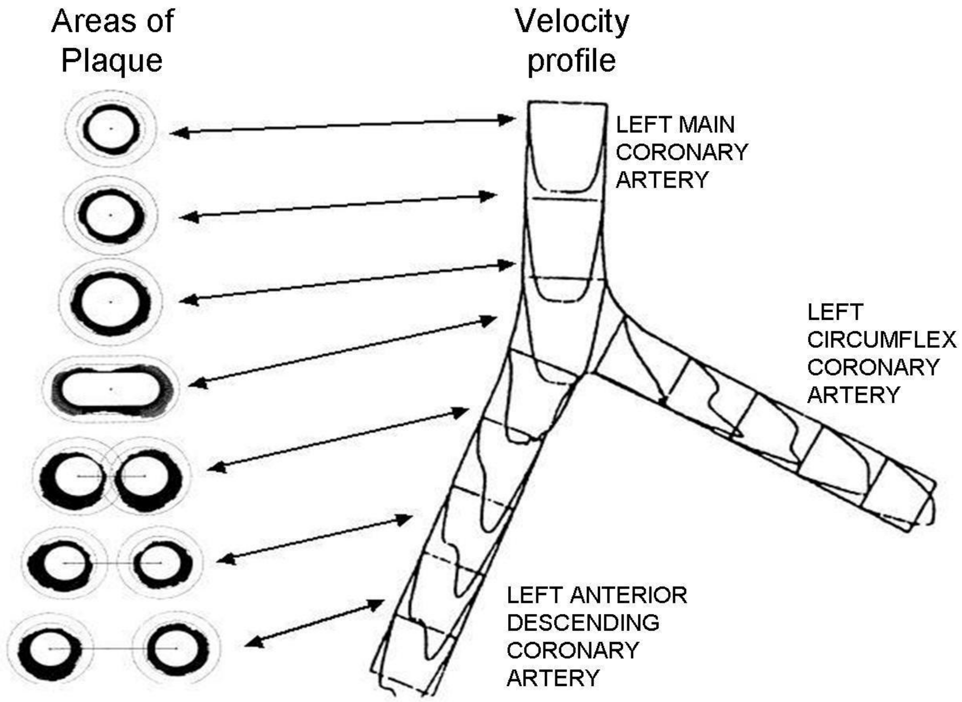

Figure 1.3: Velocity profiles of the left main coronary artery proximal and distal to the LAD/LCX bifurcation and corresponding cross-sectional distributions of plaque formation. Image adapted from Eric Gross, MD, PhD.

1.4 Stents for minimally-invasive treatment of coronary artery disease

Treatment options for CAD include pharmacological therapies and can include surgical interventions, such as: percutaneous coronary interventions (PCI), bypass surgery or heart surgery. Stent implantation has become a common interventional technique to improve blood flow through stenotic vessels (Mortier et al. 2009). Stents are defined as structured scaffold meshes, usually metal, that provide an expanded luminal surface to improve blood flow. Stents have become the preferred method of treatment as opposed to bypass surgery because of their high success rate, minimally invasive nature and improved long-term efficacy (Lefèvre et al. 2000). Bifurcations are considered challenging to treat with current interventional techniques. Of the more than 1 million

PCI treatments performed, approximately 200,000 involve bifurcation lesions (AHA 2007).

The most common method to treat atherosclerosis in coronary bifurcations is provisional side-branch (PSB) stenting. The PSB stenting technique consists of the insertion of a stent into the MV of the bifurcation and a dilatation of the SB by passing a second angioplasty catheter through the struts of the stent at the bifurcation. This approach can be followed by a redilation of the MV only or by kissing balloon (KB) inflation (i.e. simultaneous inflation of an angioplasty balloon in both branches). Both vessel redilation and KB, lead to a minor stent distortion in the MV (Gastaldi et al. 2010). Although numerous treatment techniques have been developed for various bifurcation lesions types (Figure 1.4), the complexity associated with stent delivery and potential for vessel damage, particularly in difficult geometries, have unfortunately let to less than favorable outcomes in many cases.

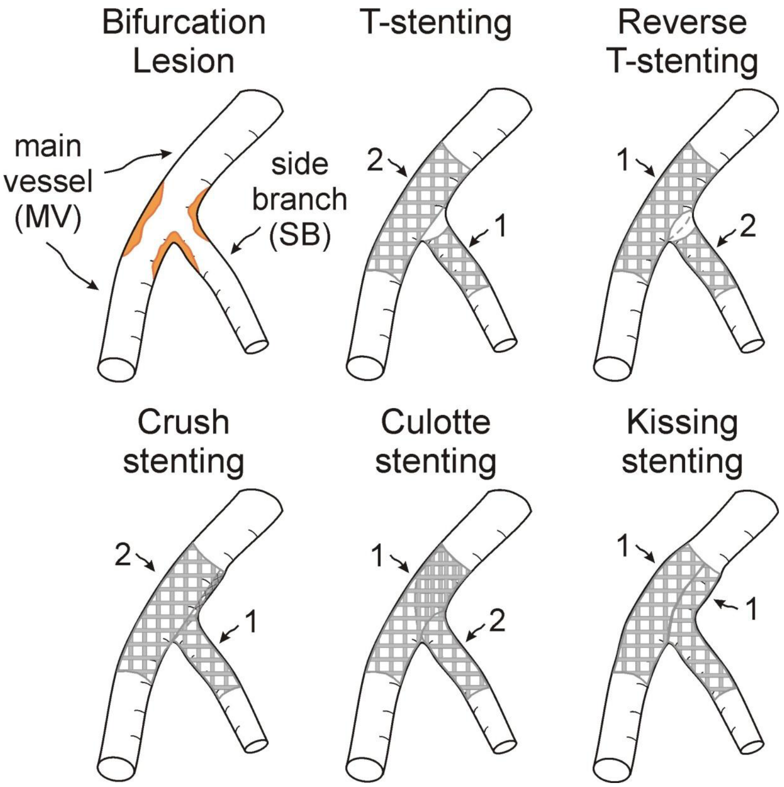

Figure 1.4: Stenting techniques for coronary bifurcations with multiple stents. Numbers indicate the implantation order. The most common plaque distribution is shown (top left).

Bifurcation stenting outcomes with both bare-metal and drug-coated stents have been investigated in several clinical trials. Colombo et al. compared the crush technique (two-stent) with the provisional T-stenting strategy (one-stent) (Colombo et al. 2004), where 73% of patients who had a two-stent treatment showed no significant difference between the one-stented and two-stented groups. Despite the lack of routine final KB inflation in the crush stent group there were no significant differences. Pan et al. compared the strategy of MV stenting and SB dilatation (without KB) versus a sequential T-stent strategy in 91 patients, which showed no statistical differences between the two groups after patient follow-up (6 months later) (Pan et al. 2007). Ge et al. compared the crush and the T-stent techniques in a nonrandomized assessment of 181 patients, 66 % of which had crush stenting. Ostial SB restenosis and MV restenosis at 1 year were both more common in the T-stent group. Clinically the effects of two-stent techniques have been examined by patient response, but there is still a lack of information as to the altered hemodynamics observed from performing each technique.

The current treatment of coronary bifurcation lesions involving systematic two-stent techniques described above results in longer procedure times, higher x-ray doses, increased procedural complications, and a higher rate of in-hospital and 9-month major adverse cardiac events (MACE) rate (Gastaldi et al. 2010). While it would be convenient to have an optimal two-stent approach, there is no optimal procedure which can accommodate every lesion type. Therefore, multiple two-stent strategies continue to exist in practice. Alternatively, a number of dedicated bifurcated stent designs have been developed in hopes of addressing some of the limitations with a two-stent approach.

Currently, eleven devices are available which have either completed or are currently undergoing human trials (Latib, Colombo, and Sangiorgi 2009). An example of a current bifurcated stent design is the Stentys™ Coronary Bifurcation Stent (Stentys, Paris, France) (Figure 1.5). The Stentys™ design is a self-expandable nitinol stent used for provisional stenting and is delivered as a single MV stent. After MV stent expansion the catheter is retracted and repositioned in the SB where the balloon will expand and dislodge (i.e. fracture) a break-away section of stent into the SB wall, providing increased SB patency. This design has recently been through its first round of human testing where it showed promising results and is now being considered by some as a potential alternative to provisional techniques (Laborde et al. 2007). Current clinical observations have shown this novel stent design to be a safe and potentially feasible alternative to PSB techniques because of its excellent procedural success rate and a low rate of MACE to date (Verheye et al. 2009).

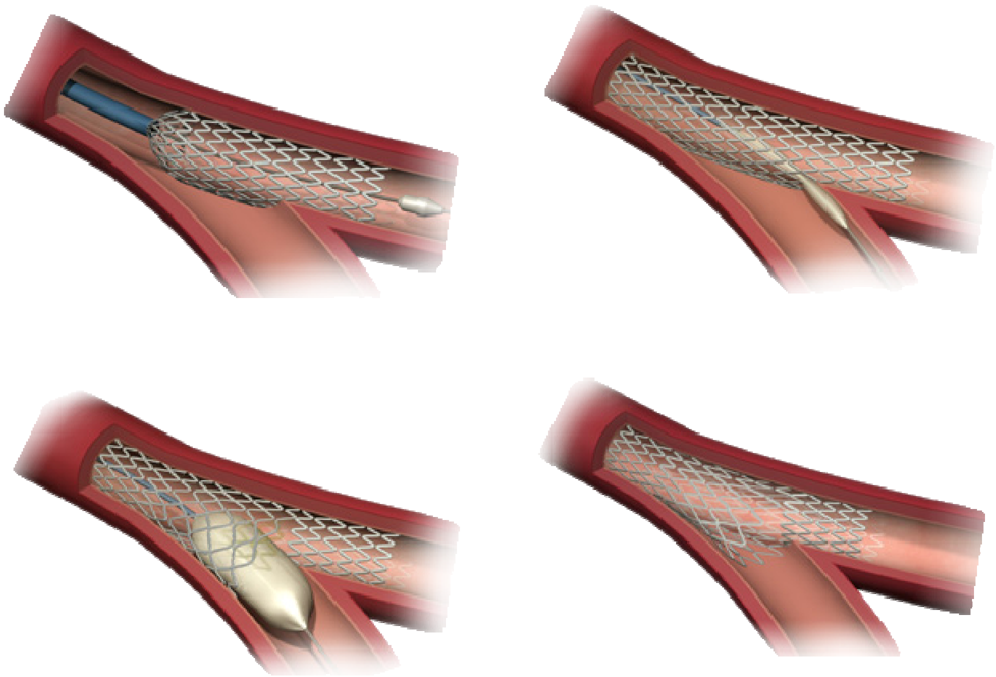

Figure 1.5: Schematic illustration of the implantation of the self-expandable Stentys device (Stentys™) in the MB (top left), followed by the insertion and inflation of an angioplasty balloon through the cell closest to the flow divider (top right and bottom left). This dilation disconnects the struts and results in improved SB access and ostium scaffolding. The bottom right panel shows the final stent shape. Courtesy Stentys™

1.5 Complications associated with stent implantation

Restenosis is characterized as a re-narrowing of the lumen by arterial tissue and is predominantly found in the stented region. Restenosis occurs in approximately 25% of patients who undergo an interventional stenting procedures (Dangas and Kuepper 2002). However, rates of restenosis fluctuate with stent geometry and can serve as a quantifiable metric for stent effectiveness (Kastrati et al. 2001). The incidence of restenosis in single vessels has diminished primarily from the introduction of drug-eluting stents (DES). The decrease in restenosis rates is accomplished by the gradual release pharmacological agents that prevent the re-growth of tissue in the arterial lumen.

While DES have been shown to limit restenosis, they are associated with a higher incidence of thrombus formation and stent migration (Finn et al. 2007). Some pharmacological agents on DES interrupt the natural healing process that occurs rapidly after stent implantation and is common with bare-metal stents. From a clinical perspective, the primary concern with DES is the potential for late thrombosis formation and subsequent embolization which is related to delayed endothelialization of the stent struts (McFadden et al. 2004). Clinical case studies have shown an increased occurrence of myocardial infarction following late (> 6 months) thrombus formations coinciding with the implantation of DES (Colombo et al. 2003).

While restenosis is the leading concern associated with interventional success, additional complications experienced with stenting procedures include: collapses, migrations, artery perforations, dissections, infection and stent mal-positioning generally associated with complex geometries (Wang et al. 2006). Collapses occur from a lack of balloon pressure during the expansion portion of the stenting procedure or loading within the in vivo environment. If the pressure applied to the balloon does not exceed the yield stress of the scaffold mesh structure, the stent may not maintain its expanded configuration. Migrations can occur from collapsed or mal-positioned stents and positioning difficulties usually present in bifurcations or tortuous vessels having complex geometries (Kitchens et al. 2002; Lefèvre et al. 2005). Among these complications, restenosis is still the primary obstacle in successful stent implantation. Currently, the dedicated bifurcation stents alluded to above are approved and under trial use; however, long-term data are not yet available or have not shown conclusive favorable evidence for many of these dedicated bifurcation platforms. Similarly, investigations into how bifurcated stent designs contribute to altered blood flow and stresses along and within the artery wall have yet to be determined.

1.6 Computational fluid dynamics as a tool for modeling blood flow through arteries

Computational fluid dynamics (CFD) is an advanced simulation tool used to quantify hemodynamic indices in vessels reconstructed from medical imaging data. CFD models can provide estimates of blood flow, pressure, velocity, wall shear stress (τ,WSS) and oscillatory shear index (OSI). WSS can be described as the tangential stress imparted onto the walls of a blood vessel as a result of flowing fluid.

Shear stress is best described by the basic example of a Newtonian fluid flowing between two plates where the motion caused by one infinite moving top plate over a stationary bottom plate imparts a stress from the moving fluid on the surface of the stationary plate. Therefore, WSS can be described by a relationship (Equation 1.1) of the fluid’s dynamic viscosity, μ, and the gradient of the near-wall velocity, *u*, with respect to the distance from the wall, *y*.

$$\tau = -\mu \frac{\delta u}{\delta y} \qquad \text{Equation 1.1}$$

Stent implantation has the potential to alter normal flow patterns which can cause deviations from the normal value of WSS that local endothelial cells prefer to experience. Low WSS is associated with an increased incidence of local CAD (Dangas and Kuepper 2002; Kastrati et al. 2001). WSS is difficult to quantify *in vivo* since imaging modalities such as MRI and pulsed and spectral Doppler are only able to resolve velocity to approximately 0.9 mm. This limited resolution in the radial direction can lead to large errors in WSS (Katritsis et al. 2007). Therefore, assuming that the geometry of the vasculature can be accurately modeled via imaging data, CFD can provide a superior estimate of WSS.

CFD uses a finite element mesh and numerical flow solver to calculate fluid velocity at submillimeter distances from the vessel wall. The inclusion of multidimensional fluid flow includes more complex calculations of WSS that reduce to Equation 1.1 in a simple shear flow. Briefly, total stress on the wall is calculated as the sum of pressure and viscous forces. For each point on the luminal surface a normal vector is defined. The product of the normal vector and total stress imparted on the wall yields a traction vector. By subtracting the normal component from the traction quantity, the surface vector is isolated. WSS is then determined as the magnitude of the calculated surface vector and viscosity.

Coronary stented regions are vulnerable to restenosis which is caused primarily by neointimal hyperplasia (NH) (Heldman et al. 2001). Additionally, areas of low WSS are associated with the growth and progression of NH (Kleinstreuer et al. 2001). NH is identified by an increased proliferation/differentiation process which increases the layers of cells on the inner lining of the arterial vessel (Subbotin 2007). Patterns of WSS are most often quantified using the indices of TAWSS and OSI. Generally, high TAWSS protects against neointimal hyperplasia, whereas low TAWSS (< 4 dynes/cm^2) and high OSI values are correlated with observance of neointimal hyperplasia in the coronary arteries (Malek, Alper, and Izumo 1999). OSI is a hemodynamic index which quantifies the deviation of WSS from the primary flow direction during the cardiac cycle. In practice, WSS is averaged over the cardiac cycle which allows for OSI to be calculated using the following Equation 1.2 (Les et al. 2010; Taylor, Hughes, and Zarins 1998):

$$OSI = \frac{1}{2}\left(1 - \frac{\tau_{mean}}{\tau_{mag}}\right) \qquad \text{Equation 1.2}$$

τ_{mean} is the addition of all WSS vectors at a given point, then averaging them over the cardiac cycle, and finally taking the magnitude of the resulting vector. τ_{mag} is the average sum of magnitudes of each WSS vector over the cardiac cycle. OSI quantifies the deviation of WSS from the primary flow direction during the cardiac cycle. OSI ranges between 0 and 0.5 because τ_{mean} will always be less than or equal to τ_{mag}. Lower OSI values indicate WSS is oriented predominately in the primary direction of blood flow while a value of 0.5 is indicative of bi-directional WSS with a time-average value of zero throughout the cardiac cycle.

Severity of stenosis can be assessed using a clinical index called fractional flow reserve (FFR). FFR is a physiologic parameter representing the fraction of maximal myocardial flow that can be maintained in the presence of an epicardial coronary stenosis (Pijls et al. 1996; Pijls et al. 1993). FFR can be quantified as the flow through a stenosis under maximum vasodilation (Q^{S}_{max}) divided by the flow through a corresponding normal vessel under maximum vasodilation (Q^{N}_{max}). Under most clinical circumstances, this measurement is not practical because the normal flow measurement, which must be made in the absence of the existing stenosis, is not available. However, if one assumes a linear relationship between pressure and flow, FFR can be approximated using pressure measurements. Therefore, clinically, FFR is approximated as the pressure distal (P_d) to a stenosis divided by the pressure proximal (P_p) to the stenosis during maximal vasodilatation. In practice FFR can be obtained by the ratio of distal coronary pressure and proximal aortic pressure (equation 1.3). For the current investigation, FFR is calculated using transient pressure and flow values queried from converged simulation results at the inlet and one cm distal to the bifurcation in the SB.

$$FFR = \frac{Q^{S}_{\max}}{Q^{N}_{\max}} = \frac{(Pv - Pd)/R}{(Pa - Pv)/R} = \frac{Pd}{Pp} \qquad \text{Equation 1.3}$$

The pressure values used in the FFR calculation were then determined from mean pressure calculated as

$$P_{mean} = \frac{(2 * P_{diastole} + P_{systole})}{3} \qquad \text{Equation 1.4}$$

1.7 Relationship of this study to previous work

To date, a moderate number of studies have examined hemodynamic alterations caused by bifurcation stenting (Deplano, Bertolotti, and Barragan 2004; Frank, Walsh, and Moore 2002). However, these studies have used overly simplistic representations of the vasculature and stents, while also computationally implanting these stents with non-realistic techniques and poor simulation boundary conditions. In contrast, the current work uses idealized CFD models based upon anatomical measurements and clinical observations of traditional one –stent and PSB techniques. The stent geometry included in these models represents that of a current device used frequently and outlet boundary conditions that achieve desired blood flow distributions and physiologic pressure within the bifurcation region similar to Vignon-Clementel et al. (Vignon-Clementel et al. 2006).

With advancements in imaging technologies including the recent establishment of 64-row multidetector computed topography (MDCT) scanners, three-dimensional (3D) vascular images are easily acquired with submillimeter resolution (Miller et al. 2008). To date, a small number of image-based studies have investigated geometric quantities associated with the coronary arterial tree. Previously, mostly cadaver castings and two-dimensional angiography were used to attain coronary morphology metrics (Girasis et al. 2010; Reig and Petit 2004; van der Waal et al. 2009). While previous studies claim to be 3D, the imaging modality predominantly employed uses 2D angiography techniques as compared to what is available via the MDCT scanner. Therefore 2D angiography studies may not as accurately reproduce geometric features such as curvature in multiple planes or vessel overlap (Pflederer et al. 2006). Secondly, while casting studies provide insight into branching patterns and anatomical data, it is more useful to have a non-invasive *in* *vivo* method available to quantify vessel morphology. Additionally, most casting studies measure geometric characteristics such as bifurcation angle from a 2D prospective such as under a microscope, which is operator dependent. Therefore, there is a need to implement a relatively rapid and robust workflow which can be used to ascertain coronary morphology using 3D image data, and can be applied for use with CFD.

Williams et al. investigated the effects of PSB techniques, but only with respect to MV stenting (Williams 2008). The current study expands on their methods to include more complex geometries, exploring PSB techniques modeled to induce stenting within the SB vessel and simultaneous KB dilation. The inclusion of SB stenting applied to CFD analysis will provide a better understanding of the local hemodynamic changes and expand on what was previously reported.

Improvement on previous methodologies used to quantify hemodynamic alterations and vessel morphology associated with bifurcations and stenting is a necessary progression. Future advancements will lead to an enhanced next-generation stent design that is geometrically optimized to lessen fluid disturbances and thus the potential for restenosis.

1.8 Objectives and specific aims

The objective of this thesis is to expand on previously developed idealized stented mythologies, by including more complex PSB techniques. The addition of this complexity allows for the inclusion of more physiologic stent implantation methods. Knowledge of coronary arterial morphology is also required to better understand the design parameters related to stents for these vessels. Therefore a method to obtain and quantify patient-specific data in a rapid and robust way is required.

The first specific aim of this thesis is a continuation of methods previously reported (Williams 2008). The second specific aim of the thesis are derived from a desire to more accurately model features of the coronary vasculature which are lacking in the results produced from the first specific aim. More accurate morphometric representations garnered from this portion of the thesis are required and will be applied future models and CFD analyses.

Specific Aim 1: Simulate blood flow through more complex, but still idealized, models of LAD/D1 bifurcation configurations including: MV stenting followed by aggressive KB inflation, a two-stented model showing MV and SB stenting without kissing, MV and SB stenting followed by gentle KB inflation, and MV and SB two-stented model followed by aggressive KB inflation. These four configurations will be created from vascular imaging data and clinician guidance.

Specific Aim 2: Design a robust and automated patient-specific image-based workflow that rapidly quantifies geometric indices associated with vessel morphology for three coronary bifurcation sites prone to CAD. Post-process geometric quantities from medical imaging data of three coronary bifurcation sites prone to CAD of interest for a group of patients by applying statistical methods to quantify trends and determine what differences exist among the three bifurcation sites.

Ultimately, the results of this thesis will provide a foundation for many of the tools that can be used in subsequent studies to create a bifurcated stent design that minimizes blood flow disturbances and vessel damage in an attempt to reduce the occurrence of restenosis. The results will also allow for large amounts of patient data to be quickly analyzed while providing additional knowledge of trends and clusters within different coronary bifurcation sites and vessel segments.

CHAPTER 2 : SPECIFIC AIM 1

2.1 Background

Idealized model construction paired with CFD analysis provides insight into what is occurring physiologically within the specified system at a localized level. Stenosis severity is often evaluated angiography by a clinician's visual inspection of the vessel although current imaging techniques offer no information about hemodynamic severity of the stenosis. In contrast, FFR can be used to elucidate the severity of stenosis using local hemodynamic measurements. Previous investigations aimed to quantify FFR for two idealized vessel models with varying stenotic SB vessels inlets (Figure 2.1) in order to verify that CFD could reproduce FFR findings reported clinically. These idealized vessels compared FRR results resulting from a reduction in SB diameter (50 and 75%, respectively) along the lateral wall opposite the carina, a common location for atherosclerotic plaque.

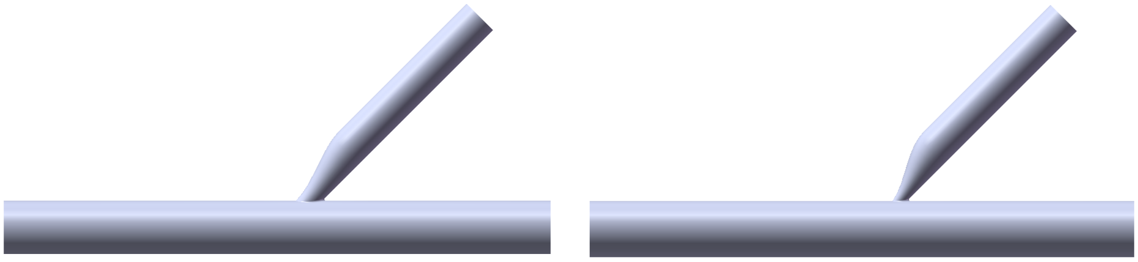

Figure 2.1: Idealized vessels comparing multiple side branch reductions in diameter, 50% (left) and 75% (right) to establish hemodynamic severity of stenosis using the FFR calculations

After performing CFD analysis on two idealized models (Figure 2.1) mean pressure values were quantified under hyperemia conditions. Locations were selected in the MV proximal to the stenotic SB as well as distal locations within the stenotic SB (Figure 2.2). A clinically significant FFR criterion has previously been as established as a value <0.75 (Koo et al. 2008) which is considered to occur for critical SB stenoses. The FFR calculations were not clinically significant for the 50% reduction in diameter (FFR = 0.83), but were clinically significant in the 75% reduction case (FFR = 0.73). These findings affirm that CFD can be used to investigate coronary artery disease severity or treatment options in a rapid and physiological manner prior to applying an intervention clinically.

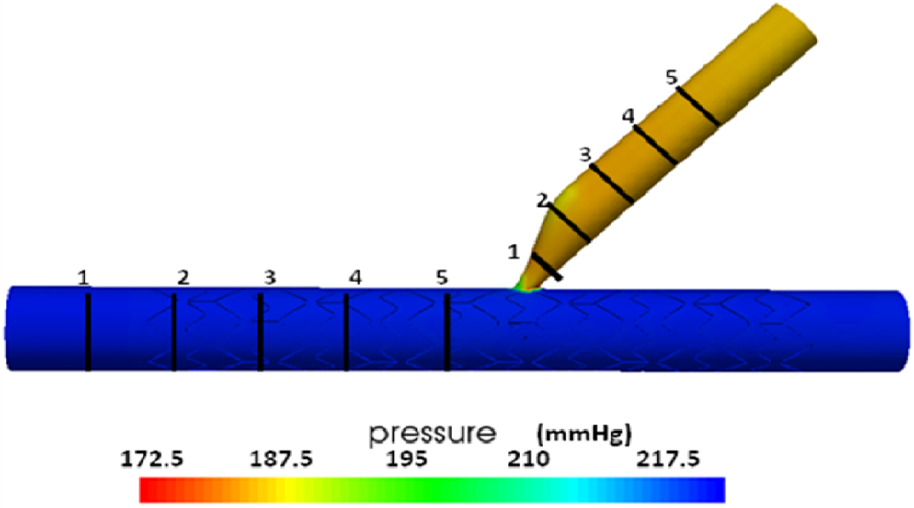

Figure 2.2: Pressure quantification locations for idealized vessels under maximum vasodilation flow conditions.

Williams et al. (Williams et al. 2010) performed CFD analysis to quantify FFR in MV stented models which underwent post SB angioplasty (Figure 2.3). The location of the carina, SB ostial area and distal MV dimensions after MV stent implantation and SB angioplasty were then altered based on the concept of carina shift (Vassilev and Gil 2008) and intravascular ultrasound (IVUS) images obtained from Bon-Kwon Koo MD, PhD, Assistant Professor of Cardiology, College of Medicine, Seoul National University.

FFR in the SB as a result of MV stenting-induced stenosis, or by partial occlusion of the ostium by stent struts ranged from 0.95-0.99. The severity of the stent struts present in the ostium (jailing of the SB) had a greater impact on FFR than the post SB angioplasty induced carina shifting. Clinically the shift carina introduced could be considered an angiographically significant stenosis and therefore might be treated with additional interventional procedures. However, Williams found that FFR measured by both pressure and flow parameters were all within normal range despite angiographic stenosis of 54%, suggesting that additional interventions would not provide a more favorable outcome from a hemodynamic perspective.

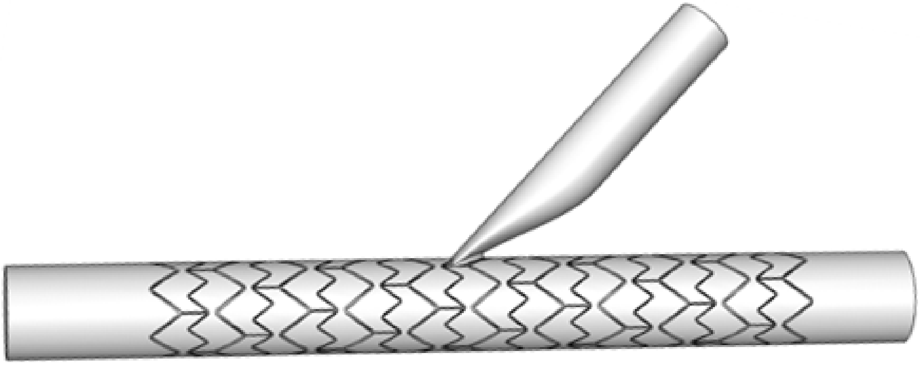

Figure 2.3: Idealized main vessel stented model demonstrating the concept of carina shift and associated partial side branch stenosis as created by Williams et al.

Specific aim 1 of the current work is a continuation of the methods outlined by Williams et al. using more complex stented vessel geometries and multiple stents. Four non-diseased idealized bifurcation models were created using a typical bifurcation angle. Therefore, the objective is to quantify altered hemodynamics as a result of MV and SB stenting resulting from these additional, more complex stenting techniques.

2.2 Methods

An overview of the process to conduct CFD analysis is visually represented in the schematic drawing of Figure 2.4. The analysis begins with an idealized geometry representing anatomically accurate coronary vessel parameters which is created in a computer aided design software program. Representative morphometric values (vessel diameter, length, and bifurcation angle) obtained from imaging data are used to create a sketch which is the template used to construct the 3D model. A clinically relevant stent design is chosen and modeled in an expanded configuration. The solid model undergoes a series of Boolean operations to remove the stent from the vessel surface, providing the fluid domain for CFD analysis. Detailed instructions are included in the thesis of Andrew Williams, M.S (Marquette University) and are discussed further in the methods below.

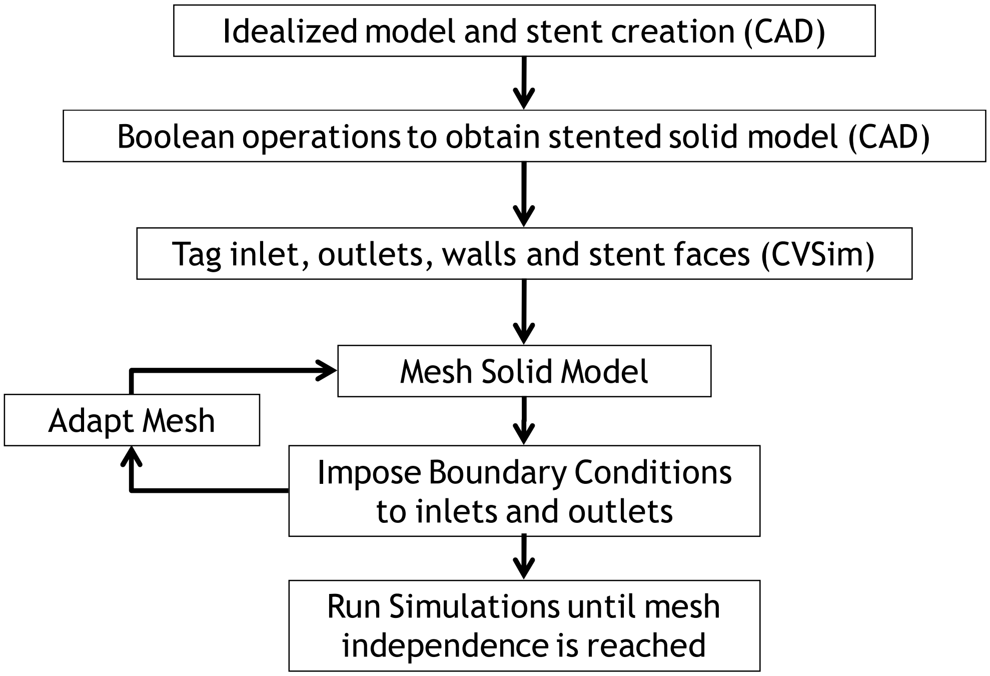

Figure 2.4: Schematic of the workflow outlining how to perform CFD analysis on idealized vessels

Within the CFD software, the model faces are tagged with names (inlet, outlet, wall, or stent) which are used to assign boundary conditions. Once tagging is completed, mathematical representations of physiological events, boundary conditions, are applied to the inlet and outlets of the model. An adaptive meshing process is used until mesh independence is achieved. These steps will be discussed in further detail below.

2.2.1 Creation of idealized left anterior descending coronary artery (LAD) – Diagonal (D1) branch bifurcation models

Four idealized solid models were constructed in the following configurations: A) MV stenting followed by aggressive KB inflation, B) a two-stented model showing MV and SB stenting without KB, C) MV and SB stenting followed by gentle KB inflation and D) MV and SB two-stented model followed by aggressive KB inflation (Figure 2.5).

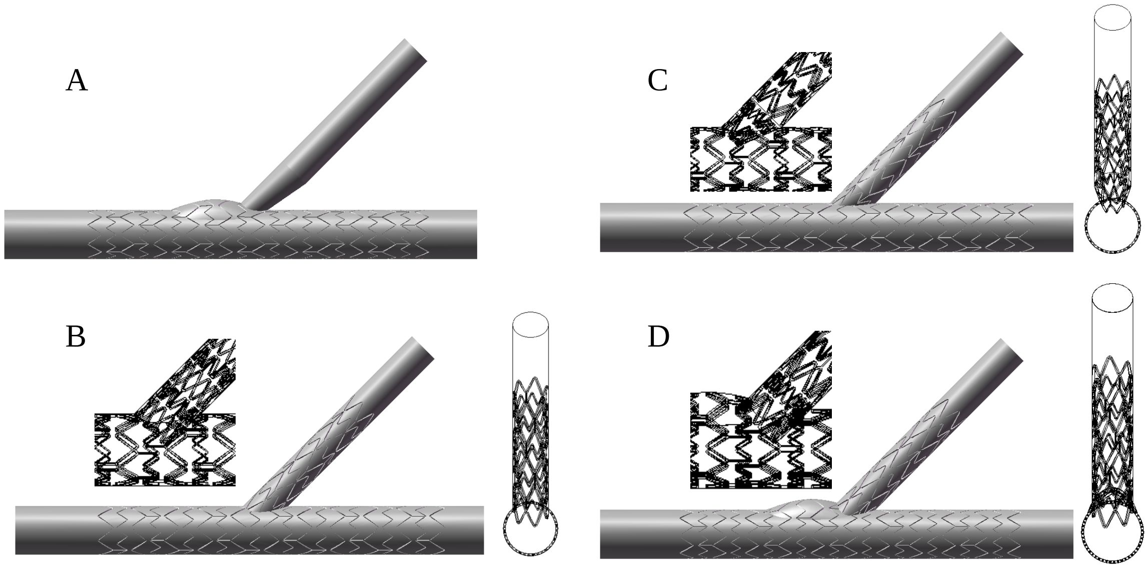

Figure 2.5: A, B, C and D: The same primary vessel geometry using different combinations of provisional stenting techniques. A) Illustrates MV stenting with aggressive kissing which is shown via the elliptical cross-section just proximal to the bifurcation, B) portrays MV and SB stenting without kissing, C) MV and SB stenting with gentle kissing, the SB stent is reduced to 40% its original diameter within the MV and D) MV and SB stenting with aggressive kissing causing an elliptical over-expansion of the proximal MV, SB stent protrudes directly into MV without tapering.

After obtaining vascular dimensions from imaging data, a part document was created using SolidWorks (SolidWorks Corp., Concord, MA) a computer aided design software. Cross-sections were sketched along the axis of each vessel. Protrusion and rounding functions were used within the software to join the cross-sections at the intersection of the vessels. Stented vessels incorporated the Express^2 stent design (Boston Scientific Corporation, Natick, MA). Stents were generated from a hollow tube with the appropriate strut thickness. A sketch with the stent linkage pattern and strut dimensions was wrapped onto the hollow tube. The stent pattern was then cut from the tube using the normal cutout command and the stent pattern was propagated radially and axially before excess material on the ends of the stent was removed.

In Solid Edge (Siemens, Plano, TX), a Boolean intersection command was then implemented to subtract the stent from the lumen thereby generating the potential region for blood flow within the bifurcation after MV stenting. The same procedure performed on the MV was used to construct and isolate the SB stented region. A secondary step was required to remove the stent struts from the bifurcation region. To obtain a non-obstructed SB, the SB vessel was subtracted from the MV stent body. This addition mimics the effects of SB angioplasty, therefore removing stent struts from the inlet SB flow domain (non-jailed SB inlet). The wirefame figures next to the solid models are meant to illustrate how the SB stents are positioned. The SB proximal diameter was reduced to 40% of its original diameter for models A and C as illustrated in Figure 2.5. This reduction in diameter was performed to simulate gentle KB dilation. Aggressive KB dilation is manifested by an elliptical cross-sectional area just proximal to the bifurcation region (Models A and D in Figure 2.5) Detailed illustrations of the various SB stent configurations are presented in Figure 2.6. Additional simulations were also conducted for all idealized models without the presence of stents in order to isolate the independent hemodynamic contributions of struts as compared to vessel geometry.

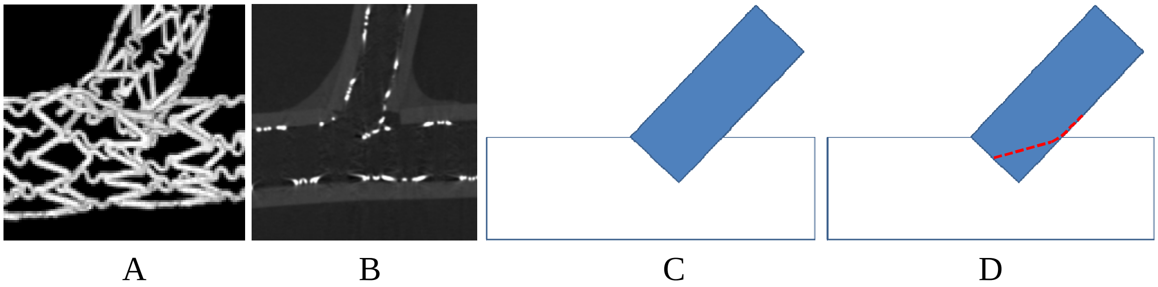

Figure 2.6: Visual representations to show the position of the SB within the MV for various idealized vessels. A & B) micro-CT images illustrating the protrusion of the SB stent in the MV. C) The shape of the SB stent (blue) for the model MV/SB stenting without kissing balloon dilation. D) The SB stent area (blue) is removed below the red dotted line in the gentle kissing model which reduces the inlet to the SB to 40% the original area.

2.2.2 Computational fluid dynamic analysis

A Inflow conditions

Arteries were assumed to be rigid and subjected to blood flow velocity waveforms obtained from a canine LAD coronary artery under normal resting and hyperemic conditions shown in Figure 2.7 and as previously described (LaDisa et al. 2002). Resting and hyperemic inflow waveforms (Reynolds number ~90 and 240, respectively) were imposed as temporally-varying Womersley velocity profiles ($\alpha = 2.9$ and 2.6, respectively) using the cvSim CFD software package (Cardiovascular Simulation, Inc., Mountain View, CA; www.cvsim.com).

With knowledge of radii in the LAD and D1 vessels ($r_{lad} = 1.354$ mm and $r_{d1} = 1.118$ mm, respectively), the percentage of blood flow to each daughter branch was calculated as 64% and 36% for the LAD and D1, respectively. This blood flow distribution was used during rest and hyperemia for all models and was based on the principles outlined by Murray’s Law (Murray 1926). Murray described an ideal branching pattern which minimizes energy loss (Equation 2.1), through a relationship between the diameter of the parent vessel and the two daughter vessel diameters.

$$\text{Murray's Law: } D_{parent}^{3} = D_{daughter1}^{3} + D_{daughter2}^{3} \qquad \text{Equation 2.1}$$

The distribution of blood flow between the distal LAD and D1 outlets was calculated by assuming WSS is the same in the distal MV and SB as was previously described by Williams et. al (Williams 2008).

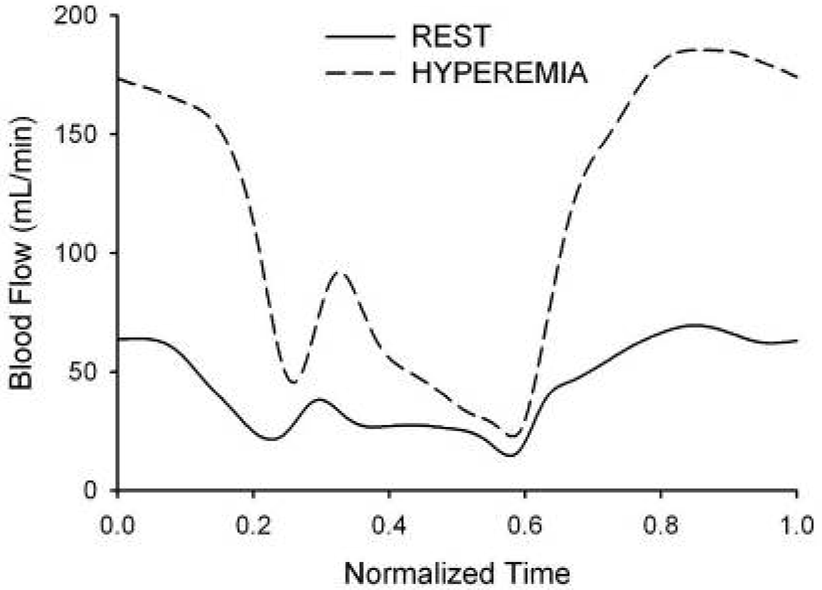

Figure 2.7 Blood flow waveforms applied to the inlet of each model for rest and exercise (hyperemia)

B Outlet boundary conditions

Outlet boundary conditions for the coronary arteries are more difficult to impose than in other vascular regions since pronounced resistance is introduced by myocardial contraction which results in a non-linear, time-varying system for which standard frequency analysis is invalid (Bovendeerd et al. 2006). However, previous work has demonstrated that linearity and time-invariance can be assumed and the behavior of the downstream vasculature in the absence of ventricular contraction can be estimated using a 3-element Windkessel (i.e. RCR) approximation (Van Huis, Sipkema, and Westerhof 1987) under certain circumstances. Van Huis et al. found the impedance modulus at zero hertz, but their impulse response methods produced a lower value than the total resistance value since their methods neglect the influence of ventricular contraction. On average, the zero hertz resistance was 37.7% (range 21.7 to 65.0%) of the total resistance. Parameters used for resting and exercise (hyperemia) conditions obtained using this approach are provided in Table 2.1.

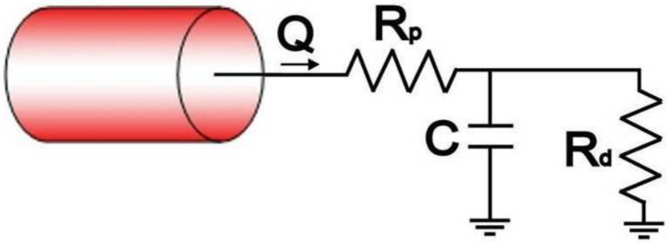

Figure 2.8: Three-element Windkessel model represented as an electrical analog which describes the outlet boundary conditions of the coronary vasculature via RCR parameters. Rp is the characteristic impedance, C represents the collective capacitance of the local and distal vessels and Rd represents the resistance downstream from the vessel.

Flow Condition	Outlet Branch	Rt (dyn·s/cm^5)	Rp (dyn·s/cm^5)	C (cm^5/dyn)	Rd (dyn·s/cm^5)
Rest	LAD	194,900	15,690	2.24E-06	179,300
	D1	346,200	23,000	1.26E-06	323,200
Hyperemia	LAD	73,660	18,410	1.60E-05	55,250
	D1	130,800	27,000	9.01E-06	103,800

Table 2.1: RCR parameters for both rest and exercise conditions applied to CFD simulation outlet boundary conditions. Rp, characteristic impedance, C, capacitance, Rd, distal resistance; Rt represents the total vascular resistance in the absence of ventricular contraction using the impulse response method Van Huis et al.

C Additional simulation parameters

Blood was assumed to behave as a Newtonian fluid with a density of 1.06 g/cm^3 and dynamic viscosity of 4 cP. Three cardiac cycles were run for each simulation to ensure the results were periodic. Periodicity was assumed when the maximum error between equivalent points in successive cardiac cycles for pressure and flow were <1 mmHg and 1 mm^3/s, respectively. Stented bifurcation models were discretized using a commercially available adaptive mesh generation program (MeshSim, Simmetrix, Clifton Park, NY). Final mesh edge sizes (see Results 3.1) were adequate to resolve microscopic flow in the neighborhood of struts and simulations were scrutinized to ensure results were independent of the number of mesh elements in each model.

D CFD analysis

CFD simulations were performed using a stabilized finite element method to solve the equations for conservation of mass (continuity) and balance of fluid momentum (Navier-Stokes) (Figueroa et al. 2006). After verifying that simulation results were mesh independent, replicated aimed blood pressure, and flow distributions were maintained, TAWSS and OSI were calculated consistent with the descriptions above and as previously described (Tang et al. 2006).

Previous studies have demonstrated that distributions of TAWSS <4 dynes/cm^2 and high temporal oscillations in WSS quantified by OSI are associated with cellular proliferation, intimal thickening and vascular inflammation (He and Ku 1996). An automated computer program was written to quantify the area of simulation results containing TAWSS <4 dynes/cm^2. To do this, the surface results file for each index of interest (.vtk extension) needed to be isolated into points, polygons and scalars. The points file contains the coordinates of each node of the surface mesh. The polygons file contains the connectivity of those nodes to each other. The scalars file contains the values for TAWSS assigned to each node. The algorithm then queried the polygon array to obtain the point numbers of each element. The associated scalar values for those points were then loaded and averaged. If the averaged was below the threshold of 4 dynes/ cm^2, then the area of the element was obtained by Heron's formula. The area of the lumen surfaces containing OSI >0.1 was also quantified using this procedure described for low TAWSS.

2.2.3 Assessing mesh independence

For this work, simulation results were assumed to be independent of the spatial computational mesh when TAWSS at a number of predetermined locations within the computational domain changed less than 6% (< 0.09 dynes/cm^2) between two successive meshes. Using boxes specifying circumferential locations in the proximal LAD, distal LAD and side branch, as well as several intra-strut faces in the proximal and distal locations of the stent (Figure 2.9), TAWSS was compare between the results of the two most recent meshes (LaDisa et al. 2004). Mesh adaption was performed using an error file created during the simulation. The adaption process assigns more elements in areas of high error and fewer elements in areas of low error to create anisotropic meshes. Operator imposed parameters such as error reduction factor, global minimum and maximum edge size were used to control the increase in number of elements (Müller et al. 2005).

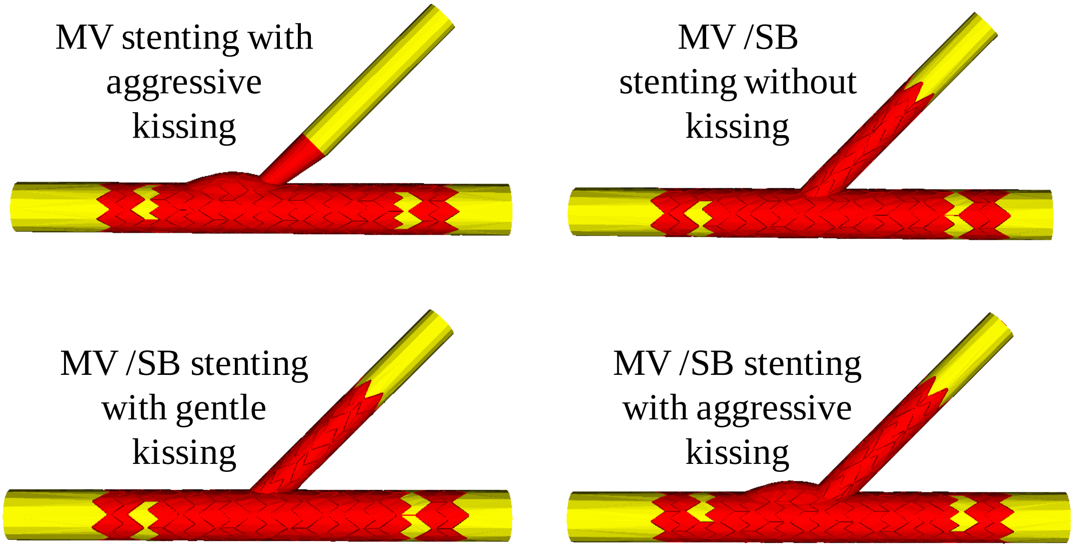

Figure 2.9: Vessel areas (yellow) where TAWSS values were quantified and compared between successive meshes to establish if mesh independence was achieved.

2.3 Results

Williams et al. found that between 2 and 7 meshes were required to satisfy the mesh independence criteria (Williams et al. 2010). The current study performed 7 meshes for each idealized model. The first mesh was isotropic and consecutive meshes were anisotropic; meaning the first mesh was comprised of the same tetrahedral element size, while consecutive meshes put varying sized elements in different locations based on error within the mesh from previous simulations. The number of successive meshes for each CFD model is shown in Table 2.2.

Model	M1	M2	M3	M4	M5	M6	M7
MV stenting with aggressive kissing	444614	476021	800587	1440345	1645686	2232833	2420000
MV /SB stenting without kissing	457409	483618	807766	1294362	1556880	2105273	2533344
MV /SB stenting with gentle kissing	453693	500538	951528	1299865	1542166	2043544	2639787
MV /SB stenting with aggressive kissing	446391	465893	811820	1249096	1649449	2078316	2554422

Table 2.2 Number of finite elements for successive meshes (M1 = mesh 1) for each performed CFD simulation the final mesh (M7) was used for hyperemia conditions

Mesh independence was assessed using TAWSS values for regions in the proximal MV, distal MV, SB and two intra-strut regions within the MV (Williams 2008). This procedure was conducted for resting conditions, the results are provided in Table 2.3. All simulations reached mesh independence as they were < 6% change between successive meshes. Hyperemia conditions were simulated at final resting meshes similar to previous work (Tang et al. 2006).

		Prox.	Dist.	Side	Prox. Cell	Dist. Cell
MV stenting with aggressive kissing						
Mesh 5	**TAWSS**	0.314	0.147	0.728	0.380	0.907
	ABS Change	▨	▨	▨	▨	▨
	% Change	▨	▨	▨	▨	▨
Mesh 6	**TAWSS**	0.326	0.160	0.731	0.383	0.901
	ABS Change	3.714	9.539	0.365	0.899	-0.668
	% Change	3.7%	9.5%	0.4%	0.9%	0.7%
Mesh 7	**TAWSS**	0.327	0.166	0.728	0.383	0.910
	ABS Change	0.239	3.154	-0.402	-0.140	1.000
	% Change	0.2%	3.2%	0.4%	0.1%	1.0%
MV /SB stenting without kissing						
Mesh 5	**TAWSS**	0.335	0.155	0.759	0.355	0.855
	ABS Change	▨	▨	▨	▨	▨
	% Change	▨	▨	▨	▨	▨
Mesh 6	**TAWSS**	0.348	0.164	0.731	0.364	0.851
	ABS Change	3.685	6.114	-3.579	2.426	-0.421
	% Change	3.7%	6.1%	3.6%	2.4%	0.4%
Mesh 7	**TAWSS**	0.351	0.169	0.728	0.371	0.856
	ABS Change	0.885	2.638	-0.449	1.857	0.536
	% Change	0.9%	2.6%	0.4%	1.9%	0.5%
MV /SB stenting with gentle kissing						
Mesh 5	**TAWSS**	0.332	0.143	0.726	0.359	0.854
	ABS Change	▨	▨	▨	▨	▨
	% Change	▨	▨	▨	▨	▨
Mesh 6	**TAWSS**	0.340	0.154	0.731	0.355	0.863
	ABS Change	2.591	7.413	0.716	-1.011	1.057
	% Change	2.6%	7.4%	0.7%	1.0%	1.1%
Mesh 7	**TAWSS**	0.352	0.161	0.731	0.368	0.866
	ABS Change	3.330	4.445	0.054	3.778	0.335
	% Change	3.3%	4.4%	0.1%	3.8%	0.3%
MV /SB stenting with aggressive kissing						
Mesh 5	**TAWSS**	0.318	0.161	0.729	0.391	0.989
	ABS Change	▨	▨	▨	▨	▨
	% Change	▨	▨	▨	▨	▨
Mesh 6	**TAWSS**	0.328	0.168	0.730	0.389	0.987
	ABS Change	2.951	4.043	0.147	-0.583	-0.224
	% Change	3.0%	4.0%	0.1%	0.6%	0.2%
Mesh 7	**TAWSS**	0.331	0.175	0.733	0.391	0.986
	ABS Change	1.029	3.979	0.480	0.537	-0.083
	% Change	1.0%	4.0%	0.5%	0.5%	0.1%

Table 2.3 TAWSS for selected regions in subsequent meshes of each CFD model. Simulations were conducted under resting blood flow conditions. Green indicates mesh independence, while red indicates the simulation did not achieve the desired criteria. Prox. – proximal LAD, Dist. – distal LAD, Side – side branch locations

2.3.1 Idealized time rendered velocity profiles

It is common for CFD studies of this type to examine velocity over the entire cardiac cycle in the form of volume rendered images. Images of blood flow velocity profiles for various stages of the cardiac cycle during resting and hyperemia are therefore provided for each model in APPENDIX A. In an attempt to more fully understand how different provisional stenting techniques affect the flow domain, velocity profiles at user-defined locations were selected and visualized. Figure 2.10 shows velocity profiles during maximum blood flow velocity for resting conditions. Each of the velocity profiles provides information about how blood flow is altered based on the various stenting procedures.

MV stenting with aggressive KB dilation increases the cross-sectional area of the MV. Flow into the system (vessel) is constant, using knowledge of basic fluid mechanics, flow is a function of velocity and area; the velocity within the elliptical region just proximal to the bifurcation is decreased due to the increased vessel area. Within the distal MV the velocity rendered profiles is skewed toward the carina. This observation is similar to that seen in normal bifurcation flow patterns (Figure 1.3). Additionally, the inlet to the SB (flow divider) is narrowed. Hence, the smaller SB area causes convective acceleration and increases the velocity just distal to the bifurcation.

The velocity renderings from MV and SB stenting without KB dilation is skewed toward the center of the vessel at the bifurcation, a notch is noticeable within the velocity profile in the MV near the carina; overall shape of the profile is blunted at this location. This observance is due to the SB stent protruding down in the MV. The SB stent protrusion causes flow to be redirected within the distal portion of the MV causing an abnormal flow pattern within the MV of this stented model.

The velocity rendering slice profiles from MV and SB stenting with gentle KB dilation is skewed toward the carina (flow divider) distal to the bifurcation area. The narrowing of the SB stent within the MV causes the velocity rendering slice profile within the SB to be skewed toward the lateral wall. When comparing the effects of no KB and gentle KB dilation, the MV and SB velocity rendering slice profiles change direction from normal bifurcation velocity profiles. Due to the 40% reduction in area, the velocity within the SB is also increased.

The MV and SB stented model with aggressive kissing experiences the same decrease in flow in the elliptical cross-section, due to the increased area as seen in the MV stented model with aggressive KB. The SB has a velocity profile which is skewed towards the carina, similar to the normal bifurcation profile, due to the straight configuration of the protruding SB stent into the MV.

Velocity profiles results observed under resting conditions are exacerbated by the introduction of hyperemia as shown in Figure 2.11. The trends revealed under resting conditions are amplified in hyperemia and the same conclusions about flow disturbances are present. Visually the most pronounced flow disturbance is the notch piece from the non-KB models distal to the bifurcation site. The extended MV stent alters the flow within those vessels causing an abnormal velocity rendering slice profile.

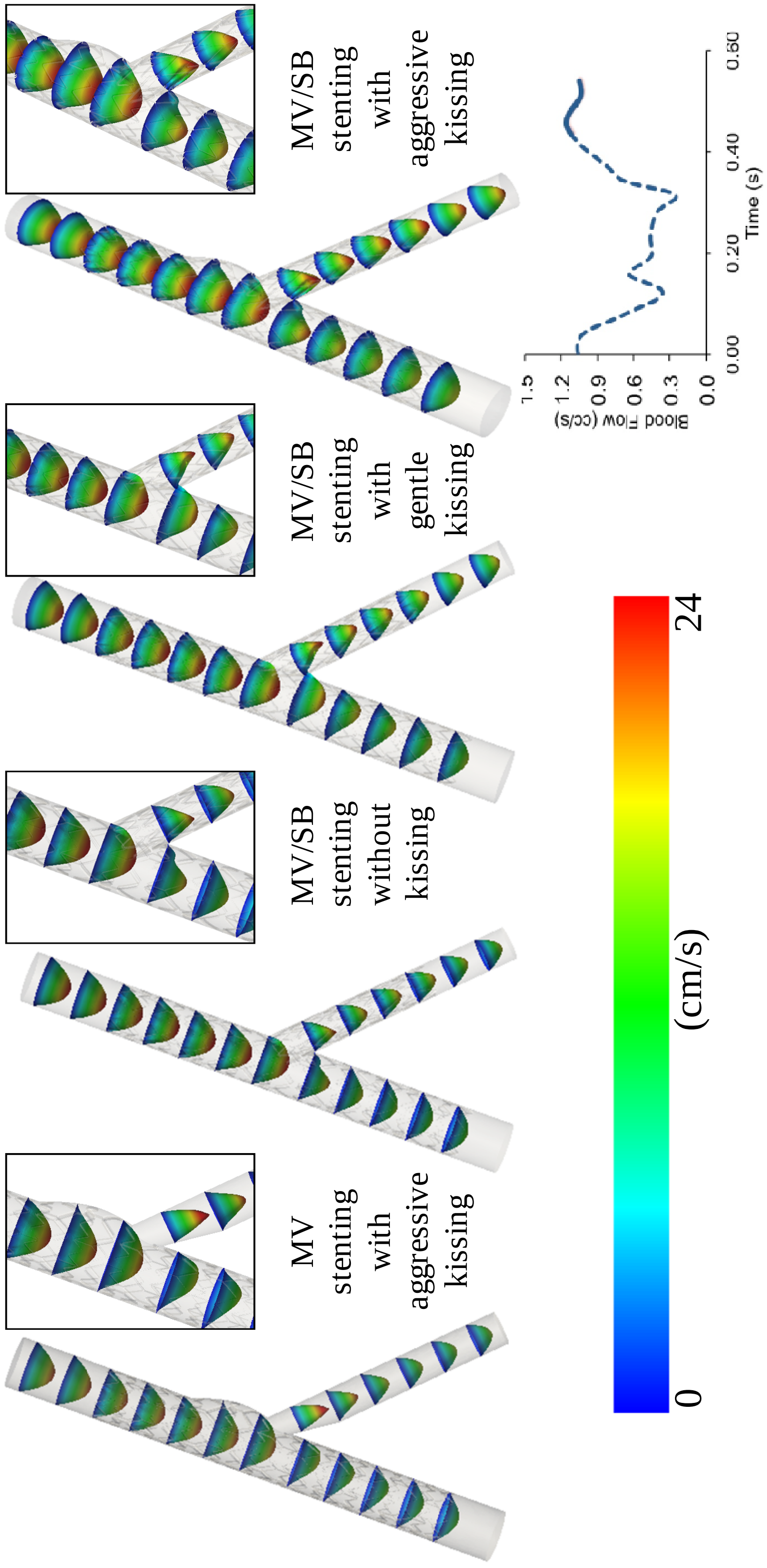

Figure 2.10: Velocity profiles at peak flow under rest conditions for each idealized stented model

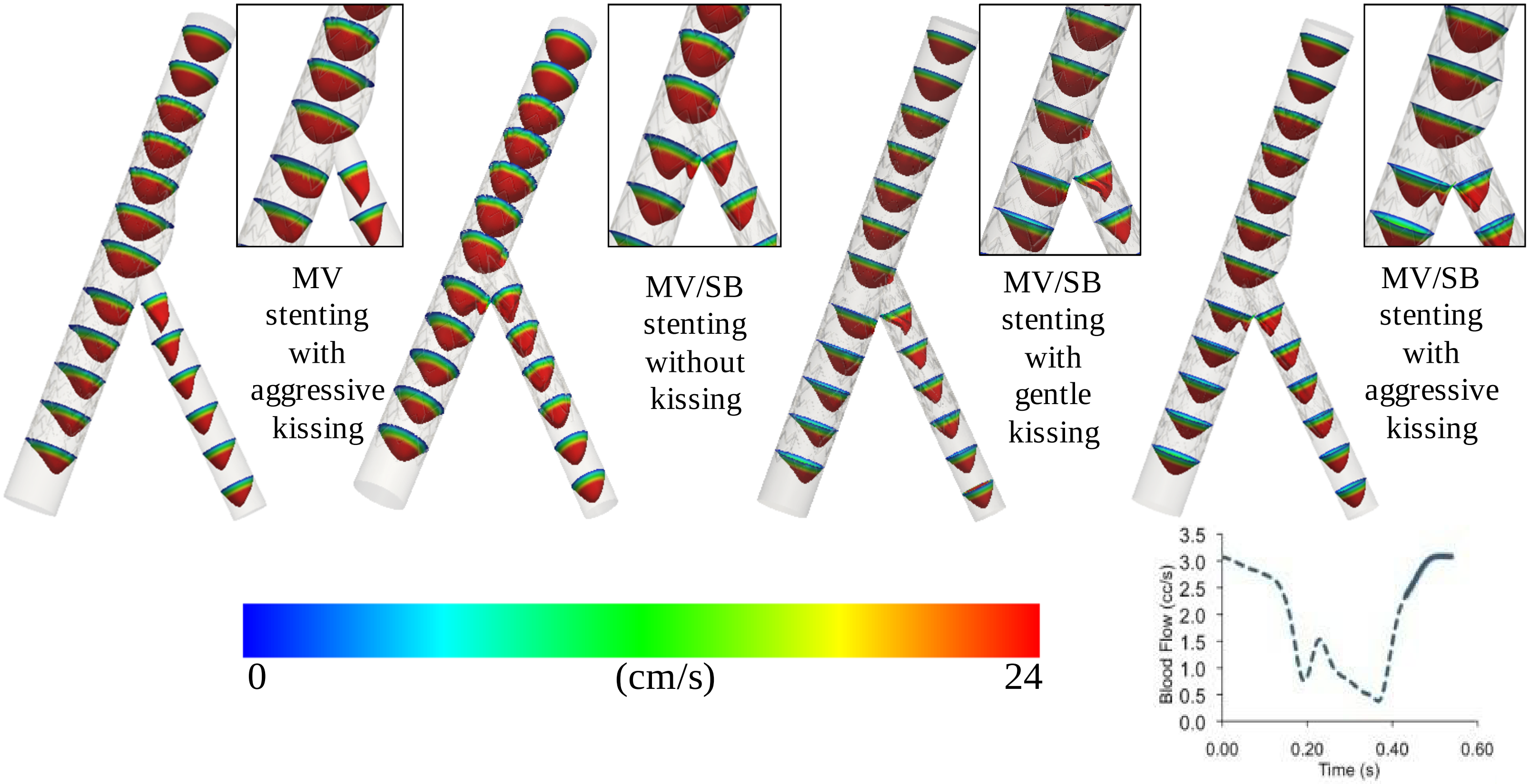

Figure 2.11: Velocity profiles during peak flow under simulated maximum vasodilation (hyperemia) conditions from a canine blood flow waveform.

2.3.2 Idealized time-averaged wall shear stress

Figure 2.12 shows patterns of TAWSS for each of the four idealized models. Results reveal high WSS along the inner wall of the flow divider and low WSS on the lateral or outer wall opposite the flow divider. For all models, within the MB, low TAWSS is observed distal to the bifurcation as well as opposite the flow divider. MB stenting followed by aggressive KB inflation shows increased areas of WSS within the over-expanded region. All MV and SB stented models shift area of low TAWSS distal to the bifurcation in the presence or absence of gentle kissing. In all stented regions there is a pattern of low TAWSS near and around the stent struts. Hyperemia (simulated exercise conditions) dramatically decreases overall area of low WSS but accentuates the impact of stenting techniques.

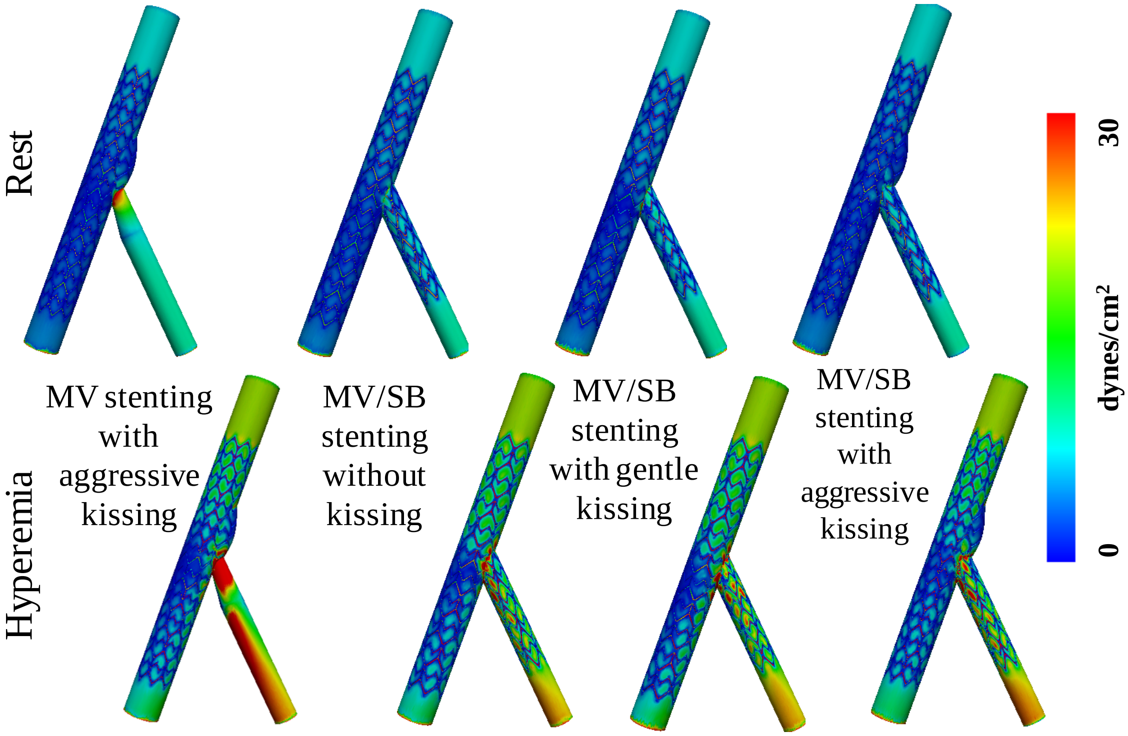

Figure 2.12: TAWSS for each idealized model under rest (top) and hyperemia (bottom) conditions

A definitive number has not been established for restenosis following stent implantation for the coronary vasculature; however, regions of TAWSS < 4 dynes/cm^2 have been shown to correlate with the localization of atherosclerotic plaque (Malek, Alper, and Izumo 1999; N, N, and MIM 2005). The percent area of the vessel wall subjected to TAWSS < 4 dynes /cm^2 under resting conditions is therefore shown in Figure 2.13. Approximately 50% of the total luminal surface was subjected to low TAWSS under resting blood flow conditions by including the stent in the MV. SB vessels which were un-stented had much lower TAWSS (~ 1 %) compared to those with stents (~30%).

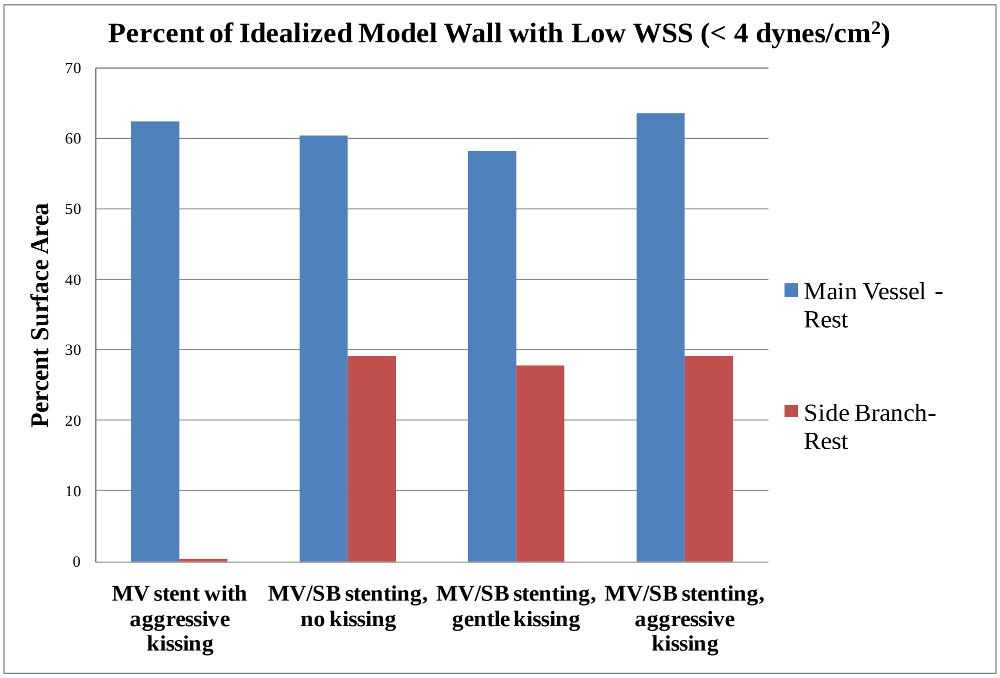

Figure 2.13: Percent of surface area exposed to areas of low TAWSS under resting conditions within the MV (blue) and SB (red)

The percent area of the vessel wall subjected to TAWSS < 4 dynes /cm^2 under hyperemia conditions is shown in Figure 2.14. Approximately 25% of the total luminal surface was subjected to low TAWSS under resting blood flow conditions by including the stent in the MV with subsequent aggressive KB techniques. Whereas, models with no KB or gentle KB had slightly lower amount (~20%) of total luminal area exposed to areas of low TAWSS. Un-stented SB had much lower TAWSS (~ 1 %) compared to those with stents (~12%), however, hyperemia decreased overall luminal area exposed to low TAWSS.

Vessels without stents were modeled to isolate the impact of vessel geometry relative to the stented geometries. Interestingly, vessel geometry accounted for only 5-10% of the vessel wall area subjected to low TAWSS under hyperemia and resting conditions, respectively. Therefore the presence of the stent contributed to the majority of area under low TAWSS.

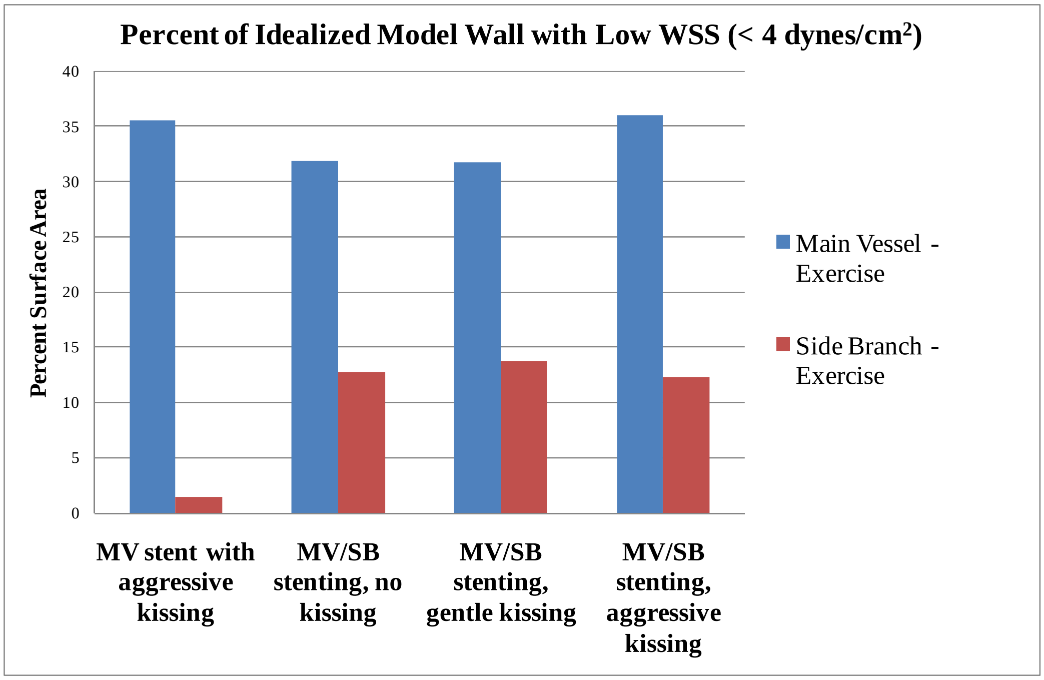

Figure 2.14: Percent of surface area exposed to areas of low TAWSS under hyperemia conditions within the MV (blue) and SB (red)

Idealized vessels were unwrapped to quantify and plot TAWSS for axial locations of 0, 90, 180 and 270 degrees as well as circumferential locations along the axis of the MV (Figure 2.15). Using Paraview, Matlab, and Excel, axial points on the model surface TAWSS results file were queried and plotted (Figure 2.17). Queried circumferential locations were selected at the inlet and outlet locations, as well as at analogous micro and macro strut locations both proximal and distal to the bifurcation (Figure 2.18)

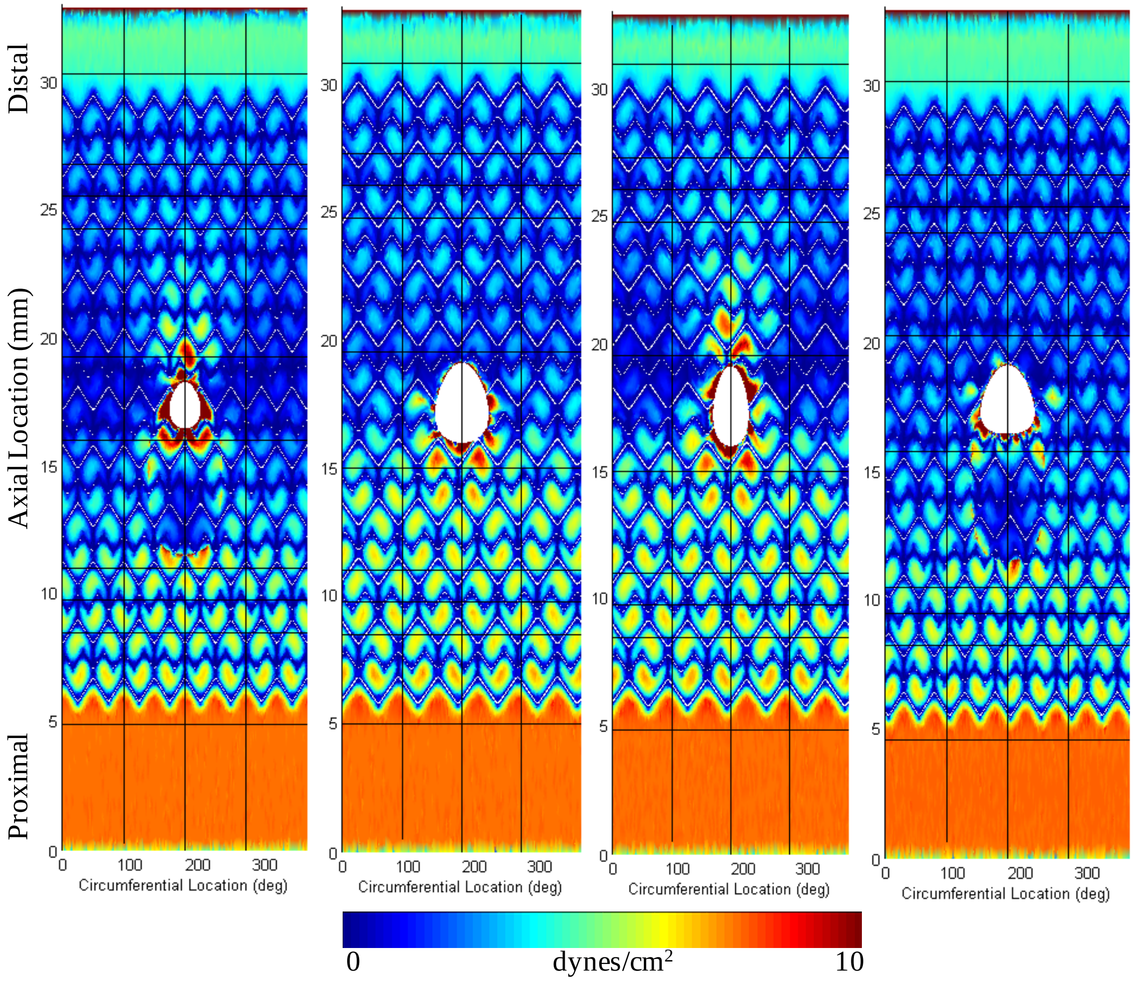

Figure 2.15: Unwrapped representation for distributions of time-averaged wall shear stress under resting conditions. The figure shows locations of each quantification site in mm down the axial length of vessels as well as at circumferential locations in degrees for the main vessel

Additionally, idealized vessels in the side branch were quantified and plotted (Figure 2.16) axially at locations of 0, 90, 180 and 270 degrees (Figure 2.17) and queried at circumferential locations (Figure 2.19). Circumferential locations were selected at analogous micro and macro strut locations as well as an outlet location, for both stented and unstented models. Using Paraview, Matlab, and Excel, points on the TAWSS surface results file were queried and plotted for the SB under rest conditions (Figure 2.19).

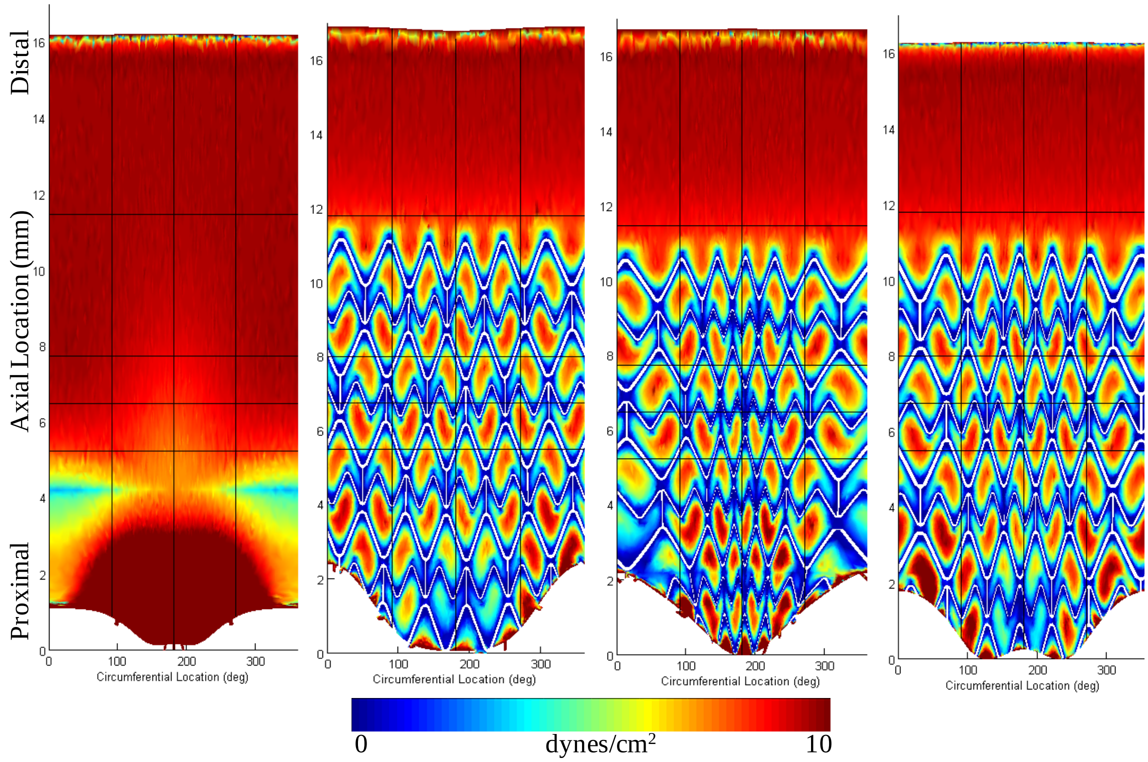

Figure 2.16: Unwrapped vessel geometries with locations of each quantification site (rest) for mm down the vessel and circumferential locations in degrees in the side branch vessel.

Within the MV, the axial plots show areas of low TAWSS on the stented regions of the luminal surface. The general trend within the MV is higher values of WSS in the proximal vessel (~ 75 dynes/cm^2), a lowering of WSS distribution at the bifurcation region (~ 35 dynes/cm^2) and then a gradual increase in WSS at the outlet (~50 dynes/cm^2). The axial WSS distributions within the SB are generally high at the inlet (~ 150 dynes/cm^2) where fluid bifurcates from the MV into the SB. The stented SB models show the same trend as the stented regions within the MV, with fluctuating values of WSS between stent struts. Overall, values of WSS are high right at the bifurcation and then drop to about 50 dynes/cm^2 and then gradually increase to about 100 dynes/cm^2.

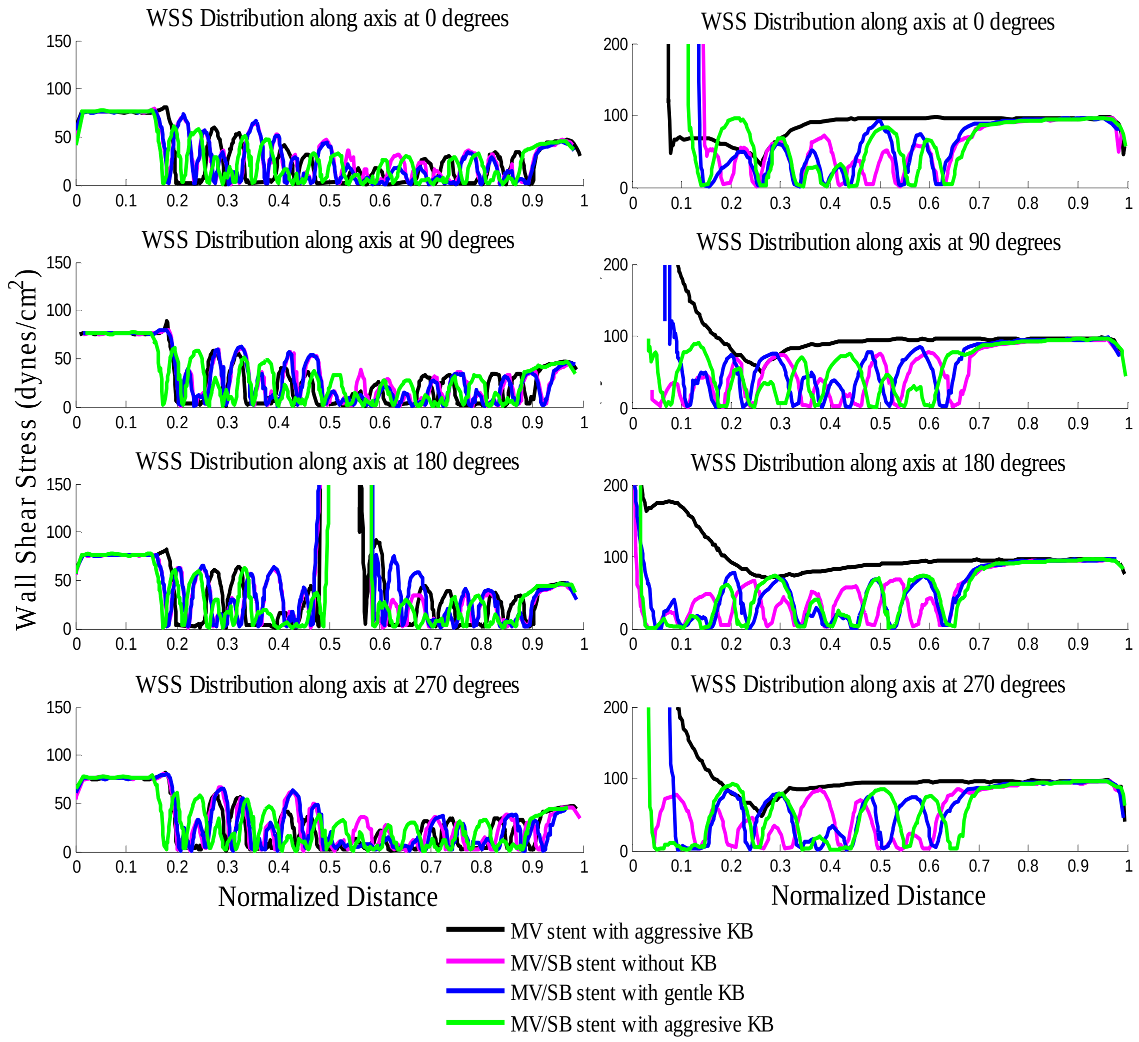

Figure 2.17: Axial WSS distributions in the MV (left panel) and SB (right) panel for all four idealized models under resting conditions.

Figure 2.18 illustrates the distribution of WSS at circumferential locations along the MV. The inlet and outlet values of WSS remain constant, however, the inlet is consistently higher (75 dynes/cm^2) compared to the outlet (45 dynes/cm^2). Overall, higher values WSS are seen at proximal locations compared to analogous distal locations. Interestingly, two models (MV-stented model with aggressive KB and the two-stented model with gentle KB) showed increased WSS at both proximal and distal ostial locations due to the decreased SB entrance area.

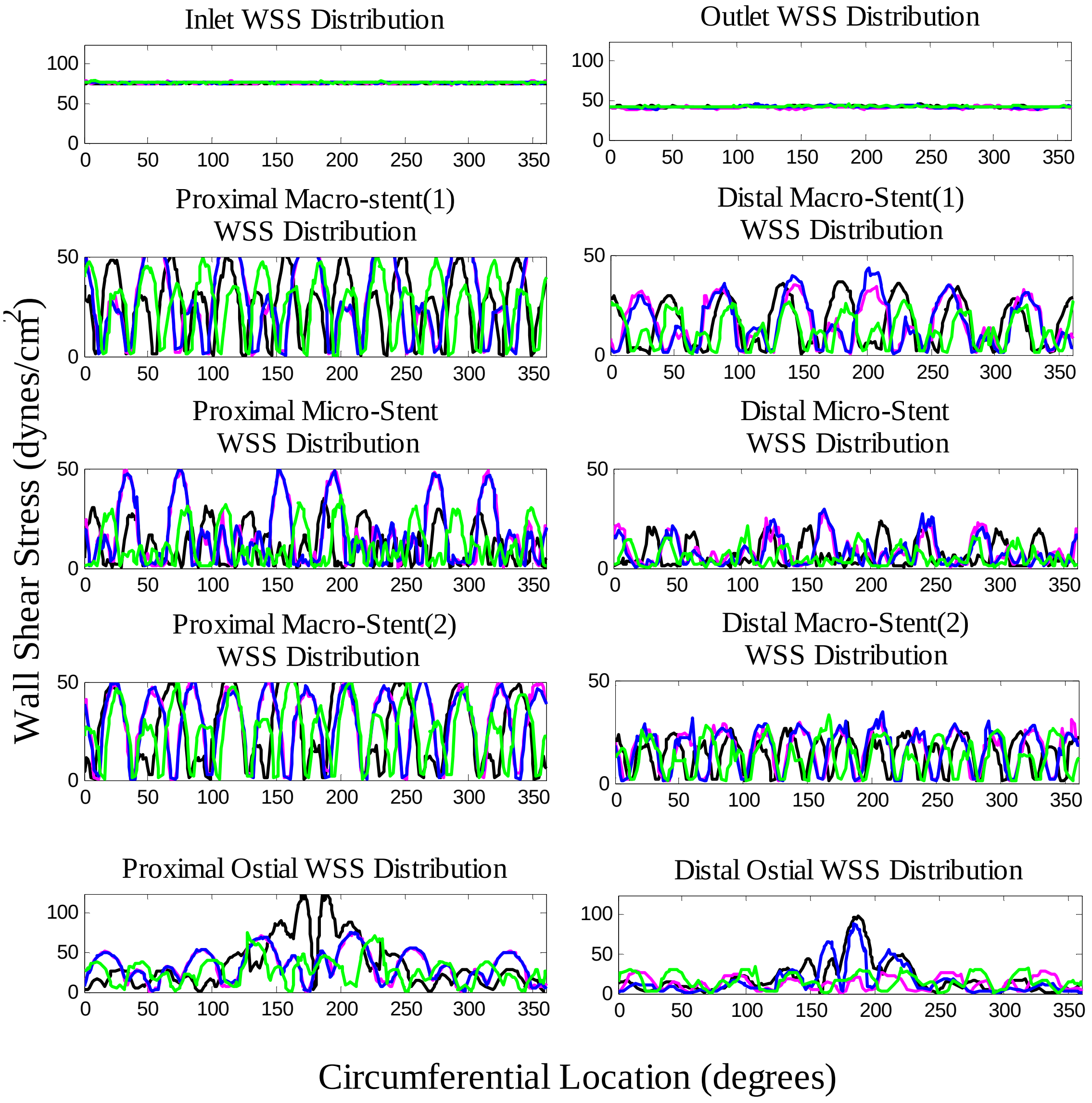

Figure 2.18: Circumferential graphs of WSS at selected locations along the main vessel. Please note the change in axis scale to better visualize the distribution of WSS at several locations. The key is the same as above for corresponding colors to vessels.

Figure 2.19 shows SB WSS distributions at varying circumferential locations. The stented models show fluctuations in WSS values within strutted areas going from peak values to zero dynes/cm^2. The outlet WSS values for the stented SB models were all slightly lower than the unstented SB model. These results correspond to the same patterns of WSS distributions within the MV.

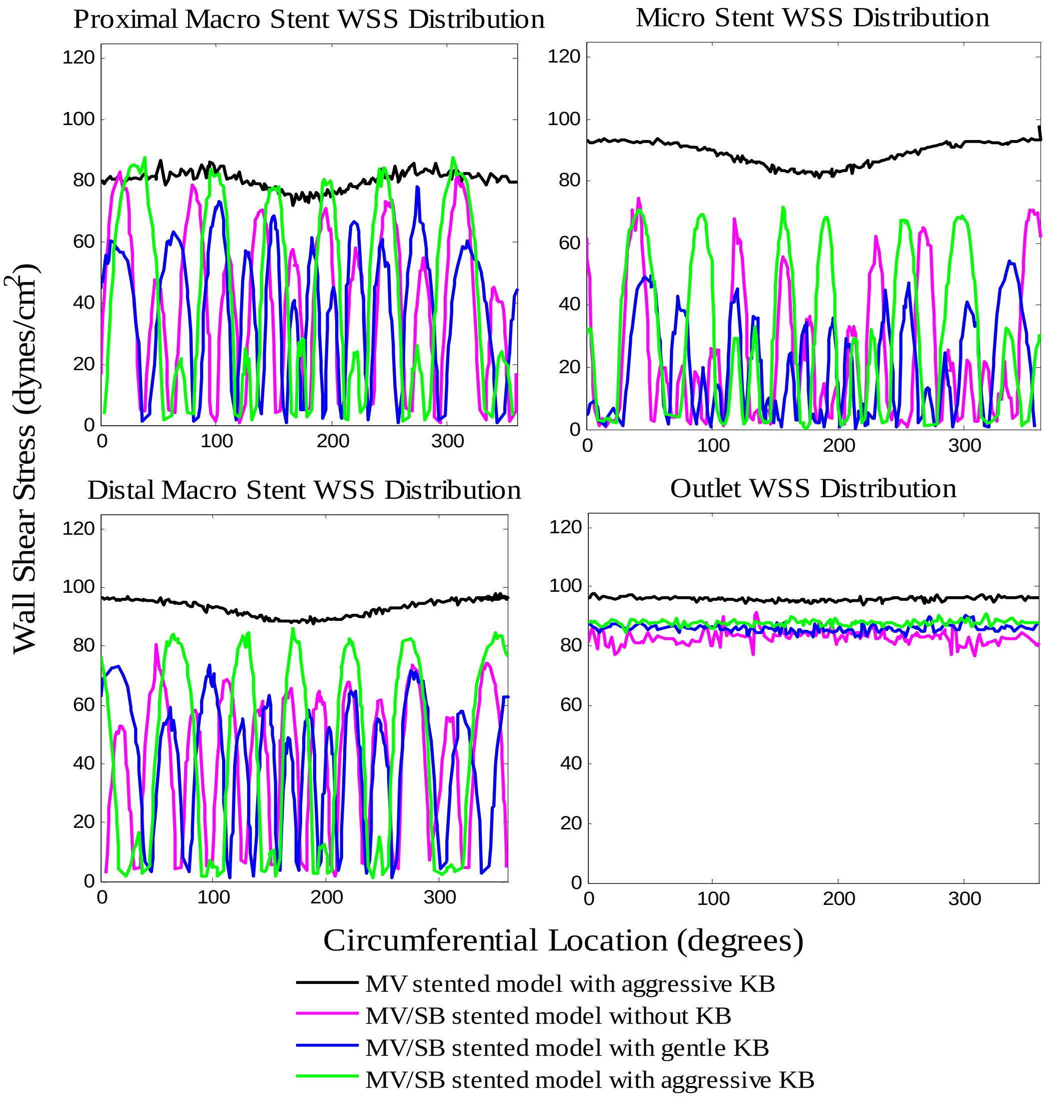

Figure 2.19: Circumferential graphs of WSS at selected locations along the side branch.

2.3.1 Idealized oscillatory shear index

Figure 2.20 illustrates the distribution of OSI in each idealized vessel. Stenting introduces high values of OSI near the stent struts (~0.2) and the skewing of the flow profile creates areas of high OSI (0.2 -0.4) opposite the carina. Gentle KB dilation of the SB moves the carina back into the LAD and reduces the localization of high OSI especially under rest conditions. Areas of high OSI are dispersed more evenly with the addition of the kissing dilation, but values are still around 0.2 at the site of bifurcation. However, a new area of high OSI, but smaller in size, is created on the LAD side of the carina. Exercise accentuates areas of high OSI.

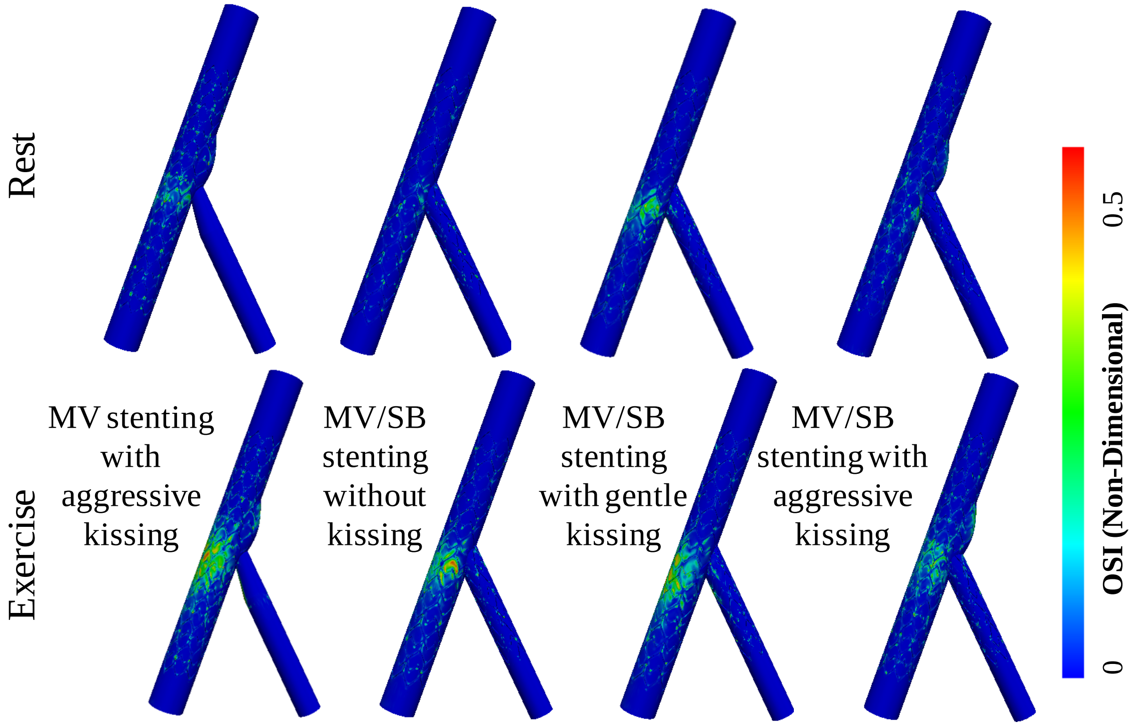

Figure 2.20: OSI of idealized models under rest and exercise conditions

Figure 2.21illustrates the percent of surface area of each model and their corresponding values of high OSI (> 0.1) in each idealized vessel. Stenting introduces high values (~3%) of OSI in the MV under rest conditions. SB stented models showed higher OSI values (~1) compared to unstented SB models (~ 0). Interestingly, MV and SB stenting with gentle KB had a higher percentage of total luminal surface are exposed to high OSI (~3%) compared to the other two-stented models (~1%). Overall, the percentage of luminal area exposed to high OSI is small (< 5% total surface area). Hyperemia conditions heighted areas of high OSI for both the main vessels (~10%) and side vessel (~2%) as shown in Figure 2.22.

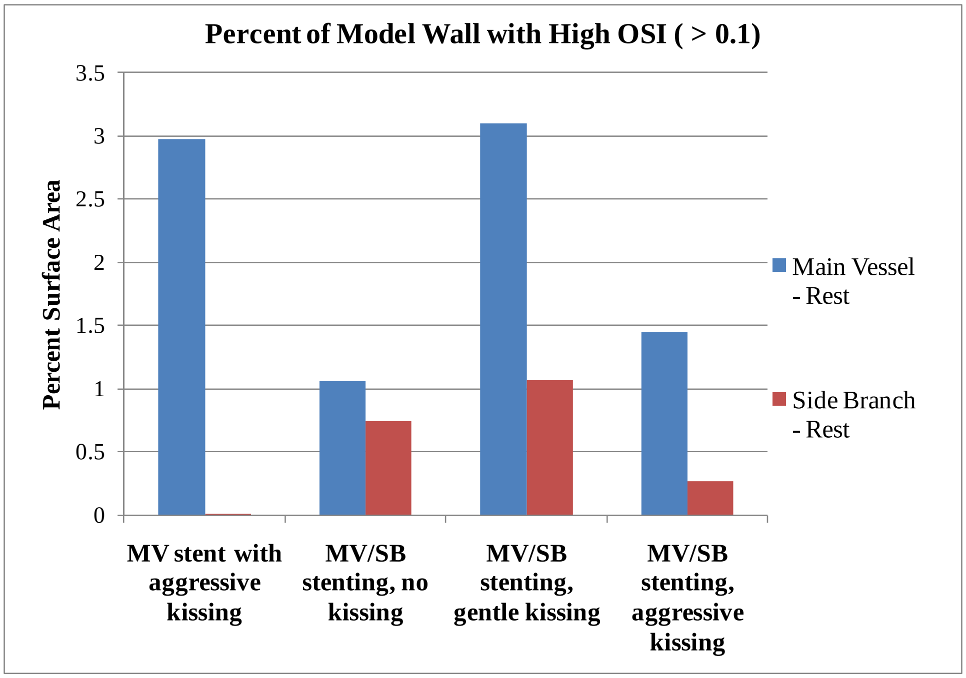

Figure 2.21: Percent of luminal surface area with areas of high OSI under resting conditions.

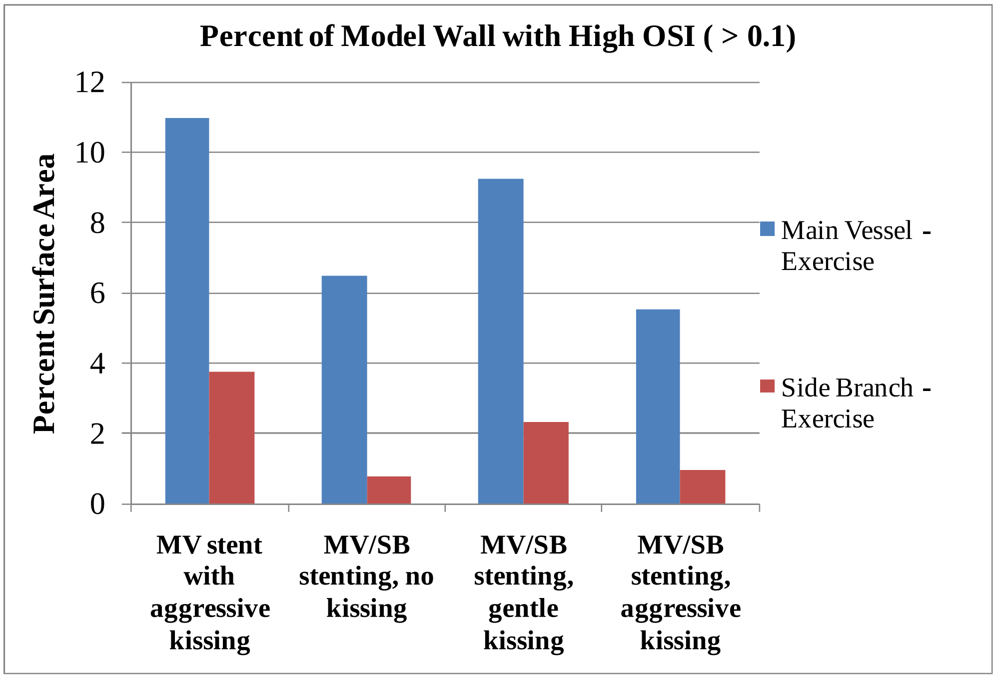

Figure 2.22: Percent of model luminal surface area with areas of high OSI under hyperemia conditions.

FFR was not quantified for these models because the maximum reduction in diameter was only 40%. Values of FFR are only clinically relevant for stenosis of 70% or greater. Therefore, quantification of FFR or severity of stenosis is not applicable to these idealized models.

2.4 Summary of Specific Aim 1

CFD analysis performed on idealized models illustrates the effects of single and multiple stent implantations on velocity profiles, indices WSS and OSI. Stented regions accounted for the majority of the vessel wall area subjected to low TAWSS under resting and hyperemia conditions (Figure 2.12). This analysis shows that velocity profiles near the bifurcation are influenced by the location of the stent struts as well as the positioning of the SB stent and how far it protrudes into the MV. The velocity flow profiles were locally altered based on SB stent placement and exacerbated under hyperemia conditions.

This quantification revealed that total luminal area exposed to low TAWSS was essentially the same between single and two-stented models regardless of the KB technique applied. KB cause an ~3% increase in the total area of the MV exposed to low WSS which may or may not impact local patterns of restenosis or thrombus potential in a clinical setting. Ge et al. compared using the final KB dilation to the absence of KB technique. Their research showed that PSB techniques with KB is associated with a lower rate of restenosis in SB, as well as lower rates of MACE and need for revascularization (Ge et al. 2005). Currently, no long-term studies have focused their aims at investigating a correlation between final KB dilation and restenosis rates. Our results indicated a potential for MV restenosis to be more pronounced after performing

KB technique from the TAWSS rates inflicting an overall greater area than in the non- or gentle KB vessels. These findings highlight an important distinction between the overall geometry of a vessel created after stenting and the specific impact of the stent. Ultimately, these simulations indicate that different stent designs, stent placements and subsequent provisional techniques have the impact to alter areas of TAWSS in bifurcation lesions. Knowledge of overall changes hemodynamic indices related to stenting has the potential to optimize stent design for various bifurcation lesions.

CHAPTER 3 : SPECIFIC AIM 2

3.1 Background

The challenges associated with treating bifurcation lesions suggest that devices could be specifically designed for this area of the vasculature. In order to improve device design a thorough understanding of coronary bifurcation morphology is required. To date a modest number of studies have employed the used of 3D imaging such as, 64 multi-slice computed topography (MSCT) images (Kawasaki et al. 2009; Matsunaga et al. 2009). CT offers an additional dimension for complete vascular reconstruction, but has not been used to create a comprehensive description of coronary morphology to date. Additionally, no universal standard has been proposed on how to measure certain quantities, particularly bifurcation angles (Kawasaki et al. 2009; van der Waal et al. 2009). The current study formulated and applied a robust protocol to extract 3D metrics that can be reproduced despite having relatively heterogeneous patient specific data, thereby reducing quantification time and diminishing user variability inherent in many protocols. Having a broader knowledge of coronary morphometric parameters can ultimately be used to enhance the stent design process.

3.2 Methods

The workflow developed to characterize bifurcation morphology is shown below. The proposed method uses several software packages to generate computational models and quantify local vessel properties (

Figure 3.1). Additional details are provided in the subsequent sections below.

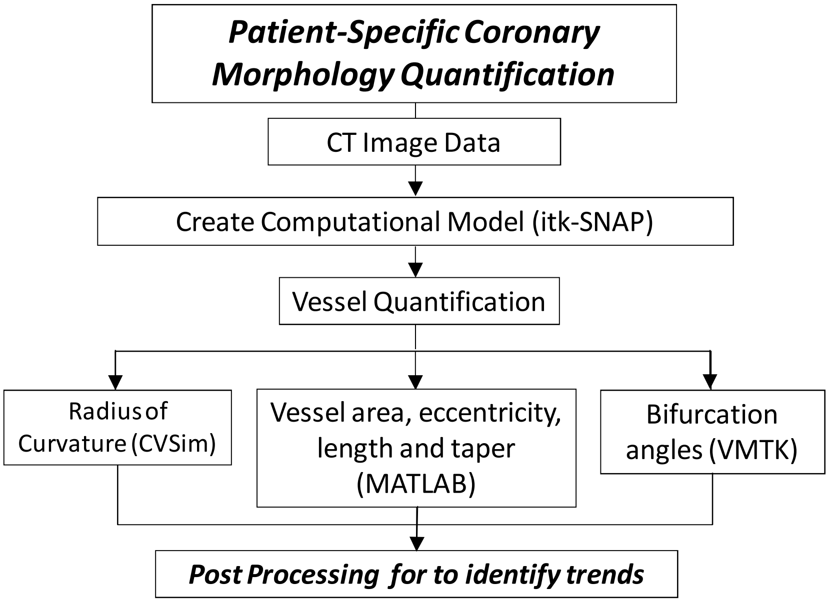

Figure 3.1: Schematic of vessel morphology quantification workflow from image-based data.

3.2.1 Study Population and Imaging Acquisition

Specific aim 2 used data obtained from human subjects (n = 22) imaged with a 64 MSCT scanner at Froedert Hospital and the Medical College of Wisconsin in Milwaukee, Wisconsin using conventional CT imaging parameters. All subjects gave written informed consent and Institutional Review Board (IRB) approval was obtained by the principal investigator and his collaborators prior to use of patient-specific imaging data for this investigation. All patient indicators were excluded from imaging data during post processing and therefore complied with all Health Insurance Portability and Accountability Act (HIPAA) regulations.

Only arteries that were characterized as normal by the cardiologist who performed the imagine acquisition were used for the current investigation. Hence, arteries that does not exhibit severe plaque burden with the associated cardiology report were included. Vessels were excluded if they were documented as being short, inflicted with a 50% or greater stenosis and if big septal branches were close to the bifurcation region. Septal branches are those which jut into the myocardium which is not consistent for all coronary bifurcations.

3.2.2 Computational Model Generation

Morphology was quantified for three left coronary artery (LCA) bifurcation sites. These sites are commonly associated with experiencing CAD: the left anterior descending (LAD) and left circumflex arteries (LCX) from the LCA, as well as their respective first branches, the LAD and first diagonal (D1) and the LCX and obtuse marginal branches (OM). An anatomical reference is shown in Figure 3.2.

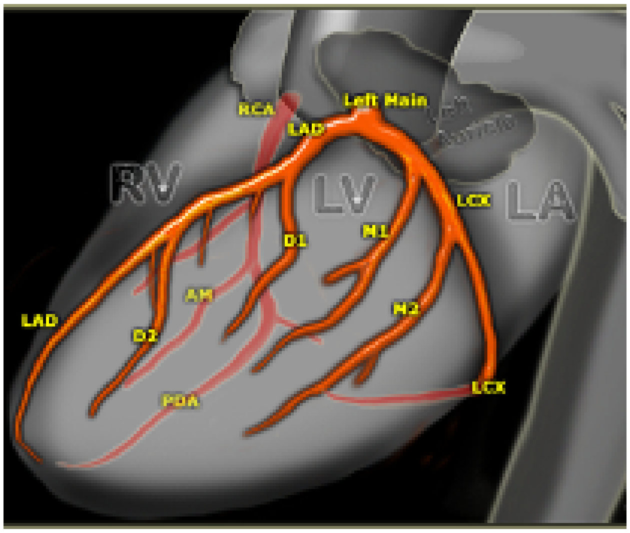

Figure 3.2: Anatomical location of the LMCA tree with relation to the heart. Adapted from the radiologist assistant (http://www.radiologyassistant.nl).

Grayscale CT image data was imported into ITK-SNAP (Yushkevich, P.A., University of Pennsylvania) as DICOM files. ITK-SNAP is an open source software application which applies active contour segmentation to imaging data to generate 3D computational models as illustrated in Figure 3.3.

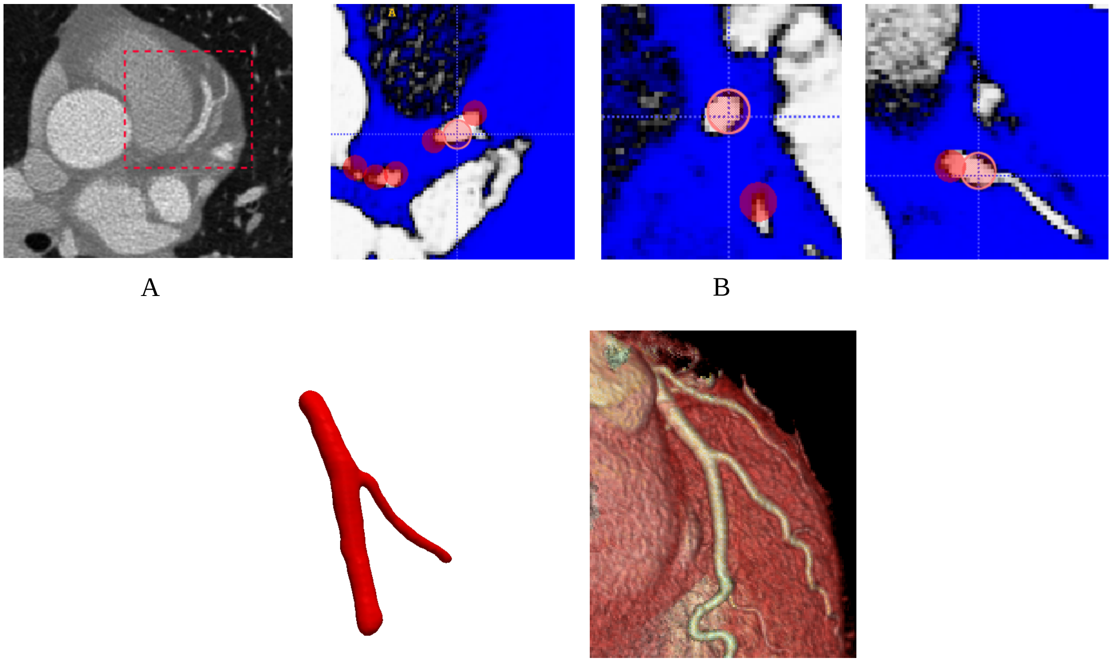

Figure 3.3: Generation of a computation model from CT data. Steps include defining a region of interest (A), placing seeds for snake initialization in axial, sagittal and coronal planes (B; left to right respectively), and visually verifying the computational representation created by snake initialization (C) relative to volume rendering from a commercial workstation (D).

A region of interest (ROI) was identified within the image data containing the location of the vasculature to be segmented. The vasculature was delineated by using thresholding and level set segmentation processes within the software. Spherical bubbles were then placed within the luminal area of each bifurcating vessel to initialize a snake algorithm (Yushkevich et al. 2006). The segmentation process was completed by choosing relative weights of different types of velocities to control the snake algorithm.

All bifurcations were segmented using the semi-automated method with manual modifications as required after the segmentation process to accurately portray the vessel ROI. Differences between data sets required parameter adjustment; specifically if the image data ROI had a large gradient in intensities. The large gradient required different thresholding values which changed based on the intensity ranges. Velocity parameters are determined by the operator and are slightly different for each data set. Once the segment has evolved to containing the area of the vasculature and the desired smoothness specified by the operator is achieved, then the computational representation is complete.

3.2.3 3D Geometric Quantification from Computational Model

A Changing file formats to comply with software architecture

Computational representations were imported into Paraview (Kitware, Inc.) where the file was saved with the extension of appended visualization toolkit polygonal (VTP) data files. This file-type is required for further analysis using the vascular modeling toolkit (VMTK). VMTK was developed and currently maintained by Luca Antiga (Medical Imaging Unit, Bioengineering Department, Mario Negri Institute, Bergamo, Italy) and David Steinman (Biomedical Simulation Lab, Mechanical & Industrial Engineering, University of Toronto, Ontario, Canada). VMTK is an open source software which allows for vessel centerlines and bifurcation angles to be delineated and quantified (Antiga and Steinman 2004).

B Centerline Calculations using VMTK

Centerlines are useful representations of the shape of vessels. 3D skeletonization provides an illustrative description of the definition of a centerline; however, the mathematical definition of a centerline is not a unique calculation among researchers. Many methods have been proposed in the literature for the computation of centerlines both from angiographic images and 3D models (Choi et al. 2009; Kawasaki et al. 2009; Long et al. 2003). The algorithm implemented in VMTK computes centerlines starting from surface model rather than by an operator.

Centerlines in VMTK are determined as weighted shortest paths traced between two extreme points. In order to ensure final lines are in fact central, the paths cannot just lie anywhere in space, but are bound to run on the Voronoi diagram (Figure 3.4) of the vessel model; this is the place where the centers of maximal inscribed spheres are defined. A sphere inscribed in an object is said to be maximal when there is no other inscribed sphere that contains it. Every point grouped to the Voronoi diagram has a sphere centered in that point that is a maximal inscribed sphere. Centerlines were generated within the software by determining the center of maximal inscribed spheres that approximated the diameter along the length of each vessel. The use of VMTK allows for fast and operator independent centerline generation, making the process more robust.

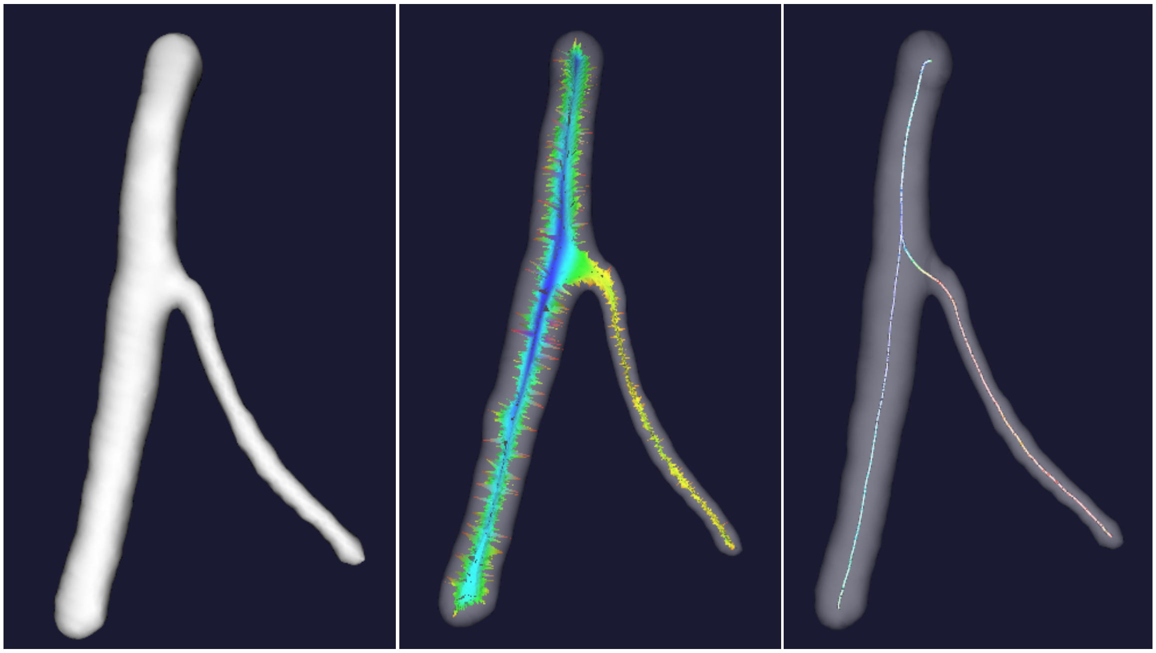

Figure 3.4: Solid model (left), Voronoi diagram (middle) and centerline within opaque model (right) of a patient-specific LAD/D1 bifurcation extracted using VMTK.

C Bifurcation Angle Extraction using VMTK

The centerlines obtained from VMTK were then used to calculate vectors normal and tangent to a defined bifurcation plane. The out-of-plane bifurcation vector angle was classified as the angle between the bifurcation vectors and the bifurcation plane in radians. The difference of in-plane angles from the daughter vessels was used to obtain bifurcation angles (Thomas et al. 2005). Centerlines were used to obtain geometric characteristics including vessel length and area in planes perpendicular to the centerlines. The bifurcation sites were characterized as the bifurcation vectors (x,y,z point locations) output from VMTK from the bifurcation angles. This data provided fast and operator-independent characterizations of the bifurcation angles for the vessels investigated.

D Vessel Quantification

Vessel quantification was accomplished by providing three inputs, a surface file (.vtk), centerline (.csv) point information, and bifurcation vectors values (.dat), to a number of scripts written in Matlab. The desired geometric measurement at surface points were taken from the smoothed VTP file and converted into a VTK surface mesh. The centerline points were exported as comma-separated value (.csv) files; both the surface and centerline files were created in Paraview.

The surface mesh, centerline points and bifurcation vectors were then loaded into Matlab in their respective formats (.vtk, .csv and .dat, respectively). Custom algorithms were used to separate the centerline paths into a main branch, side branch, ostial region and parent vessel segments. After the vessel was separated each segment was quantified individually. Circumferential slices were extracted at 1 mm measurements along each branch, except the ostial region which was in which measurements were extracted every 0.5 mm (Figure 3.5). Metrics quantified were vessel length, area, eccentricity, and taper factor.

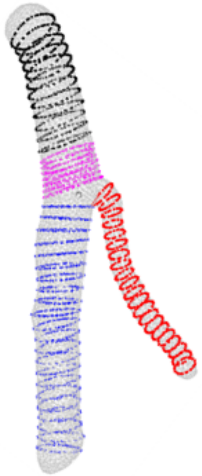

Figure 3.5: Representative vessel for which circumferential slices were taken proximally to distally along the centerline paths extracted from VMTK. Black denotes the proximal vessel, magenta the ostium, blue the distal vessel and red the side branch quantification locations.

Area was measured using the circumferential slices and the polyarea function, an inherent function within the Matlab architecture, which uses x and y points to find the area of a polygonal shape. Area measurements were then used to extract diameter and radius for branching law calculations according to Murray and Finet, which is represented as: $(R_{parent}/(R_{daughter1} + R_{daughter2}))$. Vessel length was taken as the number of collected slices down each vessel segment.

Taper is can be described as a change in area over a change in length which gives a quantifiable measure of how much a vessel changes proximally to distally. Several investigators have taken different approaches when quantifying taper (Fung 1997; Zubaid, Buller, and Mancini 2002). The taper calculation used for this study was based on the work done by Fung, where taper was described as index coined a *taper factor*, which was determined using an exponential function based on vessel area and radius. Fung's equation is:

$$A = A_o e^{(-B*x/Ro)} \qquad \text{Equation 3.1}$$

A is the area of vessel segment, A_o and R_o are, respectively, the inlet area and radius at the most proximal location, x is the distance from that upstream site and B is the taper factor previously described (Fung 1997).

Eccentricity has previously been characterized by several researchers (Miller et al. 2008; Yamagishi et al. 2002) using equation 3.2, which describe eccentricity using maximum and minimum radial distances. An eccentricity index (EI) was quantified at each circumferential location which describes how elliptical or circular the cross-sectional area of the vessel.

$$EI = (R_{max} – R_{min})/R_{max}) \qquad \text{Equation 3.2}$$

Most studies used intravenous ultrasound as the method for obtaining lumen distance. In the present study lumen distance was calculated from the vessel segment slices along each section using a standard distance equation.

Radius of curvature was quantified by incorporating the extracted centerline points, turning them into paths files from scripts written in Matlab and loading them into CVSim. Choi et al. were able to solve for radius of curvature using centerline path information by solving the inverse of the radius of an osculating circle, which was approximated by a circle passing through three points on the vessel centerline path. For the current investigation the bifurcated vessel centerline was partitioned into a MV and SB centerlines. Global curvature was then calculated using a window size, which was defined as the average diameter of the vessel. The output from this CVSim was one mean value for each vessel curvature examined (Choi et al. 2009). Mean radius of curvature is reported for vessel curvature in this investigation.

Physiological systems such as the coronary tree exhibit a high degree of organization. There have been numerous attempts to explain and to quantify the design of the vascular tree (Finet et al. 2008; Kaimovitz et al. 2008; Murray 1926). These theoretical models provide relationships between PV diameters and corresponding daughter vessels (MV and SB). Murray derived an optimal condition for vascular bifurcations based on the principal of minimum work, known as Murray's Law (Equation 2.1). It states that the cube of the diameter of the PV equals the sum of the cubes of the diameters of the daughter vessels. Finet et al. proposed a linear relationship between the different vessel diameters for coronary bifurcations which is easier to use in clinical practice (Finet et al. 2008). Finet found the ratio of parent radius over the sum of daughter radii to be 0.678 based on angiographic data for all coronary arteries. Diameter and radius calculations were quantified and applied to both Murray's law and Finet's ratio equations for the current study.

3.2.4 Post Processing Data

Standard assumptions were made about the vessel data quantified. All data were assumed to be normally distributed, stationary, have equal variance and be statistically independent. Knowledge of any anomalies were either noted or rejected from the analysis. Confidence in these assumptions was tested using the non-parametric runs test and the chi-squared (goodness-of-fit) test.

The runs test determines the randomness of a data sets distribution. More precisely, it can be used to test the hypothesis that the elements of the sequence are mutually independent. The data was partitioned into groups based on if values within the data were above or below the mean value. Too few runs indicate a tendency for high and low values to cluster. Too many runs indicate a tendency for high and low values to alternate.

A chi-square test was used to prove the hypothesis that the vessel data comes from a normal distribution with variance a known variance. The data sets were tested against the alternative that the values come from a normal distribution with a different variance. Results from the chi-square test will dictate whether parametric or non-parametric statistical analyses are performed.

Parametric hypothesis testing was performed on normally distributed data, verified based on the chi-square testing outcomes. Geometric variables, averaged across all patients, were compared using one-way analysis of variance (ANOVA) and paired t-test. Due to the inherent variability across all patients, nonparametric hypothesis testing was performed on all data to confirm that true trends were revealed. The Wilcoxon signed-rank test is a nonparametric alternative for two paired samples and is analogous to the student's paired t-test. A nonparametric test for comparing multiple independent samples is the Kruskal-Wallis test. This procedure is analogous to the parametric ANOVA hypothesis test. The utility of both parametric and nonparametric testing ensures significant differences between and within geometric properties are discovered. Statistical significance was defined as $P < 0.05$. All testing was performed using Matlab.

Statistical analysis can be skewed by outliers and abnormalities within the data, which can be misrepresented and conceal true trends of the most often presenting values for indices of vascular bifurcation morphology. A joint probability density function (JPDF) provides a visual and intensity scalar representation of the largest commonality among paired metrics and was therefore employed here. However, despite presenting the data from two characteristics as seen with the JPDF, the collective qualities of these vessels may still differ. Thus, to further determine how all metrics are connected and decipher where the data naturally partitions based on all input characteristics (i.e. geometric properties), clustering analysis was implemented. Two clustering approaches were taken; hierarchical and k-means clustering. Hierarchical clustering groups multiple input variables together based on Euclidian distances. The distances are then linked according to the un-weighted averages of those distances. K-means clustering uses an iterative partitioning approach which minimizes the sum over all clusters, by taking the Euclidean distances of those point-to-centroid sums. Logically, when comparing the individual vessel data (PV, DV, SB and Ostium) ideally three bifurcation sites should be grouped. Additionally when comparing geometric properties from the entire bifurcation site (LCA, LAD and LCX) four individual vessel segment groups should emerge. Using this logic, clustering analysis was performed by setting the number of groups for partitioning to 3 and 4 when clustering the individual vessel segments and whole bifurcation sites, respectively.

The final tool incorporated within this analysis is the utility of principal component analysis. One of the difficulties inherent in multivariate statistics is the problem of visualizing data that has many variables. For data sets with several variables, groups of variables often can be grouped together since more than one variable might be reflective a driving principles governing the behavior of the system. In many systems there are only a few such driving forces, but an abundance of measurements allows for several measures of system variables. Multiple variables can be simplified by replacing a group of variables with a single new variable.

Principal component analysis is a method for attaining a measurable value of what variables influence the system. This procedure generates a new set of variables, principal components. Each principal component is a linear combination of the original variables. All the principal components are orthogonal to each other, so there is no redundant information. Using built in functions within the Matlab architecture provides a simple way to calculate principal components from the geometric properties quantified in the current investigation.

3.3 Results

A total of 63 computational models from three LMCA bifurcations were generated during this investigation and used to obtain geometric properties. A group of representative computational models are displayed in Figure 3.6. Vessel length, area, taper, and eccentricity are reported in Table 3.1. Parametric statistical analysis was performed on all quantified geometric parameters and reported in Table 3.1.

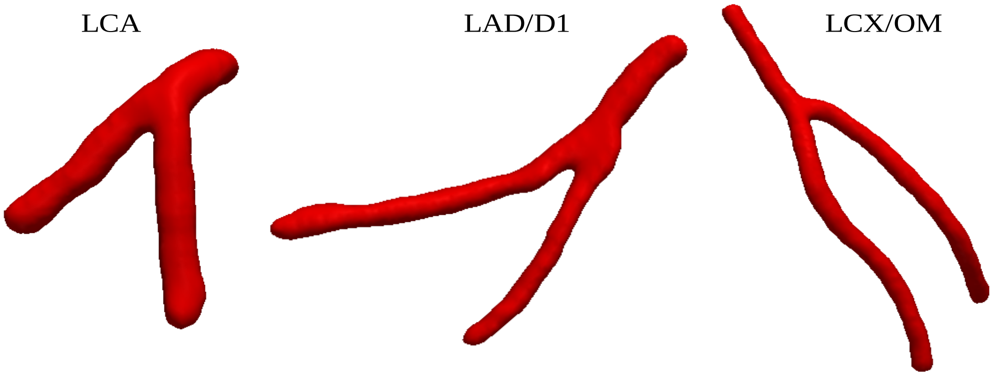

Figure 3.6: Representative computational models from CT image data, used to quantify vessel geometric properties.

The outcome of the runs test showed vessel length for each bifurcation site (LAD/LCX, LAD/D1 and LCX/OM) were not considered random. Alternatively, individual vessel segments (PV, DV, SB and OS) were considered random. Bifurcation angles (both DIA and PIA) were not considered random (P =0.4 and P = 0.17, respectively). After performing a runs test on mean radius of curvature for both the MV and SB vessel segments both vessel segments were not random (P = 0.01 and P = 0.03, respectively).

Data classified as random from the runs test, required a chi-square ‘goodness-of-fit’ test to determine if the underlying distribution could be considered normal. Vessel area, length, bifurcation angles and radius of curvature data were considered to have normal distributions after performing the chi-square test, confirming the utility of parametric testing for this investigation.

Results from parametric statistical testing (one-way ANOVA and paired t-tests) showed that within the LCA and LCX/OM bifurcation segments; vessel area of DV and SB are less than PV and Ostium, and the DV and SB are longer than the PV and Ostium. Within LAD/D1 bifurcation segments, vessel areas of SB are less than PV, Ostium and DV vessel segments. Additionally, vessel lengths for the LAD/D1 from the DV and SB are longer than PV and Ostium.

Between specific bifurcation segments, vessel area and length from the LAD and LCX bifurcations are less and greater, respectively, than LCA PV. Vessel length from the LAD and LCX SB (i.e. D1 & Ostium) are greater than upstream PV. No other parameters compared were statistically significant. Therefore, according to parametric testing vessel area and length have the most variability when comparing within and between LMCA bifurcations.

LAD/LCX (n =20)

	PV	DV	SB	Ostium
Area (mm^2)	17.7 ± 8.1	11.7 ± 5.6§	9.5 ± 4.6§	19.4 ± 9.3
Length (mm)	7.6 ± 4.0	19.3 ± 5.9§	18.4 ± 8.6§	2.8 ± 0.4
Eccentricity	0.2 ± 0.1	0.2 ± 0.1	0.2 ± 0.1	0.3 ± 0.1
Taper Factor	0.10 ± 0.06	0.06 ± 0.05	0.06 ± 0.05	0.12 ± 0.08

LAD/D1 (n = 21)

	PV	DV	SB	Ostium
Area (mm^2)	11.3 ± 6.7†	8.5 ± 5.4	3.5 ± 1.8†§*	14.0 ± 6.5†§*
Length (mm)	12.2 ± 4.4†	18.8 ± 6.0§	16.8 ± 5.3§	2.8 ± 0.4§
Eccentricity	0.2 ± 0.1	0.2 ± 0.05	0.2 ± 0.1	0.4 ± 0.1
Taper Factor	0.06 ± 0.05	0.05 ± 0.03	0.08 ± 0.03	0.07 ± 0.05

LCX/OM (n = 22)

	PV	DV	SB	Ostium
Area (mm^2)	12.2 ± 6.1†	7.2 ± 3.7†§	4.1 ± 2.1†§	13.1 ± 5.9†
Length (mm)	14.2 ± 7.4†	21.7 ± 7.4§	18.5 ± 7.6§	3.6 ± 1.1†
Eccentricity	0.2 ± 0.1	0.2 ± 0.1	0.2 ± 0.1	0.4 ± 0.1
Taper Factor	0.05 ± 0.04	0.05 ± 0.02	0.06 ± 0.06	0.06 ± 0.04

Table 3.1: Average geometric vessel properties expressed in mean ± standard deviation. Parametric testing outcomes distinguished by symbols. § = within bifurcation group significant difference ($P<0.05$), † = between bifurcation group significant difference ($P<0.05$) * = within bifurcation group significant difference from DV ($P<0.05$).

Taper factor values were similar for all bifurcation sites (Table 3.2). The values reported in Table 3.2 were used to graph the curves shown in Figure 3.7. The general shapes of the curves are the same for all bifurcations and individual segment. No statistical difference was observed between taper values. Despite no variability between taper factors from the observed data, general vessel taper has been quantified and can be incorporated into stent design.

LAD/LCX (n =20)

	PV	DV	SB	Ostium
Taper Factor	0.10 ± 0.06	0.06 ± 0.05	0.06 ± 0.05	0.12 ± 0.08
R_0 (mm)	2.3	1.9	1.7	2.4
A_0 (mm^2)	19.4	15.7	13.2	24.2
B/R_0	0.04	0.03	0.04	0.05

LAD/D1 (n = 21)

	PV	DV	SB	Ostium
Taper Factor	0.06 ± 0.05	0.05 ± 0.03	0.08 ± 0.03	0.07 ± 0.05
R_0(mm)	1.8	1.6	1.0	2.1
A_0 (mm^2)	11.3	15.7	13.2	24.2
B/R_0	0.03	0.03	0.08	0.03

LCX/OM (n = 22)

	PV	DV	SB	Ostium
Taper Factor	0.05 ± 0.04	0.05 ± 0.02	0.06 ± 0.06	0.06 ± 0.04
R_0 (mm)	1.9	1.5	1.2	2.0
A_0 (mm^2)	12.2	8.9	6.3	14.9
B/R_0	0.03	0.03	0.05	0.03

Table 3.2: Average taper values which were used to plot taper in Figure 3.7.

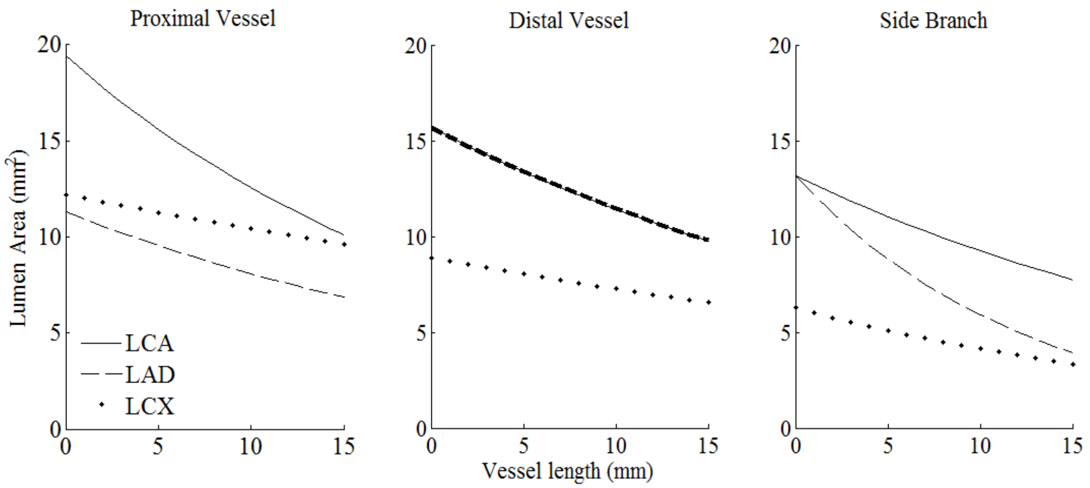

Figure 3.7 Plotting taper as function of taper factor ‘B’ based on Fung’s equation 2.4, from a length of 0 mm to 15 mm, moving proximal to distal along the vessel.

Figure 3.8 and Table 3.3 illustrate the bifurcation angles quantified for this analysis. The proximal and distal intersection angles (PIA and DIA, respectively) were calculated using the bifurcation vectors extracted using VMTK. The resulting values are shown in degrees; both groupings of bifurcation angles have high variance (13-24 degrees). The matched bifurcation angles were tested using a paired t-test; DIA from LAD/D1 was compared to DIA from LCX/OM and the PIA from LAD/D1 was compared to PIA from LCX/OM. Both pairings have similar results, which do not vary between bifurcation sites (considered to have the same means).

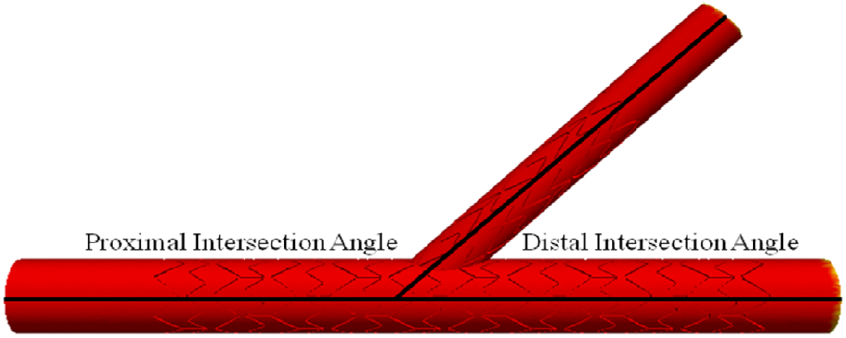

Figure 3.8: Bifurcation angle reference vessel, displaying the locations of proximal and distal intersection angles.

	LAD/LCX		LAD/D1		LCX/OM	
	DIA	**PIA**	**DIA**	**PIA**	**DIA**	**PIA**
Average B_A	75 ± 16	149 ± 24	62 ± 16	150 ± 17	65 ± 15	150 ± 13

Table 3.3: Average bifurcation angles (B_A), distal intersection angle (DIA) and proximal intersection angle (PIA) values shown as mean ± standard deviation.

Mean radius of curvature values were compared and averaged (Table 3.4). There was an increased value of curvature in the SB vessel segments, compared to the MV segments. However, with the larger mean radius of curvature values within the SB there are was also higher variance (standard deviation) so this difference did not reach significance. Mean radius of curvature increased for the LAD/D1 and LCX/OM bifurcations compared to the LCA, however there was no significant difference between bifurcations. Paired t-tests were performed on vessel curvature values to compare the differences between the analogous bifurcation segments. Three vessel groupings were compared: 1) MV and SB from the LCA bifurcation, 2) MV from LAD/D1 and MV from LCX/OM, and 3) SB from LAD/D1 and SB from LCX/OM. All three groupings were not significantly different from each other (means were considered the same).

Mean radius of curvature (mm^{-1})

	MV	**SB**
LAD/LCX	0.18 ± 0.04	0.20 ± 0.06
LAD/D1	0.22 ± 0.06	0.40 ± 0.20
LCX/OM	0.25 ± 0.10	0.34 ± 0.20

Table 3.4: Average mean radius of curvature calculations shown for both the main vessel (MV) and side branch (SB)

Geometric data from this investigation was applied to equations from branching law theory; k-values and Finet ratios, were quantified and are shown in Table 3.5. K-values varied from 2.5 to 3, similar to the principal of minimum work (k = 3) (Murray 1926). Calculated Finet ratios for each bifurcation site ranged from 0.7 – 0.8. As stated previously, Finet et al. (Finet et al. 2008) found a branching ratio based on bifurcations from the entire epicardial coronary tree of 0.678. Statistical analysis showed no differences between the bifurcation sites for the calculated k-values or Finet ratios. The values are not the same as those reported in previous studies however; this study does not include the entire coronary vasculature, but rather bifurcations isolated into three prominent bifurcations.

	LAD/LCX	LAD/D1	LCX/OM
k-value	3.1 ± 2.6	3.0 ± 5.1	2.5 ± 2.5
Finet ratio	0.7 ± 0.1	0.7 ± 0.1	0.8 ± 0.1

Table 3.5: Branching law indices quantified using average diameters values from each vessel for each bifurcation site.

Scatter plots from the raw data were created to illustrate how one geometric property can be influenced by another geometric property (Figure 3.9). For example, Figure 3.9 and Figure 3.10 compares average MV length to a corresponding bifurcation angle (DIA and PIA) with the use of scatter and JPDF plots, respectively. Average values were approximately 65˚ and 155˚, similar to the average calculated values from Table 3.1. The values from the JPDF yielded ranges of 50-80˚ for and 140-160˚, with lengths between 10-25 mm for both DIA and PIA bifurcation angles, respectively. The probability that all bifurcation sites would have these values was between 8-9%.

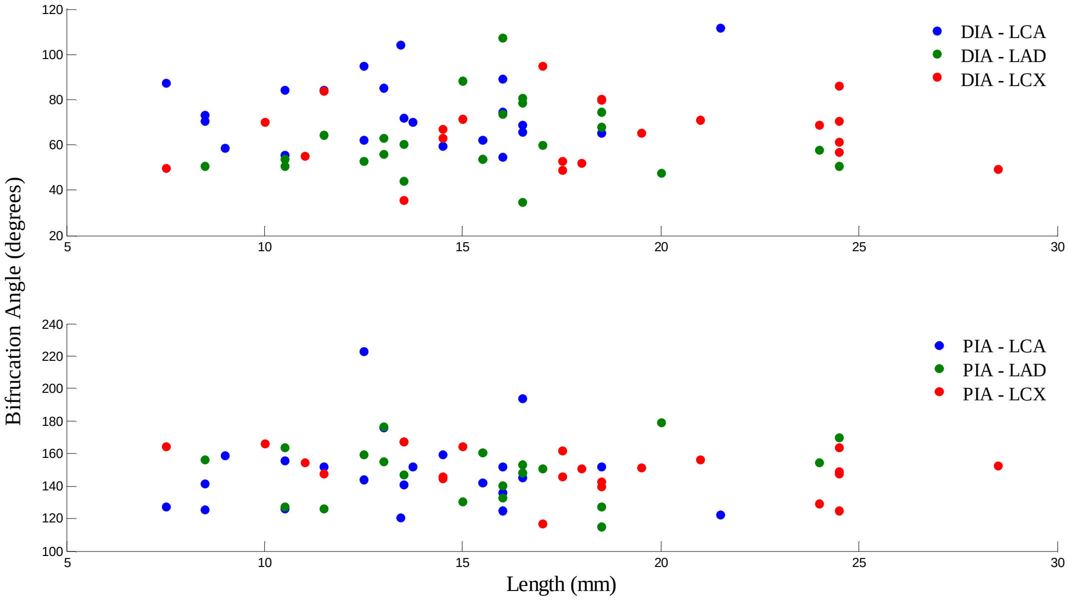

Figure 3.9: Scatter plots comparing bifurcation angles (DIA and PIA) for each bifurcation to mean main vessel length

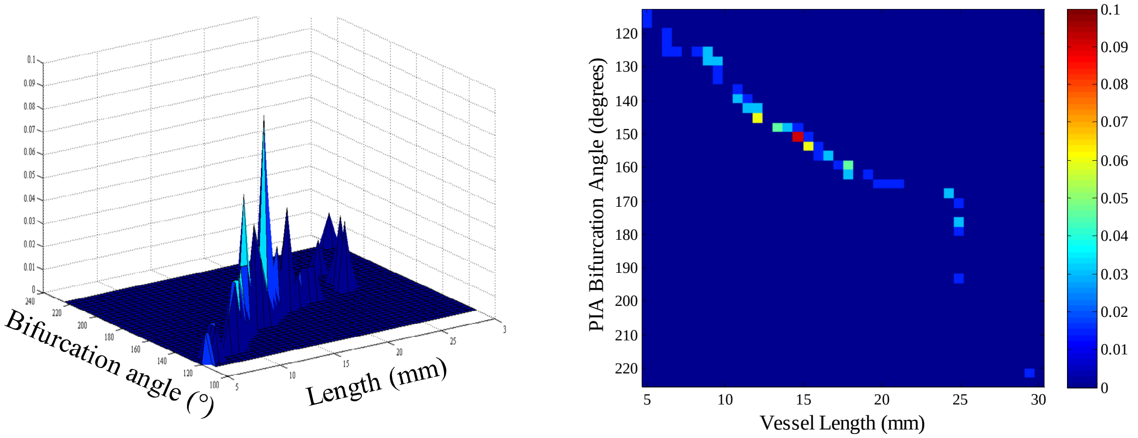

Figure 3.10: JPDF comparing the likelihood of a particular bifurcation angle occurring at a particular vessel length.

Figure 3.11 compares mean radius of curvature to vessel length. For all bifurcation sites the mean radius of curvature is approximately between 0.1 and 0.3 mm^{-1}, with corresponding lengths from 10-25 mm, respectively. Visually, the data from the LCX/OM vessel segments do not cluster in the same manner as the other two bifurcation sites. Therefore, JPDF plots were created to illustrate where the highest range of probabilities are located (intensity peaks in a 3D space). Results from the JPDF for each bifurcation site with values of 0.1-0.25 mm-1 for mean radius of curvature and lengths of 10-25 mm are the highest probability with 8-10%.

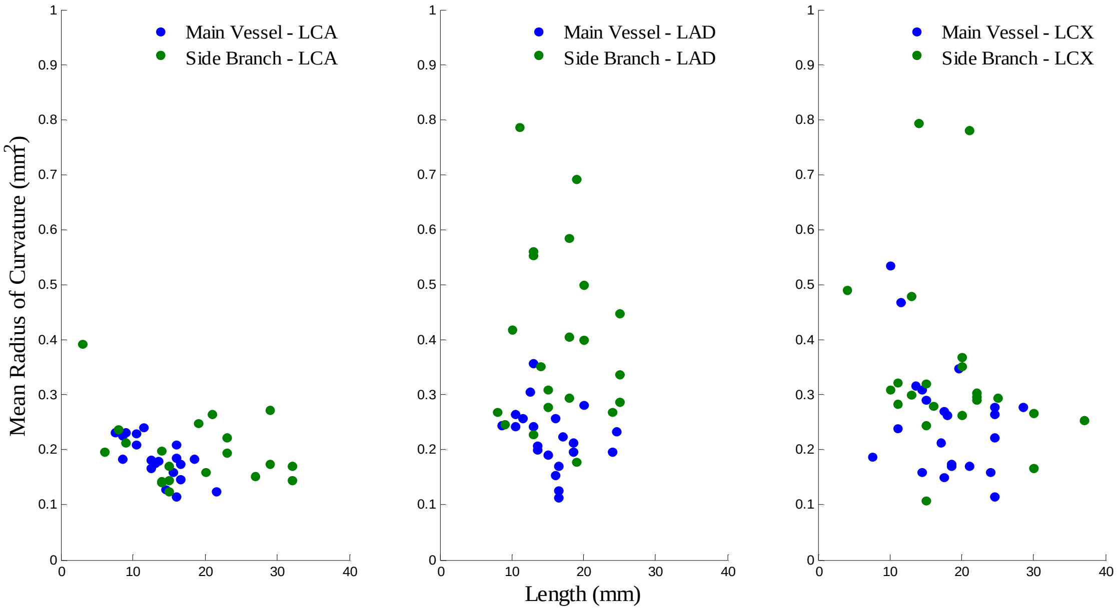

Figure 3.11: Scatter plots comparing vessel mean radius of curvature and vessel length for each branch and each bifurcation site.

Additional scatter and JPDF plots were created to compare 1) eccentricity and length, 2) area and length and 3) normalized area to length to vessel length. The scatter plots are shown in Figure 3.12 through Figure 3.14, respectively. Table 3.6, Table 3.7, and Table 3.8 compare the visual clustering results from the scatter plots to the intensities calculated from the JPDF plots. Vessel eccentricity and area are compared in Figure 3.12 and values are reported in Table 3.6. Clusters both between bifurcation groupings and within segment groupings are similar for all vessels. Interestingly, the ostial segments had the highest ranges of eccentricity values with the largest area values. The probabilities from the JPDF narrowed the ranges of component groupings.

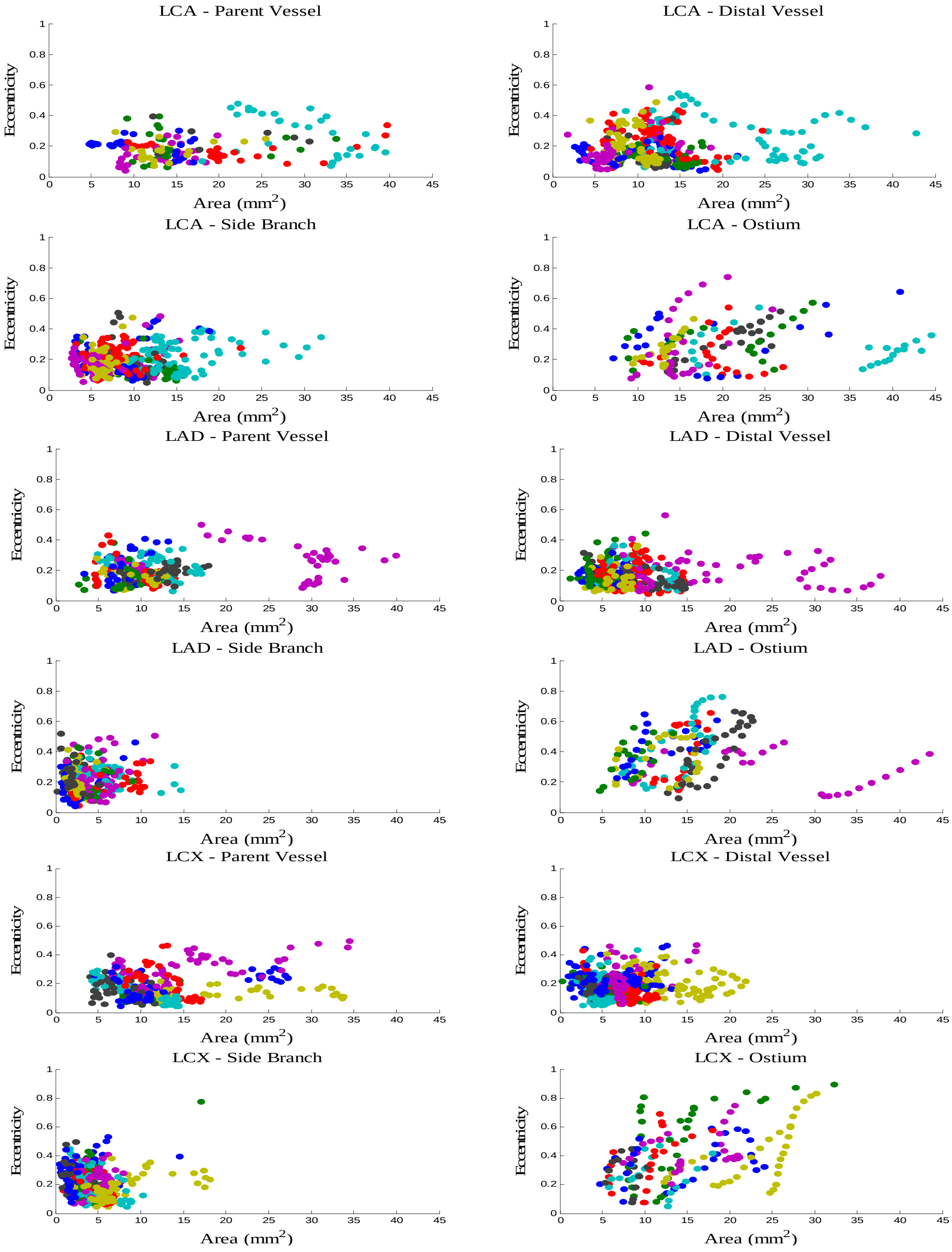

Figure 3.12: Scatter plots comparing eccentricity to vessel length for all vessel segments at all bifurcation sites, different colors represent each individual segment being compared.

LAD/LCX (n =20)

	Scatter plot trend		JPDF		
	Eccentricity	Area (mm^2)	Eccentricity	Area (mm^2)	Probability
PV	0.2	5-20	0.1-0.3	8-15	32%
DV	0.1-0.3	5-15	0.05-0.2	5-10	49%
SB	0.1-0.3	3-15	0.05 -0.2	5-10	28%
Ostium	0.3-0.4	10-25	0.2-0.4	10-20	22%

LAD/D1 (n = 21)

	Scatter plot trend		JPDF		
	Eccentricity	Area (mm^2)	Eccentricity	Area (mm^2)	Probability
PV	0.2	5-15	0.1-0.3	4-15	46%
DV	0.2-0.4	3-15	0.05-0.2	5-15	41%
SB	0.2-0.4	1-10	0.05-0.2	3-8	30%
Ostium	0.3-0.6	5-25	0.1-0.4	5-25	48%

LCX/OM (n = 22)

	Scatter plot trend		JPDF		
	Eccentricity	Area (mm^2)	Eccentricity	Area (mm^2)	Probability
PV	0.2-0.4	5-20	0.1-0.3	5-15	57%
DV	0.2-0.4	1-15	0.05-0.3	1-10	43%
SB	0.2-0.4	1-10	0.05-0.2	1-8	56%
Ostium	0.3-0.6	5-25	0.2-0.4	5-15	45%

Table 3.6: Clustered values of eccentricity and area for each bifurcation site obtained from scatter plots and from JPDF, showing the ranges and the associated probability with those ranges.

Vessel length and area is compared in Figure 3.13, scatter plot values compared against JPDF results are reported in Table 3.7. Length and vessel area data have similar trends both between bifurcation groupings and within segment groupings. Interestingly, the probabilities associated with each segment were highest across all segments for ostium segment for all three bifurcation sites (12%, 9%, and 8 %, for LCA, LAD/D1, and LCX/OM).

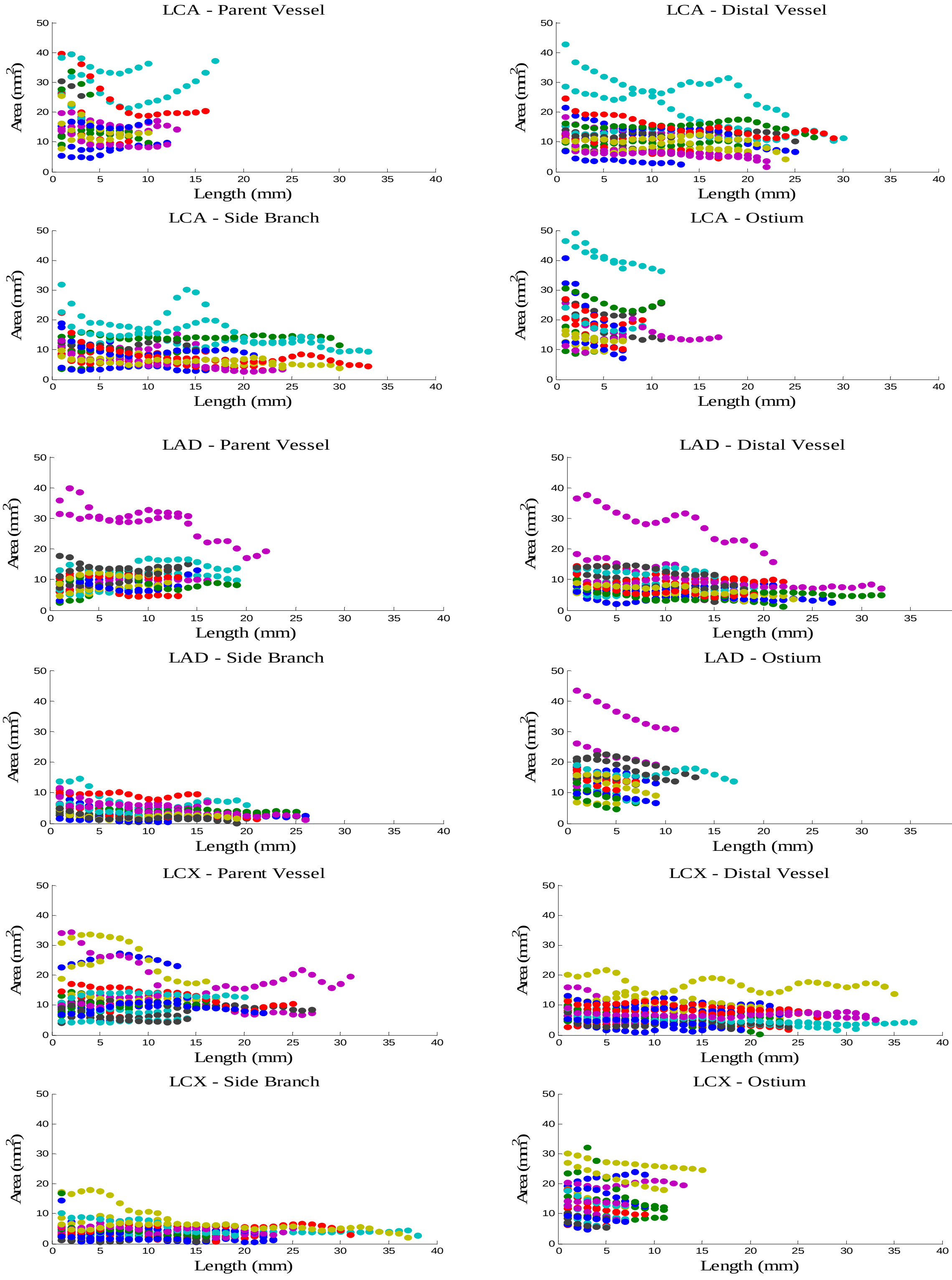

Figure 3.13: Scatter plots comparing vessel area to vessel length for all vessel segments at all bifurcation sites, different colors represent each individual segment being compared.

LAD/LCX (n =20)

	Scatter plot trend		JPDF		
	Length (mm)	Area (mm^2)	Length (mm)	Area (mm^2)	Probability
PV	1-15	5-20	2-7	0-20	53%
DV	15-20	5-15	5-18	5-25	44%
SB	15-30	3-15	3-18	5-10	34%
Ostium	1-10	10-25	1-5	5-15	50%

LAD/D1 (n = 21)

	Scatter plot trend		JPDF		
	Length (mm)	Area (mm^2)	Length (mm)	Area (mm^2)	Probability
PV	5-20	5-15	1-5	1-20	65%
DV	15-25	3-15	1-10	5-25	62%
SB	15-25	1-10	1-15	1-5	56%
Ostium	5-10	5-25	1-5	5-15	55%

LCX/OM (n = 22)

	Scatter plot trend		JPDF		
	Length (mm)	Area (mm^2)	Length (mm)	Area (mm^2)	Probability
PV	5-25	5-20	1-15	1-15	53%
DV	20-25	1-15	1-15	1-15	50%
SB	10-25	1-10	1-10	2-7	68%
Ostium	3-10	5-25	1-3	1-10	43%

Table 3.7: Clustered values of length and area for each bifurcation site obtained from scatter plots and from JPDF, showing the ranges and the associated probability with those ranges.

Scatter plots comparing vessel area against normalized area (area values were divided by total vessel segment length) data are shown in Figure 3.14. Values from the plots are reported in Table 3.8. Length and normalized area data have similar trends for each of the segments compared; LAD/D1 and LCX/OM values are similar from both the scatter plots as well as the JPDF. The LCA bifurcation had slightly different values than the two daughter bifurcations, with overall higher probabilities of cluttering to occur (10% probability observed in both DV and ostium of LCA).

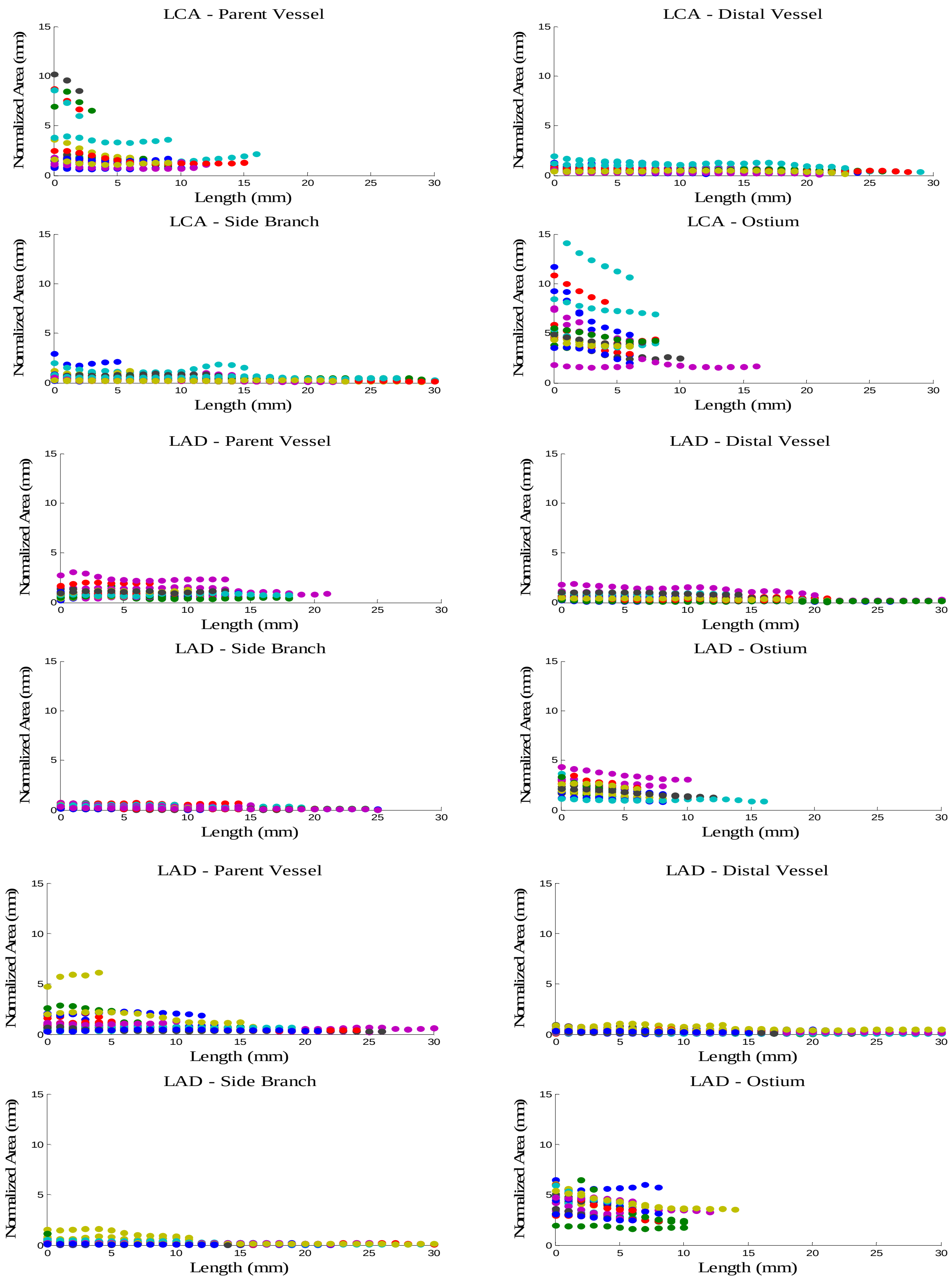

LCA - Parent Vessel

LCA - Distal Vessel

LCA - Side Branch

LCA - Ostium

LAD - Parent Vessel

LAD - Distal Vessel

LAD - Side Branch

LAD - Ostium

LAD - Parent Vessel

LAD - Distal Vessel

LAD - Side Branch

LAD - Ostium

Figure 3.14: Scatter plots comparing normalized area to vessel length against vessel length for all vessel segments at all bifurcation sites, different colors represent each individual segment being compared.

LAD/LCX (n =20)

	Scatter plot trend		JPDF		
	Length (mm)	Normalized Area (mm)	Length (mm)	Normalized Area (mm)	Probability
MV ROC	5-15	1-5 & 6-10	1-8	0-5	65%
DV	5-20	1-3	5-15	0-3	55%
SB	5-25	0-3	1-10	0-2.5	64%
Ostium	0-8	3-15	0-2	0-8	56%

LAD/D1 (n = 21)

	Scatter plot trend		JPDF		
	Length (mm)	Normalized Area (mm)	Length (mm)	Normalized Area (mm)	Probability
PV	5-10	0-3.5	1-6	0-2.5	65%
DV	1-15	0-2	2-10	0-3	63%
SB	1-15	0-1	2-8	0-3	55%
Ostium	1-8	1-5	1-5	0-3	75%

LCX/OM (n = 22)

	Scatter plot trend		JPDF		
	Length (mm)	Normalized Area (mm)	Length (mm)	Normalized Area (mm)	Probability
PV	1-15	0-3	1-5	0-5	60%
DV	5-10	0-1	1-10	0-3.5	65%
SB	1-15	0-2	1-5	0-2	54%
Ostium	1-8	3-6	2-4	0.5-4	65%

Table 3.8: Clustered values of length and normalized area to length for each bifurcation site obtained from scatter plots and from JPDF, showing the ranges and the associated probability with those ranges.

Vessel length and area were the characteristics which impacted the statistical analysis the most. To more fully describe these indices, individual slice area was divided by length total vessel length for each vessel segment, yielding normalized area. Normalized area and length are reported to provide insight about general vessel behavior. Quantifying how vessel area is related to length provides information about where common lengths and areas will be observed. Information elucidated from the scatter plots describes broader ranges than those from the JPDF results. The probability of the cluster (spike) in the data was relatively low (< 15%) for all geometric properties compared; however, the data usually exhibited one prominent spike from the data within the plot, indicating data clustering. Scatter and JPDF plots provide information about how two geometric properties are influenced by the other. Additional information is required to classify the morphometric characteristics of the coronary arteries. In order to compare more than two variables data clustering and principal component analysis was performed.

The scatter plots and JPDF plots show that there may be some skewing within the data, which would not be accounted for using the parametric statistical analysis. To ensure the data was not influenced by the requirement of an underlying distribution, Kuskal-Wallis analysis of variance test and Wilcoxon signed-rank tests were performed. Table 3.9 and Table 3.10 report statistical significance observed from non-parametric testing.

LAD/LCX (n =20)

	PV	DV	SB	Ostium
Area (mm^2)	17.7 ± 8.1	11.7 ± 5.6§	9.5 ± 4.6§*	19.4 ± 9.3*
Length (mm)	7.6 ± 4.0	19.3 ± 5.9‡§	18.4 ± 8.6‡§	2.8 ± 0.4

LAD/D1 (n = 21)

	PV	DV	SB	Ostium
Area (mm^2)	11.3 ± 6.7†	8.5 ± 5.4†	3.5 ± 1.8†§*	14.0 ± 6.5†§*
Length (mm)	12.2 ± 4.4†	18.8 ± 6.0§	16.8 ± 5.3‡§	2.8 ± 0.4

LCX/OM (n = 22)

	PV	DV	SB	Ostium
Area (mm^2)	12.2 ± 6.1†	7.2 ± 3.7†§	4.1 ± 2.1†§	13.1 ± 5.9†
Length (mm)	14.2 ± 7.4‡†	21.7 ± 7.4‡§	18.5 ± 7.6‡§	3.6 ± 1.1†

Table 3.9: Average geometric vessel properties expressed in mean ± standard deviation. Nonparametric testing outcomes distinguished by symbols. § = within bifurcation group significant difference ($P<0.05$), † = between bifurcation group significant difference ($P<0.05$) * = within bifurcation group significant difference from DV ($P<0.05$), ‡ within bifurcation group significant difference from OS ($P<0.05$).

	LAD/LCX (n =20)		LAD/D1(n = 21)		LCX/OM (n =22)	
	DIA	**PIA**	**DIA**	**PIA**	**DIA**	**PIA**
Average B_A (degrees)	76 ± 16	149 ± 24	62 ± 16§	150 ± 17	65 ± 15	150 ± 13
Radius of curvature (mm^{-1})	**MV**	**SB**	**MV**	**SB**	**MV**	**SB**
	0.18 ± 0.04	0.20 ± 0.06	0.22 ± 0.6	0.40 ± 0.20§	0.25 ± 0.10§	0.34 ± 0.20§

Table 3.10: Average geometric vessel properties expressed in mean ± standard deviation. Nonparametric testing outcomes distinguished by symbols. § = between bifurcation group significant difference (P<0.05)

Results from Kuskal-Wallis analysis of variance were similar to results from the parametric ANOVA. There were some indices that were considered significantly different which were not included previously. Vessel area was significantly different within vessel parameters, especially the ostium, as compared to the ANOVA where the ostial region only different from the PV and not individual segments. The LAD DIA bifurcation angle was statistically different from the LCA parent bifurcation. Also, radius of curvature was significantly different between the MV of the LCA and LCX as well as the SB. Overall, vessel area still is the most variant geometric property, but other features such as bifurcation angle and curvature should be included in design parameters to design stents for specific regions of the coronary vasculature. The utility of non-parametric statistical analysis was required in this analysis because there were statistical differences which were not discovered using the normal parametric tests. This could be a result of the chi-square test having too much type 2 statistical (beta) error. The only way to make sure that type 2 error was not introduced into the quantification is by increasing the number of samples or compromising on the level of significance (decreasing significance to < 95%). Discussed later, sample size determination will be quantified to see if enough samples were collected to accurately distinguish statistical significance. If too few samples were used, that could be an indication that statistical assumptions may not hold true for all instance within the data. Therefore, it was worthwhile to perform nonparametric testing to elucidate if statistical error was introduced and reveal the true distribution of the data. Despite performing several statistical tests, which describe the data based on means and distribution, deciphering where most of the data clusters is important when providing results for stent design.

Data clustering was accomplished by custom Matlab scripts which employed inherent clustering analysis tools from the statistical toolbox. Statistical and partitioning methods were used to group morphometric parameters by similarity. This approach allows for a large number of input characteristics (i.e. vessel area, length, eccentricity, taper, radius of curvature and bifurcation angles). The function calculated the pairwise distances between parameters, where then function linkage created hierarchical cluster trees. The data was clustered based on operator-specified threshold which set the maximum number of clusters. Hierarchical clustering is a way to explore groupings within the vessel data, concurrently over an array of scales of distance, by creating a cluster tree. The tree is not a single set of clusters, as in k-means, but rather a multi-level hierarchy, where clusters at one level are joined as clusters at the next higher level.

The data was also clustered based on statistical k-mean values. The k-means values which are calculated by reassigning points among clusters to decrease the sum of point-to-centroid distances, and then re-computes cluster centroids for the new cluster assignments. K-means clustering is a partitioning method, each observation in the data set is associated with a locations and distances from each other. It partitions the objects into K mutually exclusive clusters, such that objects within each cluster are as close to each other as possible, and as far from objects in other clusters as possible. Each cluster is characterized by its centroid, or center point. The distances used in clustering do not represent spatial distances. All vessel data was used for the quantification.

All three bifurcations were clustered as well as all vessel segments (PV, MV, SB and Ostium) and the primary seven geometric properties (area, length, taper, eccentricity, radius of curvature and bifurcation angles both DIA and PIA). The clustering approaches by both, hierarchical and k-means elucidate some understanding how the data is grouped based on geometric properties. While both clustering techniques provide information about how the data was grouped, k-means was selected as the primary partitioning modality for this investigation.

K-means completely partitions the data into separate groups, whereas with hierarchical clustering there is some overlap between groupings. K-means clustering for bifurcation sites and vessel segments are reported in Table 3.11 and Table 3.12. The data is clustered into groups and values from each group are reported as average values and standard deviations which are included within each group.

By calculating the principal components from these analyses; the cumulative sum of the variances (for example within the LCA bifurcation are: 50, 81, 93, 99, 99.9993, 99.9997, and 100.0000 as displayed in Figure 3.15. This cumulative sum of variances indicates that approximately 80% of the variance is accounted for by the first two principal components (vessel area and vessel length). Overall, the clustering analysis shows that vessel area and length are the two most influential geometric properties when investigating vessel morphology.

K-means Clustering Values for Vessel Segments

PV Cluster	Area (mm2)	Length (mm)	EI	Taper Factor	ROC (mm^{-1})
26	9.5 ± 3.3	16.3 ± 6	0.2 ± 0.06	0.1 ± 0.06	0.2 ± 0.08
11	23.9 ± 7.2	7.3 ± 3.5	0.2 ± 0.05	0.1 ± 0.06	0.2 ± 0.05
26	13.7 ± 6.3	11.0 ± 3.9	0.2 ± 0.07	0.1 ± 0.04	0.2 ± 0.07
DV Cluster	**Area (mm2)**	**Length (mm)**	**EI**	**Taper Factor**	**ROC (mm^{-1})**
23	5.3 ± 1.7	24.1 ± 6	0.2 ± 0.03	0.1 ± 0.03	0.3 ± 0.08
12	15.0 ± 7.2	16.0 ± 5.4	0.2 ± 0.05	0.0 ± 0.04	0.2 ± 0.11
28	9.6 ± 3.1	21.0 ± 5.7	0.2 ± 0.06	0.1 ± 0.03	0.2 ± 0.04
SB Cluster	**Area (mm2)**	**Length (mm)**	**EI**	**Taper Factor**	**ROC (mm^{-1})**
15	3.5 ± 8.6	7.6 ± 18.3	0.1 ± 0.2	0.04 ± 0.06	0.1 ± 0.25
40	1.7 ± 3.6	7.3 ± 20.2	0.1 ± 0.21	0.0 ± 0.07	0.2 ± 0.36
8	5.7 ± 11.4	4.8 ± 11.1	0.1 ± 0.23	0.1 ± 0.05	0.1 ± 0.22
Ostium Cluster	**Area (mm2)**	**Length (mm)**	**EI**	**Taper Factor**	
21	12.4 ± 4.2	2.4 ± 1.7	0.4 ± 0.09	0.1 ± 0.05	
31	18.7 ± 9.1	2.0 ± 1.7	0.3 ± 0.11	0.1 ± 0.07	
11	11.9 ± 4.7	4.0 ± 3.6	0.4 ± 0.07	0.07 ± 0.06	

Table 3.11: K-means clustering values for each of the vessel characteristics quantified. Values expressed as average value ± standard deviation. The number of samples clustered into each group is reported under each cluster. The data was clustered into three groupings based on the expected number of bifurcation sites.

K – Means Clustering Values (Bifurcation Sites)

LCA Cluster	**Area (mm^2)**	**Length (mm)**	**EI**	**DIA (degrees)**	**PIA (degrees)**	**Taper Factor**	**ROC (mm^{-1})**
21	23.4 ± 8.7	6.8 ± 4.3	0.3 ± 0.1	67 ± 12	162 ± 24	0.11 ± 0.07	0.17 ± 0.03
21	11.9 ± 5.4	22.8 ± 6.5	0.2 ± 0.1	65 ± 11	164 ± 25	0.06 ± 0.04	0.19 ± 0.04
22	9.9 ± 4	12 ± 7.8	0.2 ± 0.1	76 ± 6	143 ± 14	0.06 ± 0.05	0.20 ± 0.05
16	12.8 ± 6	13.8 ± 9.8	0.2 ± 0.1	93 ± 11	125 ± 2	0.11 ± 0.07	0.20 ± 0.04
LAD Cluster	**Area (mm^2)**	**Length (mm)**	**EI**	**DIA (degrees)**	**PIA (degrees)**	**Taper Factor**	**ROC (mm^{-1})**
19	10.8 ± 10.2	19.6 ± 7.8	0.2 ± 0.1	46 ± 7	165 ± 11	0.06 ± 0.05	0.27 ± 0.12
33	8.2 ± 4.6	10.5 ± 4.6	0.3 ± 0.1	56 ± 4	154 ± 13	0.06 ± 0.04	0.30 ± 0.13
8	10.1 ± 5.1	14.9 ± 5.2	0.2 ± 0.1	98 ± 10	132 ± 1	0.07 ± 0.06	0.21 ± 0.08
24	10.2 ± 5.9	14.3 ± 6.1	0.2 ± 0.1	73 ± 6	135 ± 14	0.07 ± 0.04	0.25 ± 0.11
LCX Cluster	**Area (mm^2)**	**Length (mm)**	**EI**	**DIA (degrees)**	**PIA (degrees)**	**Taper Factor**	**ROC (mm^{-1})**
12	5.8 ± 2.8	28.8 ± 5.6	0.2 ± 0	69 ± 5	146 ± 11	0.04 ± 0.04	0.23 ± 0.08
16	8.3 ± 4.9	13.6 ± 8.5	0.2 ± 0.1	82 ± 4	138 ± 9	0.08 ± 0.05	0.30 ± 0.17
28	9.1 ± 5.2	8.2 ± 4.9	0.3 ± 0.1	65 ± 6	154 ± 8	0.05 ± 0.03	0.31 ± 0.15
28	10.1 ± 6.9	16.8 ± 8.4	0.2 ± 0.1	50 ± 7	158 ± 8	0.05 ± 0.03	0.26 ± 0.08

Table 3.12: K-means clustering values for each of the vessel characteristics quantified. Values expressed as average values ± standard deviation. The number of samples clustered into each group is reported under each cluster. The data was clustered into four groupings based on the expected number of individual vessel segments.

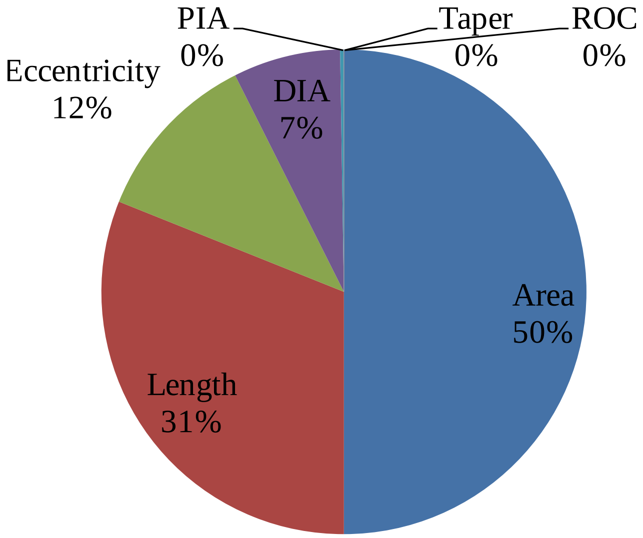

Figure 3.15: Principal component analysis outcome for the LCA bifurcation, illustrating the geometric properties which introduce the most variance when comparing all properties.

3.4 Sample Size Determination

In design applications it is important to establish how many samples (n) are required to properly elucidate the desired information. Sample size determination can be accomplished by using statistical principals. For accurate sample size determination, three inputs are required to produce a confidence interval estimate for an unknown population mean. Those three indices are: the desired confidence level, the standard deviation of the characteristic under study (σ), and the margin of error (E). These variables can be applied to the following equation 3.3:

$$n = \left(\frac{Z_{1-\left(\frac{\alpha}{2}\right)}\sigma}{E}\right)^{2} \qquad \text{Equation 3.3}$$

The desired confidence level is 95% which is equal to 1.96. Standard deviations from each vessel segment for both circumferential diameters and vessel segment lengths were applied to equation 3.1; those values are displayed in Table 3.13.

	LCA	LAD	LCX
PV	1.04	0.97	0.90
DV	0.86	0.86	0.74
SB	0.81	0.50	0.95
OS	1.09	0.88	0.90

	LCA	LAD	LCX
PV	4.05	4.39	7.42
DV	5.88	5.98	7.39
SB	8.59	5.30	7.61
OS	0.41	0.44	1.14

Table 3.13: Standard deviations from vessel diameters (left) and vessel length values (right) for each vessel segment at every bifurcation location.

Two common indices reported for stent sizing options are diameter and length measurements. Therefore, margins of error were defined as values which encompassed reported sizing values. Common diameter and length size options were taken from clinically relevant coronary stents: the Taxus™ Express^2 and the Cypher™ coronary stent.

Taxus™ Express2	Cypher™
Lengths (mm): 8, 12, 16, 20, 24, 28, 32	Lengths (mm): 8, 13, 18, 23, 28, 33
Diameters (mm): 2.5, 2.75, 3, 3.5	Diameters (mm): 2.25, 2.5, 2.75, 3, 3.5

From the values reported by both clinically relevant stents, the common change in length was approximately 5 mm. Therefore E_{length} = 5 mm for sample size determination. General changes in diameter sizing options was 0.25, therefore $E_{Diameter}$ = 0.25. Sample size determination for each vessel segment was calculated. Sample size requirements are presented for every bifurcation site, vessel diameter and length in Table 3.14.

	LCA	LAD	LCX
PV	67	58	51
DV	47	46	36
SB	41	16	57
OS	74	49	51

	LCA	LAD	LCX
PV	3	3	9
DV	6	6	9
SB	12	5	9
OS	1	1	1

Table 3.14: Samples required (N) to obtain enough samples to accurately conduct statistical analysis related to vessel diameters (left) and lengths (right) for each vessel segment at every bifurcation locations.

The current study modeled 22 patient data sets for each bifurcation site. After calculating sample sizes for both vessel diameter and vessel length, (Table 3.14), approximately 75 total data sets are required to accurately represent coronary diameters. Interestingly, vessel length, a source of variance (~30%) for all vessel groupings per the principal component analysis has fulfilled the minimum number of samples required for accurate statistical results. Therefore, statistical differences quantified from length measurements are correct. Vessel length is an important attribute regarding stent design.

3.5 Summary

A method for producing computational representations and quantifying morphometric data has been established that is relatively fast and accurate. Geometric properties (vessel area, length, taper, eccentricity, bifurcation angles and radius of curvature) were defined using 3D imaging data. Statistical methods provided insight on trends observed across three LCMA bifurcation sites, vessel area and length were significantly different after performing parametric procedures. Data skewing may have been introduced due to patient variability.

Nonparametric statistical analysis was performed to ensure data distributions did not affect the outcome of the analysis. Vessel area and length within and between bifurcation sites were the most significantly different. Notably, nonparametric testing exposed both bifurcation angles and mean radius of curvature values as significantly different. Further post-processing was accomplished using scatter plots, JPDF plots, clustering analysis and principal component analysis. The additional post-processing techniques were used to more fully understand where trends exist within coronary bifurcation morphology.

Sample sizes for diameter and length measurements were calculated. The results revealed that involving more patients is necessary to obtain a sample size large enough to accurately report diameter (area) measurements. Additional patient data would provide more data and meet the minimum sample size requirement without doing excess work.

CHAPTER 4 : DISCUSSION

4.1 Review of thesis objectives

The goal of this thesis was to develop a method whereby the adverse hemodynamic changes induced by PSB intervention strategies can be quantified. Specifically, CFD simulations were performed investigating the adverse hemodynamic effects of multiple-stent intervention strategies with additional provisional techniques in the LAD/D1 coronary bifurcations and the local affects on TAWSS and OSI values. Initially, the simplest problem reflective of geometric changes observed from IVUS and micro-CT data was implemented using idealized vascular representations. The continuation of tools developed was employed to include more complex stenting strategies. Added complexity within the computational models paired with CFD analysis, reveals how hemodynamic indices affect *in vivo* stent performance.

The second portion of this thesis was aimed at developing a workflow which can rapidly construct and quantify image-based CT data. This workflow was created to allow for more insight into coronary morphology and design better stents. Further quantification was accomplished using several strategies to more accurately capture normal geometric clustering via post-processing techniques using statistical and signal processing methods.

4.2 Novel aspects of the current work

This work confirms what was known about blood flow through stents using CFD models and expands on previous work (Williams et al. 2010) by applying CFD techniques to the coronary artery bifurcation with several important improvements. The current simulations employ a 3-element Windkessel (i.e. RCR) outflow boundary conditions strategy to include the impact of the distal vasculature not included in the physical CFD model. This method is not ideal since it does not include the time-varying resistance induced by myocardial contraction and will be improved upon in subsequent simulations beyond the scope of this thesis. Nonetheless, these boundary conditions provide reasonable results and are more reflective of the true physiologic phenomena than employing a zero pressure outlet boundary conditions as is frequently performed. The outlet boundary conditions used allow for quantification of FFR. Idealized stenotic vessel simulations demonstrate that CFD employed with the current boundary conditions offers a non-invasive method for quantifying severity of stenosis via FFR. The idealized vessel with 50% reduction in diameter was confirmed not clinically significant (< 0.75) while the 70% reduction in diameter was clinically significant. These FFR results from CFD simulations correlate with clinical findings.

The realistic nature of the CFD models created for the current work is a drastic improvement over the models that had been employed previously (Deplano, Bertolotti, and Barragan 2004). Although the models in the first portion of the thesis are idealized, the vascular dimensions and bifurcation angle were implemented based on statistical characteristics from a sampling of clinical patients (Finet et al. 2008; Vignon-Clemental et al. 2006).

Additionally, the geometric changes induced by bifurcation stenting are rooted in clinical observations made from IVUS clinical data of the carina shift before stenting, after stenting and following gentle to aggressive balloon angioplasty kissing dilation and second stenting procedure. Previous studies in this area frequently use less common and far simpler stent designs, whereas the Taxus Express^2 stent is currently used frequently within cardiac catheterization laboratories around the world making the current results more interesting and applicable to clinicians. A unique contribution of this work is the workflow developed to quickly extract image data models, obtain geometrical data, and construct computational models. This workflow can be used by future researchers to allow for quicker simulation time. The post-processing uses a variety of techniques which can allow for multidimensional insight on differences and similarities observed by this area of the vasculature. Finally, the morphologic characteristics delineated from this workflow were processes using common parametric and lesser implemented parametric techniques to determine which properties may be most important in the stent design process. Of note, these results also take into consideration the full 3D nature of the vasculature relative to prior angiographic or casting studies in this area

4.3 Hemodynamic results

Stenting alters hemodynamics near the coronary bifurcation by altering arterial geometry. This geometric alteration is due to stent design as well as changes in the vessel caused by the implantation procedure. For all idealized vessels, WSS was decreased distal to the bifurcation and localized within strut sections. This further understanding highlights potential means by which next-generation bifurcation stents can be improved to limit the potential for restenosis. For example, potentially favorable spatial changes in flow patterns could be introduced by optimizing the design (i.e. pattern) of stent linkages or the bifurcation branching morphology. However overexpansion of the distal main branch will almost always lead to low WSS and higher OSI, regardless of the stent design. Although the PSB techniques investigated are all different and more complicated than those previously reported, the differences in total low TAWSS are within 3%. This small difference may or may not have an impact on the outcome of the PSB stenting technique performed.

The hemodynamic changes caused by stents can be clearly seen in the axial and circumferential plots shown in Figure 2.17, Figure 2.18 and Figure 2.19. MV stenting with aggressive KV showed increased WSS distal to the bifurcation as compared with the proximal region. All the stented models show decreased WSS distal to the stenosis as compared to their respective proximal regions. The WSS pattern shown in the circumferential plots shows a combination of the skewing pattern found also in the pre-stent models and lower WSS as compared to the pre-stent model. In addition there is a stent pattern of alternating high and moderately high peaks. Stenting induces areas of low WSS according to the pattern of the stent that is implanted with intermittent areas being exposed to higher shear stress near the center of each intra-strut region. The present results show the same behavior for the more complex Taxus Express^2 stent. Many assumptions were used for idealized model CFD simulations, but these results will are helpful in understanding how fluid is imparted on different geometries with PSB stenting techniques.

4.4 Relationship to previous work

LaDisa et al. simulated blood flow through straight and curved stented vessels and compared different stent design parameters including the number, width, thickness, orientation and deployment ratio of an implanted stent (LaDisa et al. 2005). Deplano et al. conducted similar simulations in an idealized bifurcation and also compared stent design parameters of a Palmaz slotted tube stent (Deplano et al. 2004). Deplano et al. used a bifurcation model with a bifurcation angle of 90 degrees which is within the physiologic range but not common. Further their branching diameters do not conform to physiologic branching patterns described recently by Finet et al. (Finet et al. 2008). Additional, the boundary conditions implemented for this previous stented bifurcation model used methods which may not produce physiologic pressures and are therefore incapable of calculating FFR.

This work represents the next step in CFD modeling of the coronary artery bifurcation. The models employed here are more physiologic in that they conform to branching patterns described by Finet et al. and a physiologic bifurcation angle described by Pflederer et al.(Finet et al. 2008; Pflederer et al. 2006). Expanding on the methods and findings by Williams et al. the addition of complexity in stent configuration in conjunction with CFD analysis was accomplished. Williams et al. found some unique characteristics applicable to further stent design research. Their findings demonstrate that CFD can be used to quantify altered hemodynamics due to MV stenting and subsequent SB angioplasty in a coronary bifurcation and shows representative changes in local vascular geometry. The current study used the same local quantification methods as Williams et al. who quantified the amount of flow alterations due to overall vessel geometry versus the intricacies of stents struts, as well as circumferential and axial alterations in WSS indices and revealed that there may not be a benefit to SB intervention from a fluid dynamics perspective.

The development of an image-based quantification technique will better equip both researchers and clinician in rapidly understanding and identifying morphometric alterations as shown by the tortuousness and wide-variety of geometric ranges observed throughout the coronary vasculature. This work goes beyond casting studies which employ two-dimensional quantification of geometric indices as well as sacrificed vasculature. Also, this goes beyond basic angiography quantification tool which impose a third dimension based upon mathematical calculations, which do not account for vessel overlap and changes over the cardiac cycle. By utilizing all three dimensions accurately, higher quality computational representations are available for future CFD studies.

4.5 Limitations

Limitations to this analysis include the assumptions of rigid walls, a Newtonian fluid, and a Womersley profile at the inlet. The assumption of RCR Windkessel outlet boundary conditions is not completely representative of physiology. The 3-element Windkessel model assumes that frequency analysis can be performed on pressure and flow waveforms to calculate outlet impedance and then the values for resistances and capacitance. A more complex model of the outlets might include a time-varying resistor or ventricular coupling. Another limitation was the use of a flow waveform that was measured in a canine model. A canine waveform was originally used due to lack of availability of a human waveform (LaDisa et al. 2002) and proper instrumentation. Previous studies used the physiological waveforms from this investigation which allows comparable results against reported findings (Williams et al. 2010).

Physiologically the vessel models have certain anatomical aspects omitted from the design process. All vessel models were idealized with straight cylindrical cross-sections, all of which exhibit no change in curvature from proximal to distal locations. The models did not include deformable walls; due to the pulsatile nature of the heart the coronary arteries also undergo a cyclic longitudinal strain (change in length) over the cardiac cycle. The constant change in vessel length during contraction could affect the both stent placement as well as MV/SB stent interactions. Further investigations involving deformable walls and the introduction of vessel strain would be beneficial to understanding the factors of fatigue which affect product design.

The primary workflow created to quantify coronary morphology does not present any limitations, however some limitations are associated with the current study. The image data provided in this study was not cardiac gated, providing only one point during the cardiac cycle. As stated above, the coronary arteries move due to the pulsatility of the heart, this movement has the ability to change vessel characteristics. Particularly, radius of curvature and eccentricity are attributes which have high probabilities of changing during this event. While the results presented in this study on coronary vessel morphology are correct they only describe one point in the cardiac cycle. Performing the quantification methods described in this thesis on cardiac-gated image data could improve understanding of prominent coronary bifurcations.

One further limitation is that patient demographic data including age, gender, body surface area and coronary artery dominance were not included. Unfortunately this information was unavailable for inclusion for this investigation. If available, this data would allow for additional statistical analysis of subgroups, as well as provide accurate sample size for statistical analysis on diameter measurements.

CHAPTER 5 : CONCLUSION

The bifurcation lesion is one of the most challenging lesion subsets in the field of percutaneous coronary intervention (Colombo et al. 2004; Ikeno et al. 2006; Lefèvre et al. 2005). As alterations in indices of WSS are reported to be associated with the progression of atherosclerosis (Louvard, Lefèvre, and Morice 2004), it is important to understand local, potentially adverse, changes in these hemodynamic indices as a result of interventions in order to develop better strategies and devices. This thesis is a tool to elucidate some of the unanswered questions surrounding the benefit of using multiple stenting techniques or a dedicated bifurcated stent. Concurrently, a rapid and robust methodology was developed to quantify 3D vessel characteristics to reveal more about patient-specific geometries. Additionally, the use of 64 MDCT data provided a noninvasive means to model coronary morphology. From the four idealized stented models; the low, oscillatory, flow observed during rest, which is associated with increased rates of restenosis (Hoffmann et al. 1996), was mostly eliminated during exercise conditions. The multiple PSB stenting techniques showed the protrusion of the SB into the MV disrupts fluid flow and creates unnatural velocity profiles around the struts. Areas of WSS were changed with the introduction of vessel dilation (kissing). Further application of these observances and quantification will provide insight into next-generation stent design.

BIBLIOGRAPHY

AHA. (american heart association) heart and stroke statistics. 2007 update.

Antiga, L. and D. A. Steinman. 2004. Robust and objective decomposition and mapping of bifurcating vessels. *IEEE Trans Med Imaging* 23, no. 6: 704-13.

Bovendeerd, PH, P Borsje, T Arts, and FN van De Vosse. 2006. Dependence of intramyocardial pressure and coronary flow on ventricular loading and contractility: A model study. *Ann Biomed Eng* 34, no. 12: 1833-45.

Choi, G., C. P. Cheng, N. M. Wilson, and C. A. Taylor. 2009. Methods for quantifying three-dimensional deformation of arteries due to pulsatile and nonpulsatile forces: Implications for the design of stents and stent grafts. *Ann Biomed Eng* 37, no. 1: 14-33.

Colombo, A, J Drzewiecki, A Banning, E Grube, K Hauptmann, S Silber, D Dudek, S Fort, F Schiele, K Zmudka, G Guagliumi, ME Russell, and TAXUS II Study Group. 2003. Randomized study to assess the effectiveness of slow- and moderate-release polymer-based paclitaxel-eluting stents for coronary artery lesions. *Circulation* 108, no. 7: 788-94.

Colombo, A, JW Moses, MC Morice, J Ludwig, DR Jr Holmes, V Spanos, Y Louvard, B Desmedt, C Di Mario, and MB Leon. 2004. Randomized study to evaluate sirolimus-eluting stents implanted at coronary bifurcation lesions. *Circulation* 109, no. 10: 1244-9.

Dangas, G and F Kuepper. 2002. Cardiology patient page. Restenosis: Repeat narrowing of a coronary artery: Prevention and treatment. *Circulation* 105, no. 22: 2586-7.

Deplano, V, C Bertolotti, and P Barragan. 2004. Three-dimensional numerical simulations of physiological flows in a stented coronary bifurcation. *Med Biol Eng Comput* 42, no. 5: 650-9.

Figueroa, C.A., I.E Vignon-Clementel, K. Jansen, T.J.R. Hughes, and C.A. Taylor. 2006. A coupled momentum method for modeling blow flow in three-dimensional deformable arteries. In *Computer Methods in Applied Mechanics and Engineering*:195(41-43): 5685-5706.

Finet, G., M. Gilard, B. Perrenot, G. Rioufol, P. Motreff, L. Gavit, and R. Prost. 2008. Fractal geometry of arterial coronary bifurcations: A quantitative coronary angiography and intravascular ultrasound analysis. *EuroIntervention* 3, no. 4: 490-8.

Finn, AV, G Nakazawa, M Joner, FD Kolodgie, EK Mont, HK Gold, and R Virmani. 2007. Vascular responses to drug eluting stents: Importance of delayed healing. *Arterioscler Thromb Vasc Biol* 27, no. 7: 1500-10.

Frank, AO, PW Walsh, and JE Jr Moore. 2002. Computational fluid dynamics and stent design. *Artif Organs* 26, no. 7: 614-21.

Fung, Y. C. 1997. *Biomechanics : Circulation*. New York: Springer.

Fung, YC and SQ Liu. 1993. Elementary mechanics of the endothelium of blood vessels. *J Biomech Eng* 115, no. 1: 1-12.

Gastaldi, D, S Morlacchi, R Nichetti, C Capelli, G Dubini, L Petrini, and F Migliavacca. 2010. Modelling of the provisional side-branch stenting approach for the treatment of atherosclerotic coronary bifurcations: Effects of stent positioning. *Biomech Model Mechanobiol*.

Ge, L, F Airoldi, I Iakovou, J Cosgrave, I Michev, GM Sangiorgi, M Montorfano, A Chieffo, M Carlino, N Corvaja, and A Colombo. 2005. Clinical and angiographic outcome after implantation of drug-eluting stents in bifurcation lesions with the crush stent technique: Importance of final kissing balloon post-dilation. *J Am Coll Cardiol* 46, no. 4: 613-20.

Girasis, C, PW Serruys, Y Onuma, A Colombo, DR Jr Holmes, TE Feldman, EJ Bass, K Leadley, KD Dawkins, and MC Morice. 2010. 3-dimensional bifurcation angle analysis in patients with left main disease: A substudy of the syntax trial (synergy between percutaneous coronary intervention with taxus and cardiac surgery). *JACC Cardiovasc Interv* 3, no. 1: 41-8.

Gray, Henry. 2003. *The complete gray's anatomy with later additions by dr. R.A. Bolam*. East Molesey: Merchant Book Company.

Guyton, Arthur C. and John E. Hall. 2006. *Textbook of medical physiology*. Ed Elsevier Saunders.

He, X and DN Ku. 1996. Pulsatile flow in the human left coronary artery bifurcation: Average conditions. *J Biomech Eng* 118, no. 1: 74-82.

Heldman, AW, L Cheng, GM Jenkins, PF Heller, DW Kim, M Jr Ware, C Nater, RH Hruban, B Rezai, BS Abella, KE Bunge, JL Kinsella, SJ Sollott, EG Lakatta, JA Brinker, WL Hunter, and JP Froehlich. 2001. Paclitaxel stent coating inhibits neointimal hyperplasia at 4 weeks in a porcine model of coronary restenosis. *Circulation* 103, no. 18: 2289-95.

Hoffmann, R., G. S. Mintz, G. R. Dussaillant, J. J. Popma, A. D. Pichard, L. F. Satler, K. M. Kent, J. Griffin, and M. B. Leon. 1996. Patterns and mechanisms of in-stent restenosis. A serial intravascular ultrasound study. *Circulation* 94, no. 6: 1247-54.

Ikeno, F, YH Kim, J Luna, JA Condado, A Colombo, E Grube, PJ Fitzgerald, SJ Park, and AC Yeung. 2006. Acute and long-term outcomes of the novel side access (slk-view) stent for bifurcation coronary lesions: A multicenter nonrandomized feasibility study. *Catheter Cardiovasc Interv* 67, no. 2: 198-206.

Kaimovitz, B, Y Huo, Y Lanir, and GS Kassab. 2008. Diameter asymmetry of porcine coronary arterial trees: Structural and functional implications. *Am J Physiol Heart Circ Physiol* 294, no. 2: H714-23.

Kastrati, A, J Mehilli, J Dirschinger, J Pache, K Ulm, H Schühlen, M Seyfarth, C Schmitt, R Blasini, FJ Neumann, and A Schömig. 2001. Restenosis after coronary placement of various stent types. *Am J Cardiol* 87, no. 1: 34-9.

Katritsis, D, L Kaiktsis, A Chaniotis, J Pantos, EP Efstathopoulos, and V Marmarelis. 2007. Wall shear stress: Theoretical considerations and methods of measurement. *Prog Cardiovasc Dis* 49, no. 5: 307-29.

Kawasaki, T., H. Koga, T. Serikawa, Y. Orita, S. Ikeda, T. Mito, Y. Gotou, Y. Shintani, A. Tanaka, H. Tanaka, T. Fukuyama, and N. Koga. 2009. The bifurcation study using 64 multislice computed tomography. *Catheter Cardiovasc Interv* 73, no. 5: 653-8.

Kitchens, C, W Jr Jordan, D Wirthlin, and D Whitley. 2002. Vascular complications arising from maldeployed stents. *Vasc Endovascular Surg* 36, no. 2: 145-54.

Kleinstreuer, C, S Hyun, JR Jr Buchanan, PW Longest, JP Jr Archie, and GA Truskey. 2001. Hemodynamic parameters and early intimal thickening in branching blood vessels. *Crit Rev Biomed Eng* 29, no. 1: 1-64.

Koo, BK, KW Park, HJ Kang, YS Cho, WY Chung, TJ Youn, IH Chae, DJ Choi, SJ Tahk, BH Oh, YB Park, and HS Kim. 2008. Physiological evaluation of the provisional side-branch intervention strategy for bifurcation lesions using fractional flow reserve. *Eur Heart J* 29, no. 6: 726-32.

Laborde, JC, N Borenstein, L Behr, and S Ramcharitar. 2007. Stentys coronary bifurcation stent. *EuroIntervention* 3, no. 1: 162-5.

LaDisa, JF Jr, DA Hettrick, LE Olson, I Guler, ER Gross, TT Kress, JR Kersten, DC Warltier, and PS Pagel. 2002. Stent implantation alters coronary artery hemodynamics and wall shear stress during maximal vasodilation. *J Appl Physiol* 93, no. 6: 1939-46.

LaDisa, JF Jr, LE Olson, I Guler, DA Hettrick, SH Audi, JR Kersten, DC Warltier, and PS Pagel. 2004. Stent design properties and deployment ratio influence indexes of wall shear stress: A three-dimensional computational fluid dynamics investigation within a normal artery. *J Appl Physiol* 97, no. 1: 424-30; discussion 416.

LaDisa, JF Jr, LE Olson, I Guler, DA Hettrick, JR Kersten, DC Warltier, and PS Pagel. 2005. Circumferential vascular deformation after stent implantation alters wall shear stress evaluated with time-dependent 3d computational fluid dynamics models. *J Appl Physiol* 98, no. 3: 947-57.

Latib, A, A Colombo, and GM Sangiorgi. 2009. Bifurcation stenting: Current strategies and new devices. *Heart* 95, no. 6: 495-504.

Lefèvre, T, Y Louvard, MC Morice, P Dumas, C Loubeyre, A Benslimane, RK Premchand, N Guillard, and JF Piéchaud. 2000. Stenting of bifurcation lesions: Classification, treatments, and results. *Catheter Cardiovasc Interv* 49, no. 3: 274-83.

Lefèvre, T, MC Morice, G Sengottuvel, A Kokis, M Monchi, P Dumas, P Garot, and Y Louvard. 2005. Influence of technical strategies on the outcome of coronary bifurcation stenting. *EuroIntervention* 1, no. 1: 31-7.

Les, AS, SC Shadden, CA Figueroa, JM Park, MM Tedesco, RJ Herfkens, RL Dalman, and CA Taylor. 2010. Quantification of hemodynamics in abdominal aortic aneurysms during rest and exercise using magnetic resonance imaging and computational fluid dynamics. *Ann Biomed Eng* 38, no. 4: 1288-313.

Long, Q., B. Ariff, S. Z. Zhao, S. A. Thom, A. D. Hughes, and X. Y. Xu. 2003. Reproducibility study of 3d geometrical reconstruction of the human carotid bifurcation from magnetic resonance images. *Magn Reson Med* 49, no. 4: 665-74.

Louvard, Y, T Lefèvre, and MC Morice. 2004. Percutaneous coronary intervention for bifurcation coronary disease. *Heart* 90, no. 6: 713-22.

Malek, AM, SL Alper, and S Izumo. 1999. Hemodynamic shear stress and its role in atherosclerosis. *JAMA* 282, no. 21: 2035-42.

Matsunaga, E, N Takaya, T Yokoyama, Y Akimoto, K Miyauchi, and H Daida. 2009. Relationship between coronary artery wall thickness measured by 64-slice multidetector computed tomography and cardiovascular risk factors. *Circ J* 73, no. 4: 681-5.

McFadden, EP, E Stabile, E Regar, E Cheneau, AT Ong, T Kinnaird, WO Suddath, NJ Weissman, R Torguson, KM Kent, AD Pichard, LF Satler, R Waksman, and PW Serruys. 2004. Late thrombosis in drug-eluting coronary stents after discontinuation of antiplatelet therapy. *Lancet* 364, no. 9444: 1519-21.

Miller, JM, CE Rochitte, M Dewey, A Arbab-Zadeh, H Niinuma, I Gottlieb, N Paul, ME Clouse, EP Shapiro, J Hoe, AC Lardo, DE Bush, A de Roos, C Cox, J Brinker, and JA Lima. 2008. Diagnostic performance of coronary angiography by 64-row ct. *N Engl J Med* 359, no. 22: 2324-36.

Mortier, P., M. De Beule, D. Van Loo, B. Verhegghe, and P. Verdonck. 2009. Finite element analysis of side branch access during bifurcation stenting. *Med Eng Phys* 31, no. 4: 434-40.

Murray, CD. 1926. The physiological principle of minimum work applied to the angle of branching of arteries. *J Gen Physiol* 9, no. 6: 835-841.

Müller, J, O Sahni, X Li, KE Jansen, MS Shephard, and CA Taylor. 2005. Anisotropic adaptive finite element method for modelling blood flow. *Comput Methods Biomech Biomed Engin* 8, no. 5: 295-305.

N, Westerhof, Stergiopulos N, and Noble MIM. 2005. *Snapshots of hemodynamics an aid for clinical research and graduate education*. Ed Springer. New York.

NIH, National Institute of Health. Http://www.Nih.Gov/index.Html. http://www.nih.gov/.

Pan, M, J Suárez de Lezo, A Medina, M Romero, A Delgado, J Segura, S Ojeda, F Mazuelos, E Hernandez, F Melian, D Pavlovic, F Esteban, and J Herrador. 2007. Drug-eluting stents for the treatment of bifurcation lesions: A randomized comparison between paclitaxel and sirolimus stents. *Am Heart J* 153, no. 1: 15.e1-7.

Pflederer, T., J. Ludwig, D. Ropers, W. G. Daniel, and S. Achenbach. 2006. Measurement of coronary artery bifurcation angles by multidetector computed tomography. *Invest Radiol* 41, no. 11: 793-8.

Pijls, NH, B De Bruyne, K Peels, PH Van Der Voort, HJ Bonnier, JJ Bartunek J Koolen, and JJ Koolen. 1996. Measurement of fractional flow reserve to assess the functional severity of coronary-artery stenoses. *N Engl J Med* 334, no. 26: 1703-8.

Pijls, NH, JA van Son, RL Kirkeeide, B De Bruyne, and KL Gould. 1993. Experimental basis of determining maximum coronary, myocardial, and collateral blood flow by pressure measurements for assessing functional stenosis severity before and after percutaneous transluminal coronary angioplasty. *Circulation* 87, no. 4: 1354-67.

Reig, J and M Petit. 2004. Main trunk of the left coronary artery: Anatomic study of the parameters of clinical interest. *Clin Anat* 17, no. 1: 6-13.

Sharma, SK, AM Mareş, and AS Kini. 2009. Coronary bifurcation lesions. *Minerva Cardioangiol* 57, no. 5: 667-82.

Subbotin, VM. 2007. Analysis of arterial intimal hyperplasia: Review and hypothesis. *Theor Biol Med Model* 4: 41.

Tang, BT, CP Cheng, MT Draney, NM Wilson, PS Tsao, RJ Herfkens, and CA Taylor. 2006. Abdominal aortic hemodynamics in young healthy adults at rest and during lower limb exercise: Quantification using image-based computer modeling. *Am J Physiol Heart Circ Physiol* 291, no. 2: H668-76.

Taylor, CA, TJ Hughes, and CK Zarins. 1998. Finite element modeling of three-dimensional pulsatile flow in the abdominal aorta: Relevance to atherosclerosis. *Ann Biomed Eng* 26, no. 6: 975-87.

Thomas, J. B., L. Antiga, S. L. Che, J. S. Milner, D. A. Steinman, J. D. Spence, and B. K. Rutt. 2005. Variation in the carotid bifurcation geometry of young versus older adults: Implications for geometric risk of atherosclerosis. *Stroke* 36, no. 11: 2450-6.

van der Waal, E. C., G. S. Mintz, H. M. Garcia-Garcia, A. B. Bui, M. Pehlivanova, C. Girasis, P. W. Serruys, W. J. van der Giessen, and N. J. Weissman. 2009. Intravascular ultrasound and 3d angle measurements of coronary bifurcations. *Catheter Cardiovasc Interv* 73, no. 7: 910-6.

Van Huis, GA, P Sipkema, and N Westerhof. 1987. Coronary input impedance during cardiac cycle as determined by impulse response method. *Am J Physiol* 253, no. 2 Pt 2: H317-24.

Vassilev, D and RJ Gil. 2008. Relative dependence of diameters of branches in coronary bifurcations after stent implantation in main vessel--importance of carina position. *Kardiol Pol* 66, no. 4: 371-8; discussion 379.

Verheye, S, E Grube, S Ramcharitar, JJ Schofer, B Witzenbichler, J Kovac, KE Hauptmann, P Agostoni, M Wiemer, T Lefèvre, PW Serruys, and RJ van Geuns. 2009. First-in-man (fim) study of the stentys bifurcation stent--30 days results. *EuroIntervention* 4, no. 5: 566-71.

Vignon-Clementel IE, Figueroa CA, Jansen KE, and Taylor CA. 2006. *Outflow boundary conditions for three-dimensional finite element modeling of blood flow and pressure in arteries*. In *Computational Methods in Applied Mechanics and Engineering*:3776-3796.

Wang, WQ, DK Liang, DZ Yang, and M Qi. 2006. Analysis of the transient expansion behavior and design optimization of coronary stents by finite element method. *J Biomech* 39, no. 1: 21-32.

Williams, A.R. 2008. Quantifying hemodynamic changes caused by stenting of coronary bifurcation lesions using realistic computational fluid dynamics models. Master of Science, Marquette University.

Williams, AR, BK Koo, TJ Gundert, PJ Fitzgerald, and J Jr Ladisa. 2010. Local hemodynamic changes caused by main branch stent implantation and virtual side branch balloon angioplasty in a representative coronary bifurcation. *J Appl Physiol*.

Yamagishi, M, H Hosokawa, S Saito, S Kanemitsu, M Chino, S Koyanagi, K Urasawa, K Ito, S Yo, J Honye, M Nakamura, T Matsumoto, A Kitabatake, N Takekoshi, and T Yamaguchi. 2002. Coronary disease morphology and distribution determined by quantitative angiography and intravascular ultrasound--re-evaluation in a cooperative multicenter intravascular ultrasound study (comius). *Circ J* 66, no. 8: 735-40.

Yushkevich, PA, J Piven, HC Hazlett, RG Smith, S Ho, JC Gee, and G Gerig. 2006. User-guided 3d active contour segmentation of anatomical structures: Significantly improved efficiency and reliability. *Neuroimage* 31, no. 3: 1116-28.

Zubaid, M, C Buller, and GB Mancini. 2002. Normal angiographic tapering of the coronary arteries. *Can J Cardiol* 18, no. 9: 973-80.

APPENDIX A

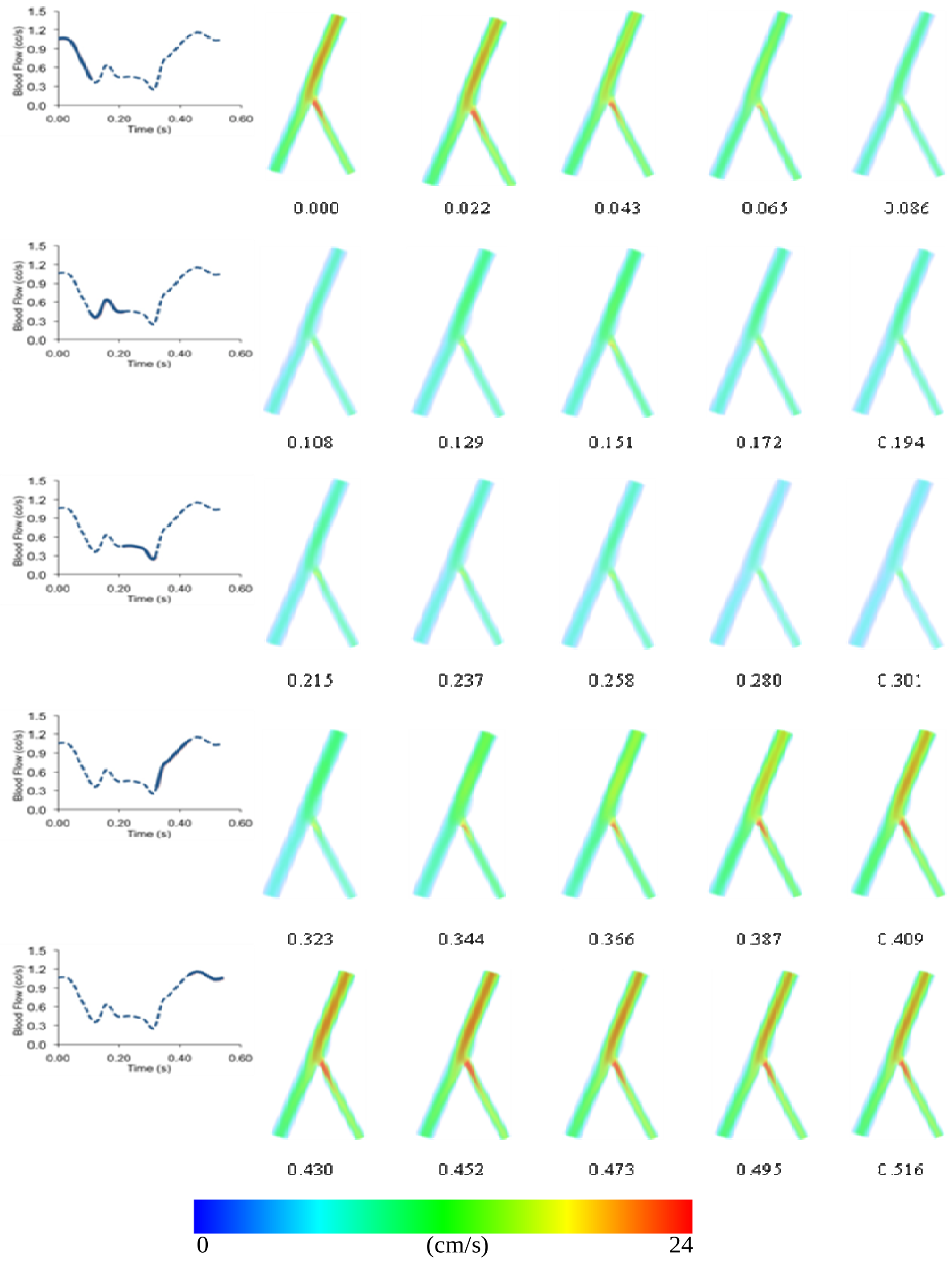

Volume rendered velocity of the idealized CFD MV stented model with aggressive KB under resting blood flow conditions, numbers are time in seconds.

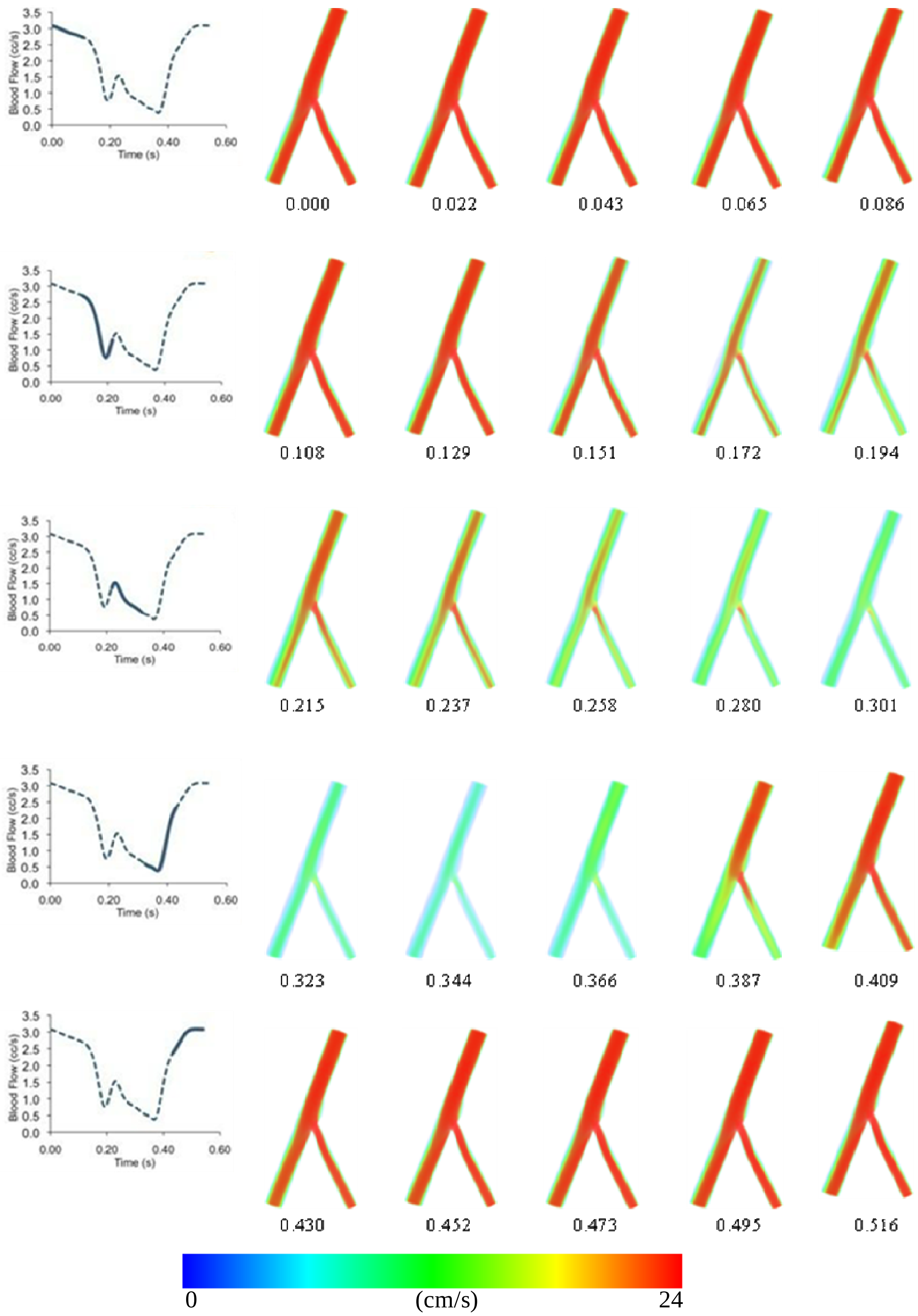

Volume rendered velocity of the idealized MV stented model with aggressive KB under hyperemia blood flow conditions, numbers are time in seconds

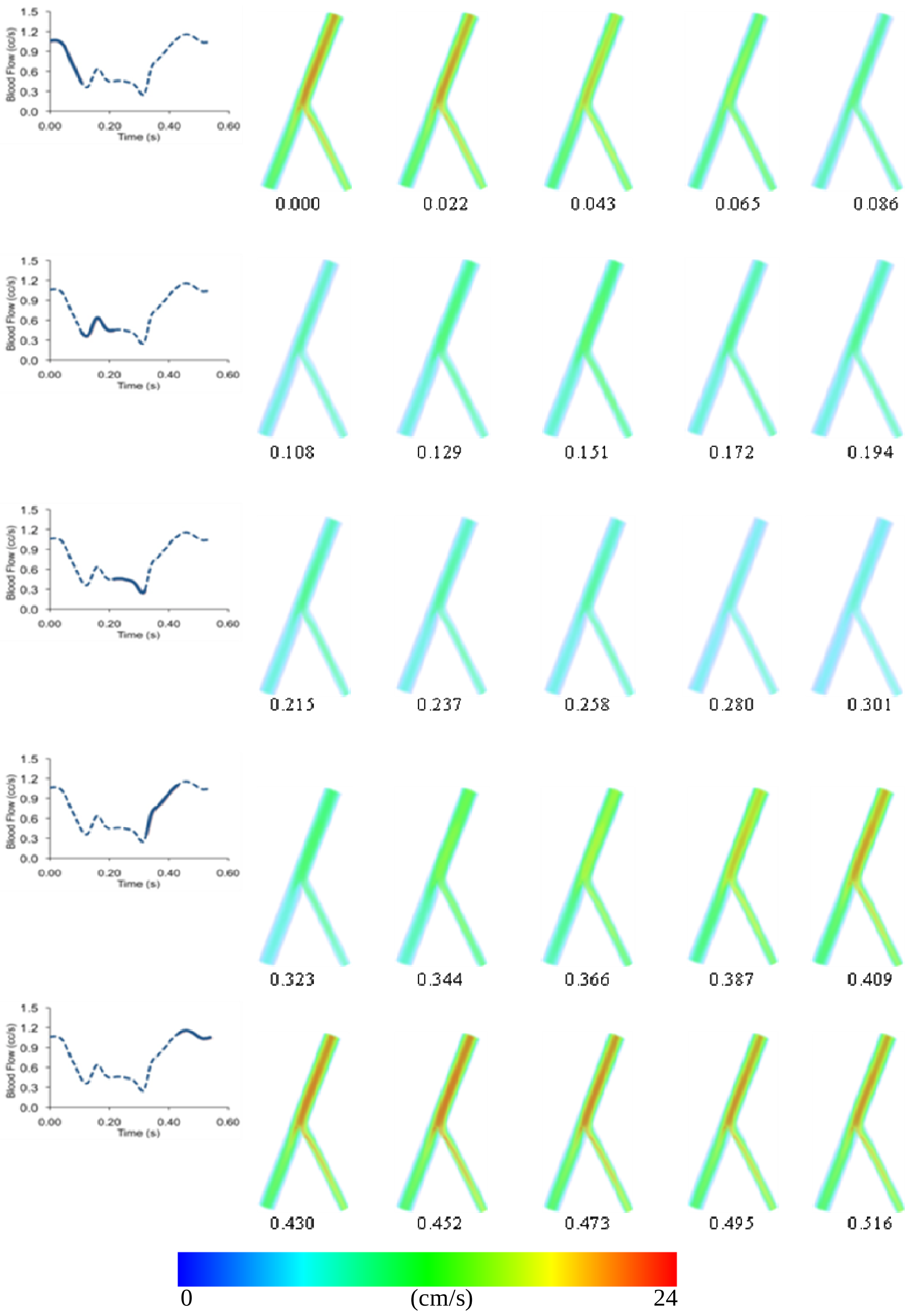

Volume rendered velocity of the idealized MV and SB stenting without KB under resting blood flow conditions, numbers are time in seconds.

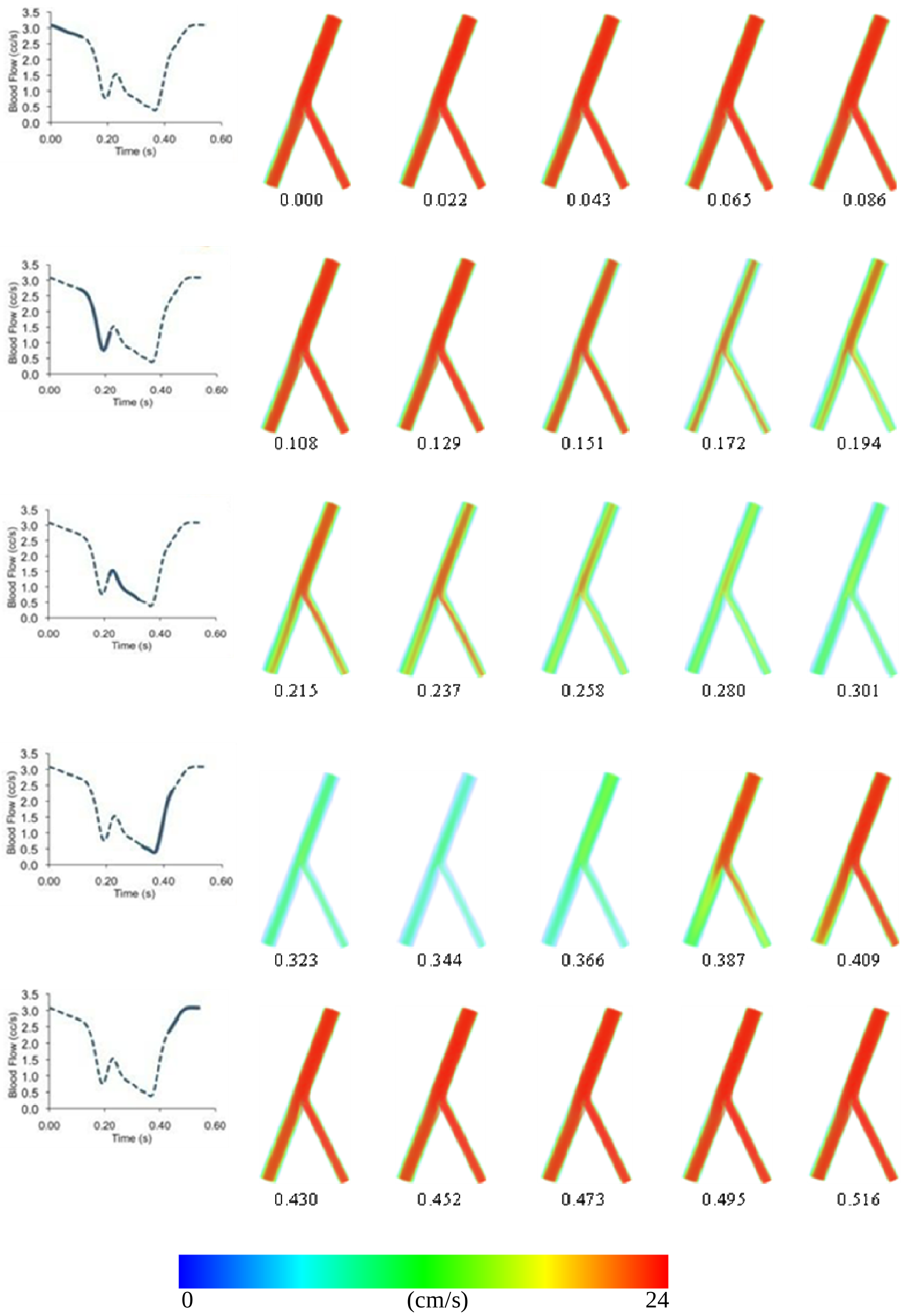

Volume rendered velocity of the idealized MV and SB stenting without KB under hyperemia blood flow conditions, numbers are time in seconds.

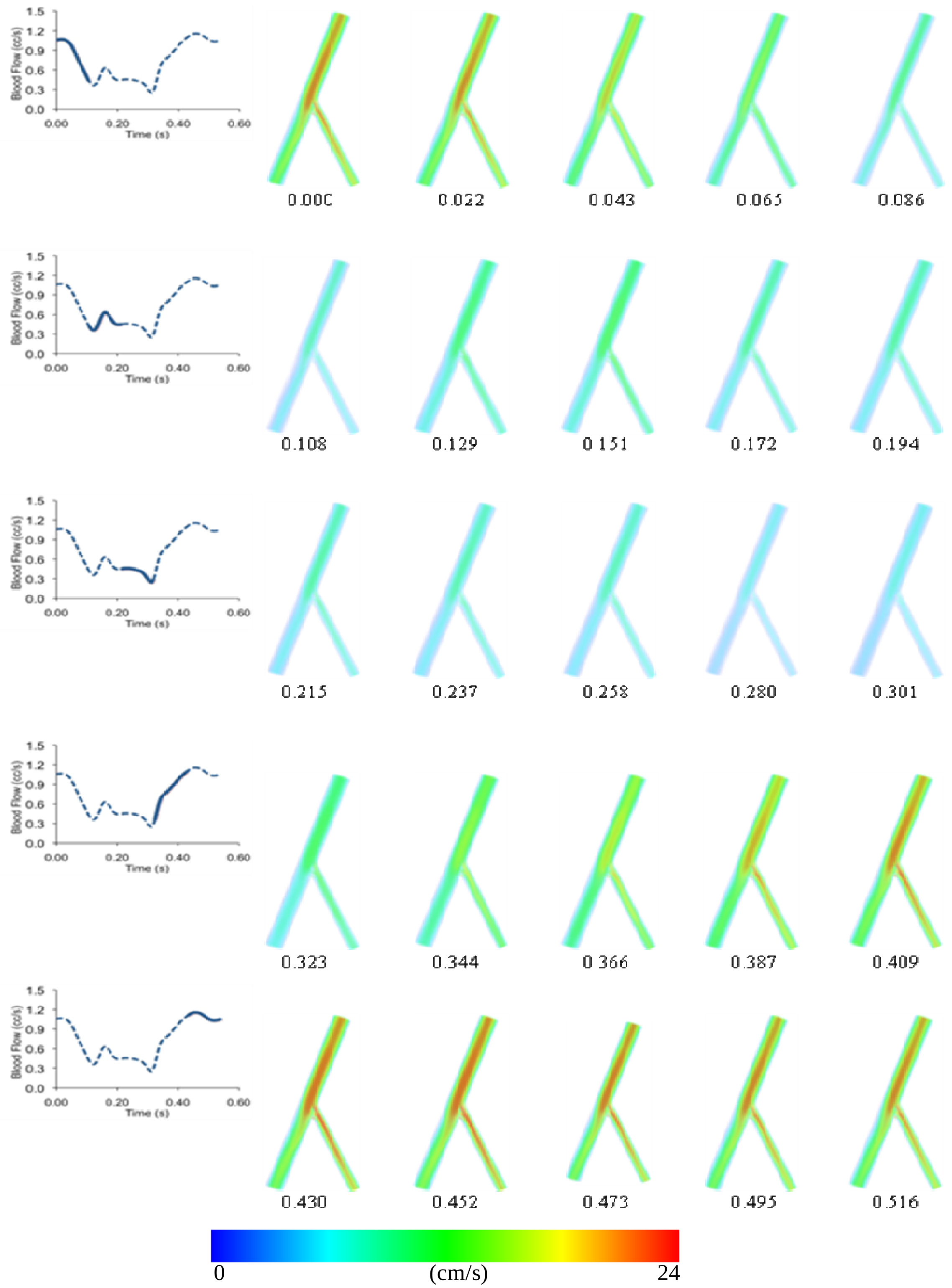

Volume rendered velocity of the idealized MV and SB stenting with gentle KB under resting blood flow conditions, numbers are time in seconds.

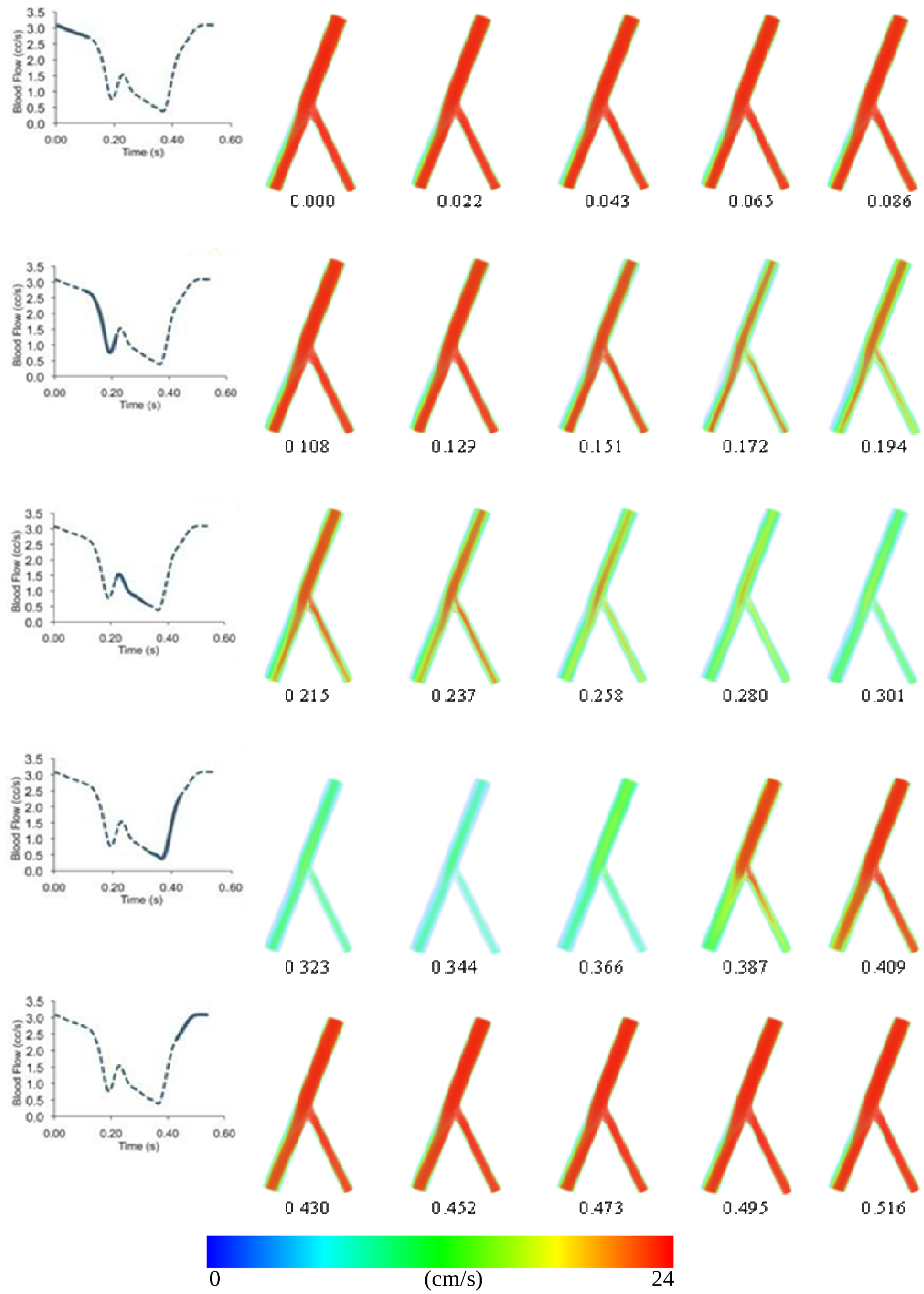

Volume rendered velocity of the idealized MV and SB stenting with gentle KB under hyperemia blood flow conditions, numbers are time in seconds.

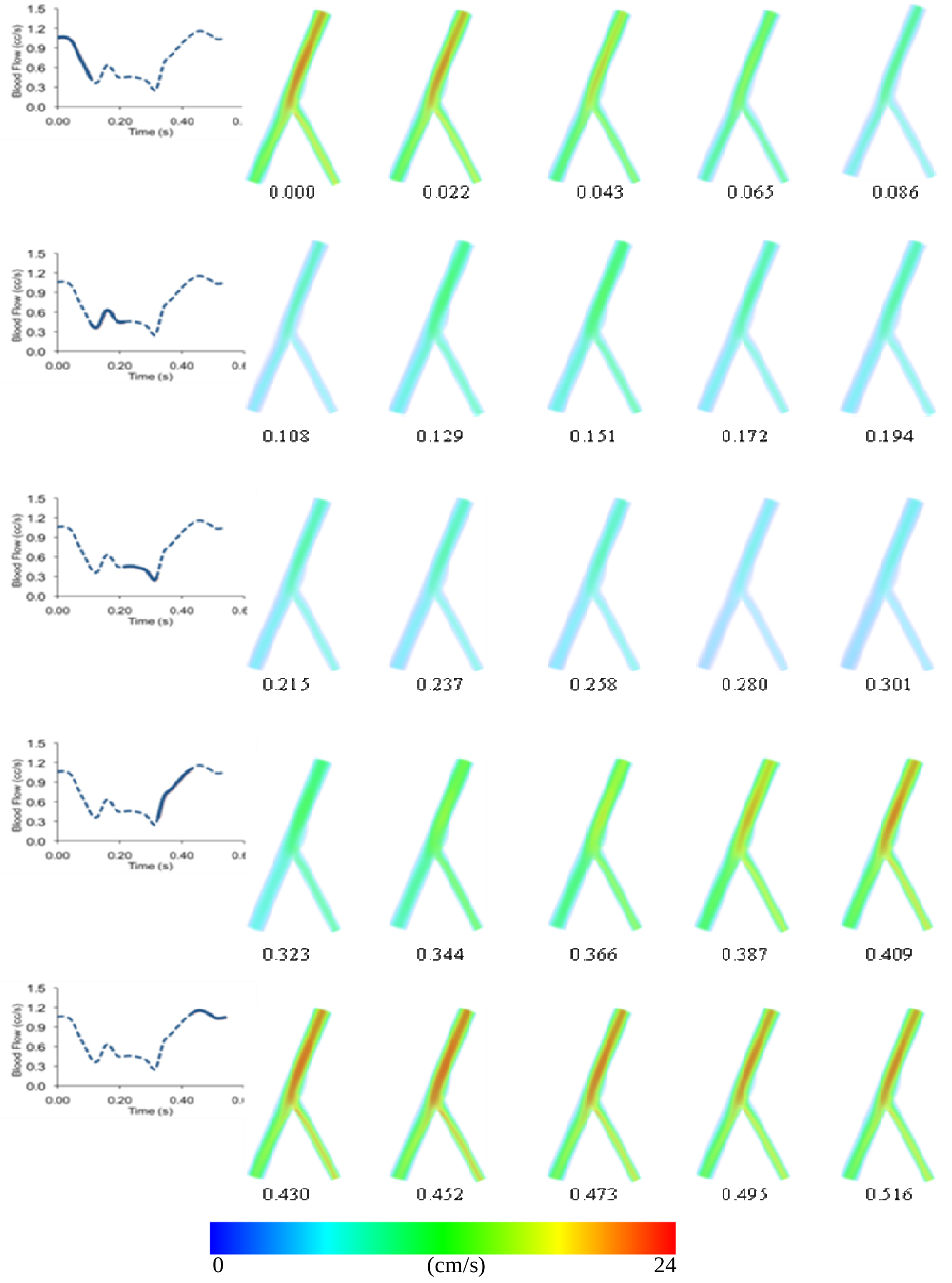

Volume rendered velocity of the idealized MV and SB stenting with aggressive KB under resting blood flow conditions, numbers are time in seconds.

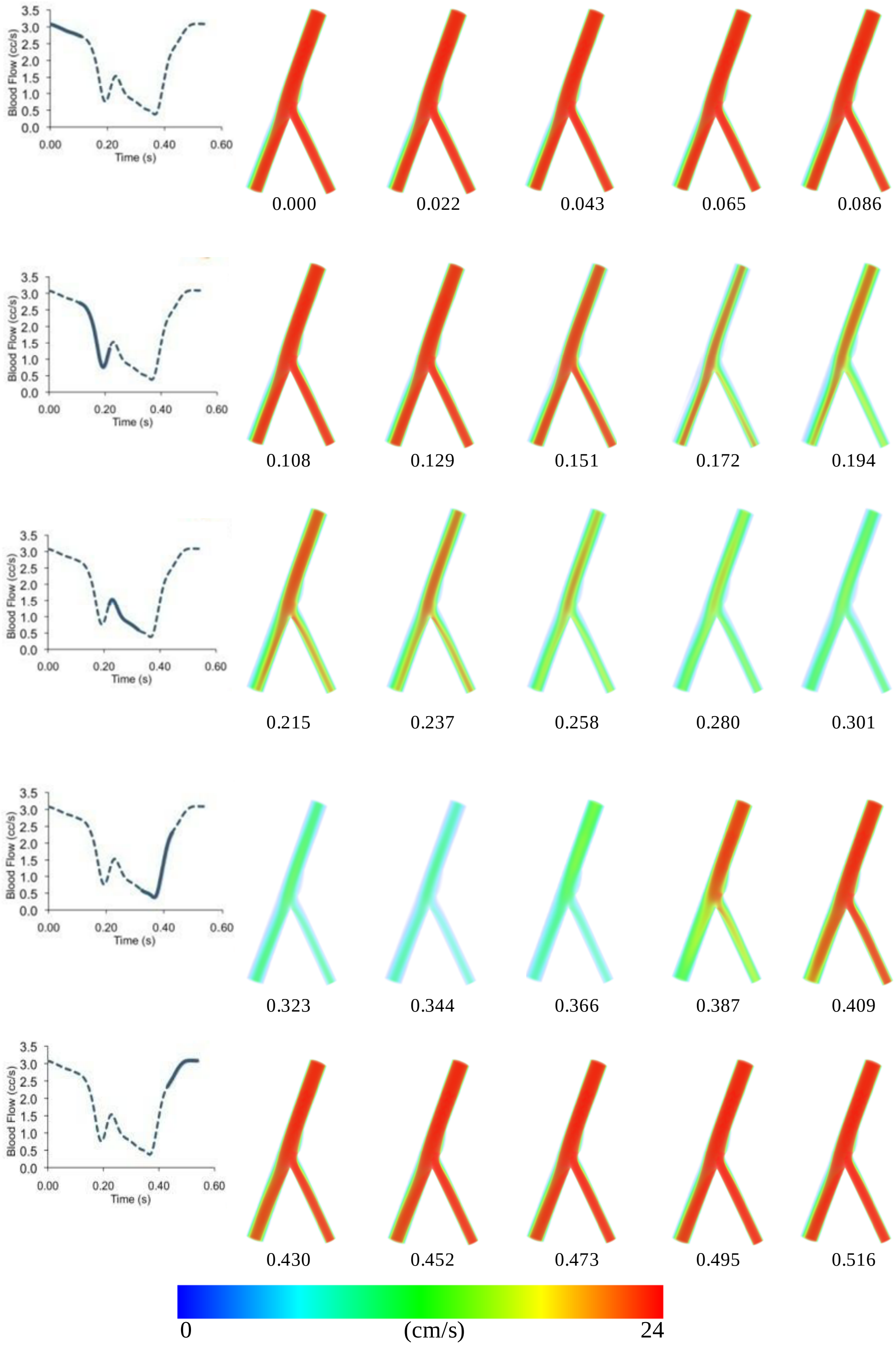

Volume rendered velocity of the idealized MV and SB stenting with gentle KB under hyperemiablood flow conditions, numbers are time in seconds.

APPENDIX B

Within the document WSS distributions for both the MV and SB are reported for resting conditions. Hyperemia conditions can also be examined in the same manner. The figures below show distributions of WSS in axial and circumferential locations. The same trends observed during resting blood flow conditions are amplified during hyperemia conditions.

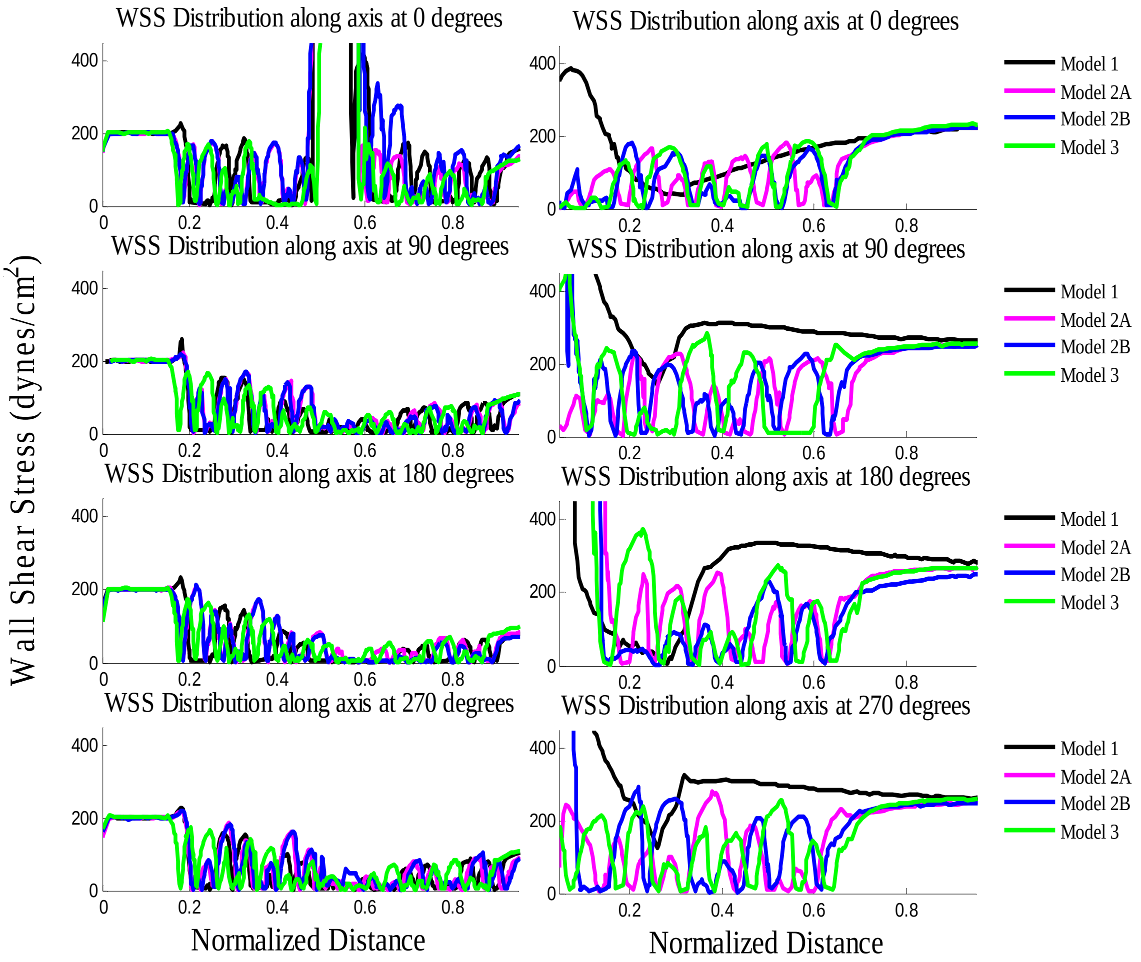

Axial WSS distributions the MV (left panel) and SB (right) panel for all four idealized models under hyperemia conditions.

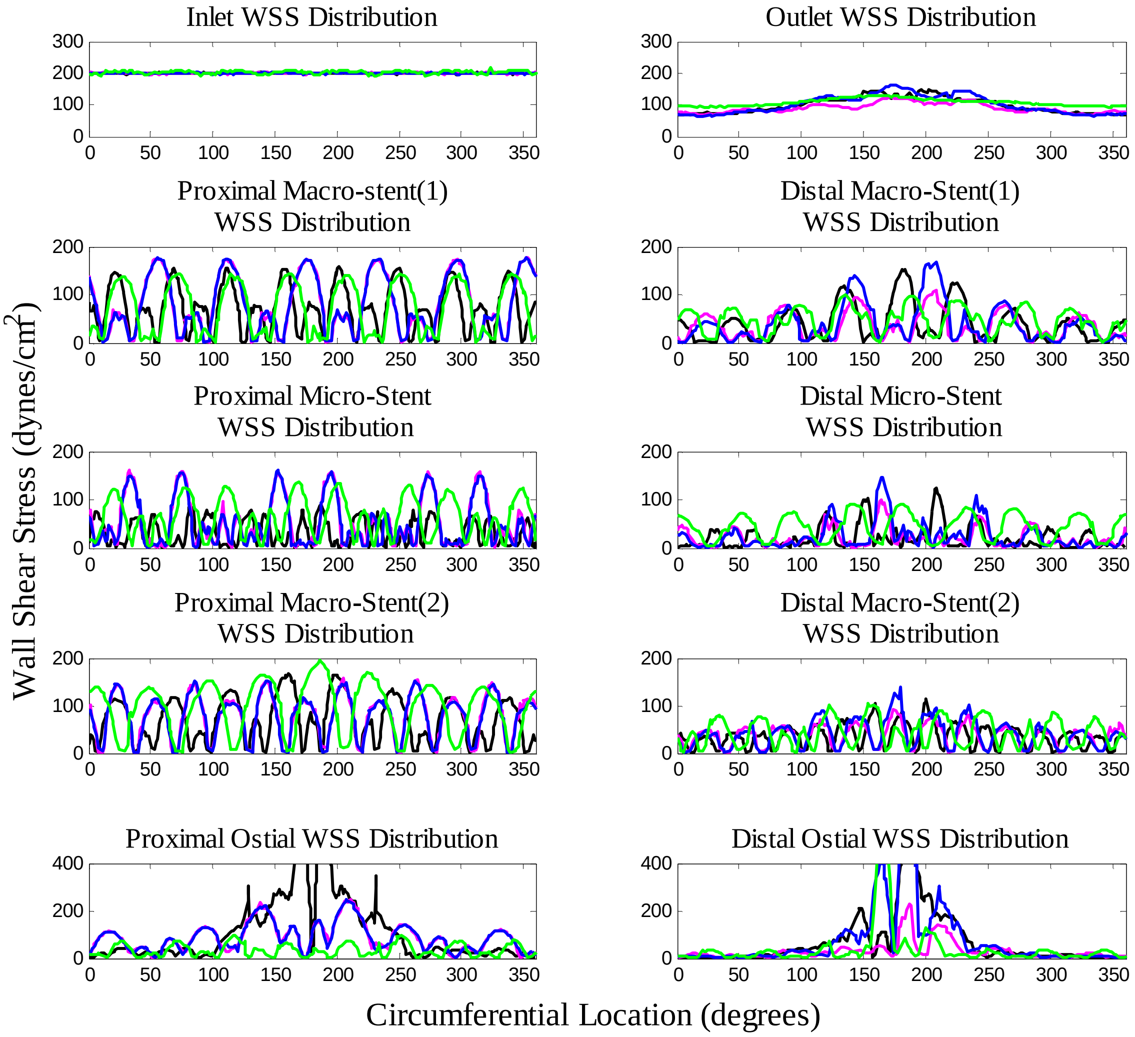

Circumferential WSS distributions at specific locations within the MV for all four idealized models under hyperemia conditions.

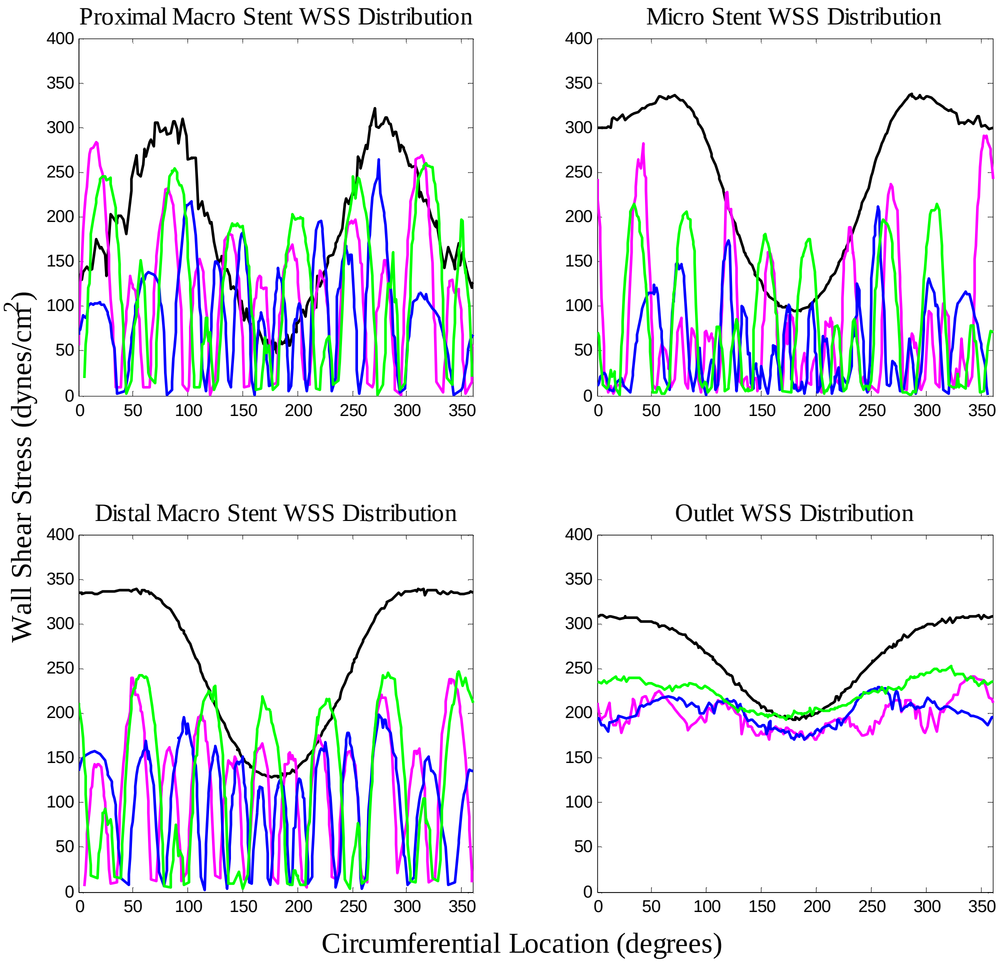

Circumferential graphs of WSS at selected locations along the side branch.

APPENDIX C

Hierarchical Clustering Values for Vessel Segments

PV Cluster	Area (mm2)	Length (mm)	EI	Taper Factor	ROC (mm^{-1})
26	9.5 ± 3.3	16.3 ± 6	0.2 ± 0.1	0.1 ± 0.06	0.2 ± 0.08
31	14.7 ± 6.9	10.7 ± 3.8	0.2 ± 0.1	0.1 ± 0.05	0.2 ± 0.07
6	26.8 ± 5.4	5.5 ± 2.7	0.2 ± 0.0	0.1 ± 0.05	0.2 ± 0.04
DV Cluster	**Area (mm2)**	**Length (mm)**	**EI**	**Taper Factor**	**ROC (mm^{-1})**
28	9.6 ± 3.1	21.0 ± 5.7	0.2 ± 0.1	0.1 ± 0.03	0.2 ± 0.04
23	5.3 ± 1.7	24.1 ± 6	0.2 ± 0	0.1± 0.03	0.3 ± 0.08
12	15.0 ± 7.2	16.0 ± 5.4	0.2 ± 0.1	0.04 ± 0.04	0.2 ± 0.11
SB Cluster	**Area (mm2)**	**Length (mm)**	**EI**	**Taper Factor**	**ROC (mm^{-1})**
6	8.2 ± 3.1	10.8 ± 4.7	0.2 ± 0.1	0.04 ± 0.03	0.2 ± 0.1
5	16.4 ± 5.3	11.7 ± 5	0.3 ± 0	0.1 ± 0.07	0.2 ± 0.07
54	4.9 ± 3.2	19.9 ± 7.3	0.2 ± 0.1	0.1 ± 0.05	0.3 ± 0.17
Ostium Cluster	**Area (mm2)**	**Length (mm)**	**EI**	**Taper Factor**	
11	12.1 ± 4.5	7.1 ± 2.5	0.5± 0.1	0.1 ± 0.07	
50	16.3 ± 8.2	4.2 ± 1.7	0.4 ± 0.1	0.1 ± 0.06	
4	12.6 ± 5.4	12.0 ± 5.7	0.3 ± 0.1	0.04 ± 0.01	

Values from hierarchical clustering for individual vessel segments.

Hierarchical Clustering Values (Bifurcation Sites)

LCA Cluster	**Area (mm2)**	**Length (mm)**	**EI**	**DIA (degrees)**	**PIA (degrees)**	**Taper Factor**	**ROC (mm^{-1})**
7	40.2 ± 4.3	6.7 ± 3.9	0.2 ± 0.1	58 ± 6	152 ± 0	0.09 ± 0.06	0.14 ± 0.04
40	16.0 ± 6.8	15.1 ± 9.9	0.2 ± 0.1	67 ± 12	164 ± 25	0.09 ± 0.07	0.18 ± 0.04
33	10.1 ± 3.9	12.0 ± 7.4	0.2 ± 0.1	80 ± 7	137 ± 14	0.08 ± 0.06	0.21 ± 0.04
7	18.0 ± 7.7	20.9 ± 14.2	0.2 ± 0	112 ± 0	123 ± 0	0.12 ± 0.04	0.13 ± 0.01
LAD Cluster	**Area (mm2)**	**Length (mm)**	**EI**	**DIA (degrees)**	**PIA (degrees)**	**Taper Factor**	**ROC (mm^{-1})**
8	10.1 ± 5.1	14.9 ± 5.2	0.2 ± 0.1	98 ± 10	132 ± 1	0.07 ± 0.06	0.21 ± 0.08
24	10.2 ± 5.9	14.3 ± 6.1	0.2 ± 0.1	73 ± 6	135 ± 14	0.07 ± 0.04	0.25 ± 0.11
7	32.0 ± 3.9	14.7 ± 5.7	0.2 ± 0	35 ± 0	148 ± 0	0.06 ± 0.03	0.11 ± 0
49	7.8 ± 4.4	13.8 ± 7.5	0.2 ± 0.1	54 ± 6	159 ± 14	0.06 ± 0.04	0.30 ± 0.12
LCX Cluster	**Area (mm2)**	**Length (mm)**	**EI**	**DIA (degrees)**	**PIA (degrees)**	**Taper Factor**	**ROC (mm^{-1})**
7	11.5 ± 5.1	3.8 ± 1.7	0.3 ± 0.2	80 ± 6	139 ± 9	0.09 ± 0.04	0.29 ± 0.15
21	6.1 ± 3.3	24.0 ± 6.4	0.2 ± 0.1	76 ± 7	141 ± 10	0.05 ± 0.05	0.28 ± 0.14
7	5.8 ± 3	12.4 ± 6.8	0.2 ± 0.1	36 ± 0	168 ± 0	0.04 ± 0.02	0.33 ± 0.03
53	9.8 ± 6.1	12.9 ± 8.8	0.3 ± 0.1	59 ± 8	155 ± 8	0.05 ± 0.04	0.27 ±0.13

Values from hierarchical clustering values from each bifurcation site.